Carbon Nanotubes In DC and Microwave Superconducting Circuits



Ani Nersisyan

Supervisor: Peter J. Leek

University College

University of Oxford

A thesis submitted for the degree of

Doctor of Philosophy

Hilary 2016

Declaration

I hereby declare that except where specific reference is made to the work of others, the contents of this dissertation are original and have not been submitted in whole or in part for consideration for any other degree or qualification to this, or any other university. This dissertation is my own work and contains nothing which is the outcome of work done in collaboration with others, except as specified in the text and Acknowledgments.

Ani Nersisyan
January 2017

This thesis is dedicated to
my family and the little one

Acknowledgements

I am incredibly thankful to everyone who has helped to make my time in Oxford so rewarding.

Thank you Peter, for giving me the opportunity to work in your lab at Oxford. It was an honour for me to be one of the first PhD students in your group and take part in the building of a very advanced laboratory in an empty room. I owe a great deal of my success to your thoughtful and patient guidance and support. You have created an ideal environment for a graduate student that is both challenging and nurturing.

I express my gratitude to everyone in the Leeklab for all of the support and inspiration. The daily conversations at the lab made the hard process of fabrication and measurements very enjoyable. Thank you, Ric, for all the coffee hours. Thank you, Michael, for enriching us with the infinite amount of information about the economics and politics. Thank you, Einar, for being so relaxed about the challenges that came across and thus serving as a good example. I would also like to thank Andy, Joseph, Giovanna and Matthias for the useful discussions.

Thanks to Andreas Landig, who did his Master thesis project at the Leeklab, for helping me with the measurements of the resonators.

I would like to express my gratitude to Fei Pei for growing carbon nanotube samples for us, as well as for useful discussions regarding the fabrication techniques.

I am thankful to Francesca, Alex, Piet and Shilei for creating a very motivating and enjoyable environment at the office.

Thanks to all my friends at Oxford whose constant companionship and easy going attitudes have made it a great pleasure to live here.

Last but not least, I am grateful to my parents who are always supportive and eager to listen to my attempts to explain my thesis. Thank you for accepting my decision to move so far from home. Thanks to my dear sisters and my brother for always being there for me over the years. Finally, I am immeasurably thankful to my husband, Vahe, for being so patient and understanding and for supporting me through the highs and lows of my DPhil. I wouldn't be the person I am if it weren't for you.

Abstract

This thesis presents an effort towards integration of superconductor-contacted carbon nanotubes into microwave circuits, as a new tool for building quantum circuits. Carbon nanotubes show a wealth of quantum phenomena demonstrated in transport experiments by different groups in the last two decades. With the development of circuit QED, one can study these phenomena using on-chip microwave circuits. Moreover, in superconductor-contacted nanotubes, Andreev reflection of the particles at the interfaces leads to the formation of Andreev bound states. A pair of such states can potentially serve as a new type of a qubit.

Here, fabrication and measurement techniques of superconductor contacted carbon nanotubes and superconductor/normal metal bilayer microwave circuits is developed, and their behaviour is studied.

In superconductor-contacted nanotubes the full range of contact transparencies is investigated, showing different transport phenomena such as Coulomb blockade, Kondo effect and Fabry-Pérot interference. In addition, the interplay of these effects with multiple Andreev reflection phenomena and the superconducting proximity-induced non-dissipative current transport through the nanotube is studied.

The proximity effect is studied using microwave resonators made of superconductor/normal metal bilayers. Characteristic parameters of the bilayers, such as the critical temperature and the magnetic penetration depth are reliably extracted from the measurements.

Finally, the two experiments are brought together in the first step towards using superconductor-contacted nanotubes in quantum microwave circuits. The successful realization of such circuit is achieved, where the Coulomb blockade in a nanotube quantum dot is probed with a microwave field.

Contents

I Introduction **1**

1 Hybrid Circuit QED 2
2 SC-contacted nanotubes 4
3 Thesis Overview 5

II Theoretical Concepts **7**

1 Quantum Transport in Carbon Nanotubes 8
1.1 Carbon Nanotubes 8
1.2 Coulomb Blockade in Carbon Nanotubes 17
1.3 Higher Order Tunneling: Kondo Effect 26
1.4 Ballistic Transport: Fabry-Pérot interference 30
2 Superconducting Proximity Effect in carbon nanotubes 31
2.1 Andreev Reflection 33
2.2 Subharmonic gap structure: Multiple Andreev Reflections . 36
2.3 Andreev Bound States 38
2.4 Experimental studies of superconductor-contacted carbon nanotubes 40
3 Superconducting Microwave Resonators for Circuit QED 41
3.1 Basic Theory of Parallel LCR Circuits 42
3.2 Transmission Model for Capacitively Coupled LC Resonator 43
3.3 Inductance of the Lumped Resonator 46
3.4 Temperature Dependence of the Quality Factor 47
3.5 Quantization of the LCR Resonator 48
4 CNT-SQUID Resonator Coupling 50
4.1 Carbon Nanotube RF SQUID 51
4.2 Inductive Coupling of CNT SQUID to MW Resonator . . . 53

III Experimental Techniques **55**

1 Carbon Nanotube Devices 56
1.1 Sample Fabrication 56
1.2 Measurement Setup Description 60
2 Microwave Resonators 64

2.1 Sample Preparation 64
2.2 Measurement Techniques 66
3 Nanotube-Resonator Coupled Devices 67
3.1 Design and Fabrication of Coupled Devices 68
3.2 Measurement Setup 70

IV DC Transport in Nanotube Devices 75
1 Normal Metal Contacted Nanotubes 76
1.1 High Interface Barrier: Coulomb Blockade 76
1.2 Medium Interface Barrier: Kondo Effect 79
1.3 Low Interface Barrier: Fabry-Perot Interference 80
2 SN-bilayer Contacted Nanotubes 82
2.1 Multiple Andreev Reflection in the Fabry-Pérot Regime . . . 82
2.2 MAR at Fabry-Perot to Coulomb Blockade Transition . . . 91
2.3 Interplay of Four-fold Degeneracy and Multiple Andreev Reflections in a Carbon Nanotube Quantum Dot 105
2.4 Discussion and Conclusion 111

V Microwave Resonators for Proximity Effect Studies 117
1 Characterization of superconducting microwave LC resonators . . . 118
1.1 Extracting Resonator Parameters From Temperature Dependence of Transmission 121
2 Measuring Proximity in Pd/Al Bilayers Using LC Resonators 125
2.1 Proximity Effect in SN Bilayers 125
2.2 Measuring LC resonator frequency response in a multiplexed geometry 126
2.3 Extracting LC resonator parameters from their temperature dependence 128
2.4 Study of the Critical Temperature of Pd/Al Bilayers 130
2.5 Discussion and Conclusion 133

VI Embedding carbon nanotubes in an SN-bilayer microwave LC circuit 137
1 Design of LC resonator nanotube coupled devices 138
2 Probing Coulomb Blockade with Microwave Field 141
2.1 Circuit Model of Nanotube SQUID-Resonator System 144
2.2 Power Dependence of the Amplitude Dips 148
3 Discussion and Conclusion 151

VII Conclusion and Prospects 155

Bibliography **159**

Appendices

A Derivation of the Transmission for Two-port Resonators **173**

B Labeling of Nanotube Devices **175**

I Introduction

Contents

1	**Hybrid Circuit QED**	**2**
2	**SC-contacted nanotubes**	**4**
3	**Thesis Overview**	**5**

The rapidly growing field of circuit quantum electrodynamics (cQED) [1, 2, 3] offers exciting prospects for learning about quantum systems and exercising control over them. Circuit QED is an implementation of cavity quantum electrodynamics in an electrical circuit, involving the coupling of an on-chip microwave resonator to a superconducting qubit. It allows to engineer flexible designs to study the nonlinearities and quantum interactions between the qubits and microwave fields. Unprecedented break-throughs in quantum information processing have been achieved by coupling artificial atoms, such as Josephson junction qubits to superconducting microwave resonators [4]. Inspired by this results, other solid state systems have been used in resonant circuits as potential qubits [5, 6] or quantum memories [7, 8, 9].

Recently, carbon nanotubes have demonstrated their potential as one-dimensional conductors, which show a wealth of quantum phenomena such as Coulomb blockade

[10], Fabry-Pérot interference [11], Luttinger-liquid behavior [12], Kondo effects [13], spin-orbit coupling [14], and a rich interplay between them [15]. Moreover, in nanotubes contacted by superconducting leads, new phenomena have been studied such as multiple Andreev reflections and Andreev bound states [16].

This thesis takes a major step towards studying superconductor-contacted carbon nanotubes in a circuit QED architecture. In addition to the earlier mentioned rich phenomena, this creates for example a possibility of implementing a new type of qubit formed by Andreev bound states in the nanotube and studying its interaction with the microwave field.

1 Hybrid Circuit QED

Conventional circuit QED architectures consist of one or several Josephson junction qubits integrated into a superconducting transmission-line resonator [1, 2, 3]. However, due to its potential in terms of modularity, circuit QED architecture has been intensively used to explore the physics of hybrid devices ranging from semiconducting quantum dots [17, 18, 19] to mechanical resonators [20, 21].

Recently, a variety of studies of carbon nanotubes embedded in cQED architectures have been reported. One of such studies demonstrates the coupling of a carbon nanotube quantum dot in Coulomb blockade and Kondo regimes to a single mode of a coplanar waveguide resonator [22]. An electron-photon coupling strength of 140 MHz is determined by probing the nanotube quantum dot using a dispersive readout. Another instance of embedding a nanotube in a microwave circuit demonstrates a distant interaction between two nanotube quantum dots mediated by the cavity photons [23].

More complex circuits based on nanotube double quantum dots have been studied in [24] and [25]. In the first study, the out-of-equilibrium charge dynamics in

the nanotube is probed with a microwave field. The authors extract characteristic parameters of the hybrid system, such as the relaxation and dephasing rates and the photon number. In the second paper by the same author, a spin-photon coupling is realized in a system consisting of a ferromagnet-contacted nanotube double quantum dot coupled to a resonator. A spin coherence time in the nanotube of 60 ns is determined from the measurements. In addition to these, in [26], a carbon nanotube based valley-spin qubit is studied. A coherent operation of the qubit via electrically driven spin resonance is demonstrated.

As mentioned earlier, this thesis aims to embed superconductor-contacted nanotubes in microwave resonators. The motivation for this stems from the idea to probe the Andreev physics in the nanotube with a microwave field. In addition, one can study an Andeev bound state qubit in a nanotube. Such qubit has been proposed by Zazunov *et. al.* in a superconducting quantum point contact embedded in a superconducting quantum interference device (SQUID)[27]. Coherent manipulation of the Andreev-level qubit in a circuit QED geometry has been recently demonstrated in atomic contacts [28, 29].

Being one-dimensional conductors, carbon nanotubes are good candidates for studying Andreev bound states. A single-walled carbon nanotube possesses only one conduction channel carrying two spin-opposite electrons. Andreev states come in pairs in each conduction channel, symmetric in energy with respect to the Fermi level [30]. Unlike the Andreev qubits based on atomic contacts, where multiple conduction channel exist, the Andreev qubit formed in a single-walled carbon nanotube is truly a two-level system.

2 SC-contacted nanotubes

A large variety of DC experiments on superconductor-contacted nanotubes has been reported [31, 32, 33, 34, 35]. When studying the superconductor-nanotube-superconductor systems, a special attention needs to be paid to the choice of the superconductor. Firstly, most of the commonly used superconducting metals result in high potential barriers at the contact interfaces with the nanotubes. On the other hand, some non-superconducting metals, such as Pd or Au, result in Ohmic contacts to the nanotubes [36, 37]. Therefore, in DC transport studies of nanotubes, superconductor/normal (SN) metal bilayers are used [35, 38]. SN bilayers become superconducting below some critical temperature due to the superconducting proximity effect [39, 40], which is the coherent propagation of the superconducting order into the normal metal at the interface.

The phenomena observed in SC-contacted nanotubes are the Andreev bound states and the multiple Andreev reflections (MAR). Andreev bound states are formed as a result of Andreev reflections of electrons and holes at the superconductor-normal metal interfaces due to the discontinuity of the superconducting phase [16]. These states are a key concept in mesoscopic superconductivity as they provide a universal description of Josephson-like effects in quantum-coherent nanostructures connected to superconducting leads [41, 42, 43, 44]. Recently, ABS have been observed in carbon nanotubes (CNTs) connected to superconducting electrodes [35, 45, 46].

Multiple Andreev reflection manifests itself as transport of the Cooper pairs from one lead to the other due to several consecutive Andreev reflections of particles at the interfaces. MAR has been studied in carbon nanotubes in different transport regimes, such as the Fabry-Pérot regime [33], Kondo regime [31, 32] and Coulomb blockade regime [34]. In this thesis we demonstrate the MAR processes and the

supercurrent through a nanotube due to ABS in different transport regimes, ranging from Coulomb blockade to Fabry-Pérot interference. We investigate the interplay of the superconductivity-mediated transport with each of these transport phenomena.

3 Thesis Overview

The present thesis begins with a theoretical background of the transport phenomena in carbon nanotubes in Chapter II. The general properties of carbon nanotubes are introduced followed by the theoretical description of quantum effects in nanotubes, including the Coulomb blockade, Kondo effect and Fabry-Pérot interference effects. In the second part of the chapter the theory of lumped element microwave LC resonators is presented. The quantization of the LC resonator is described. At the end, the concept of the Andreev level qubit is discussed and a possible coupling mechanism to the LC resonator is described.

Chapter III discusses the fabrication and the measurement techniques used in this work. The latter are separately described for DC measurements of nanotubes, microwave measurements of LC resonators as well as the measurements of coupled nanotube-microwave resonator devices.

Chapter IV discusses the DC transport measurements of carbon nanotubes contacted by normal and superconducting leads. The measurements of Coulomb blockade, Kondo effect and Fabry-Pérot interference are presented for normal contacts. The second part of the chapter presents the measurements of multiple Andreev reflection and supercurrent through the nanotube for superconducting metal contacted nanotubes. The interplay of the latter with the Fabry-Pérot interference showing a supercurrent transistor behaviour is discussed. At the end of the chapter, measurements of the multiple Andreev reflections in the Coulomb

blockade regime showing the four-fold degenerate shell structure of nanotube energy bands are introduced.

In Chapter V the RF measurements of lumped-element LC resonators are presented. In the first part of the chapter the measurements of two-port resonators made from two different metallic layers are discussed. The second part of the chapter introduces the measurements of the multiplexed LC resonators, where multiple resonators are coupled to a common transmission line. Studies of the superconducting proximity effect in Pd/Al bilayers is presented.

In the final chapter of this thesis, Chapter VI, the first RF measurements of a system consisting of a superconductor-contacted carbon nanotube embedded in a LC resonator are presented. The microwave simulations of this system with AnSYS HFSS software package are presented and compared to the measurement results. Coulomb blockade in a nanotube quantum dot is probed with a microwave field and the results are discussed at the end of the chapter.

The thesis ends with a conclusion and the future prospects of the presented studies.

II

Theoretical Concepts

Contents

1 Quantum Transport in Carbon Nanotubes 8
- 1.1 Carbon Nanotubes 8
- 1.2 Coulomb Blockade in Carbon Nanotubes 17
- 1.3 Higher Order Tunneling: Kondo Effect 26
- 1.4 Ballistic Transport: Fabry-Pérot interference 30

2 Superconducting Proximity Effect in carbon nanotubes 31
- 2.1 Andreev Reflection 33
- 2.2 Subharmonic gap structure: Multiple Andreev Reflections 36
- 2.3 Andreev Bound States 38
- 2.4 Experimental studies of superconductor-contacted carbon nanotubes 40

3 Superconducting Microwave Resonators for Circuit QED 41
- 3.1 Basic Theory of Parallel LCR Circuits 42
- 3.2 Transmission Model for Capacitively Coupled LC Resonator 43
- 3.3 Inductance of the Lumped Resonator 46
- 3.4 Temperature Dependence of the Quality Factor 47
- 3.5 Quantization of the LCR Resonator 48

4 CNT-SQUID Resonator Coupling 50
- 4.1 Carbon Nanotube RF SQUID 51
- 4.2 Inductive Coupling of CNT SQUID to MW Resonator . 53

1 Quantum Transport in Carbon Nanotubes

Carbon nanotube devices exhibit a large variety of physical phenomena when contacted by normal or superconducting leads [10, 47]. In these systems the transport regime strongly depends on the metal-nanotube contact transparency. It can range from low transparency Coulomb blockade associated with charge quantization to high transparency [48, 49] Fabry-Pérot interference associated with coherent wave properties of the charge carriers [11, 50]. For intermediate transparency regimes other phenomena such as Kondo effect can take place [13, 51, 52]. When the leads are superconducting, additional transport can occur owing to the Andreev reflections [31, 33, 35, 53]. In the following sections we discuss the theoretical background of these different transport regimes.

1.1 Carbon Nanotubes

With an atomic number of 6, Carbon is the 4th most abundant element by mass after Hydrogen, Helium and Oxygen. It forms more compounds that any other element, with almost 10 million pure organic compounds. Carbon nanotubes - long, thin cylinders of carbon, were discovered in 1991 by Sumio Iijima using a high resolution transmission electron microscope [54]. These are large macromolecules unique for their size, shape, and remarkable physical properties. Carbon nanotubes have sparked much excitement in recent years and a large amount of research has been dedicated to their understanding [55, 56, 57]. New physical properties are still being discovered and disputed. Depending on several characteristic properties, such as the diameter, length and chirality, nanotubes can have a broad range of electronic, thermal, and structural properties.

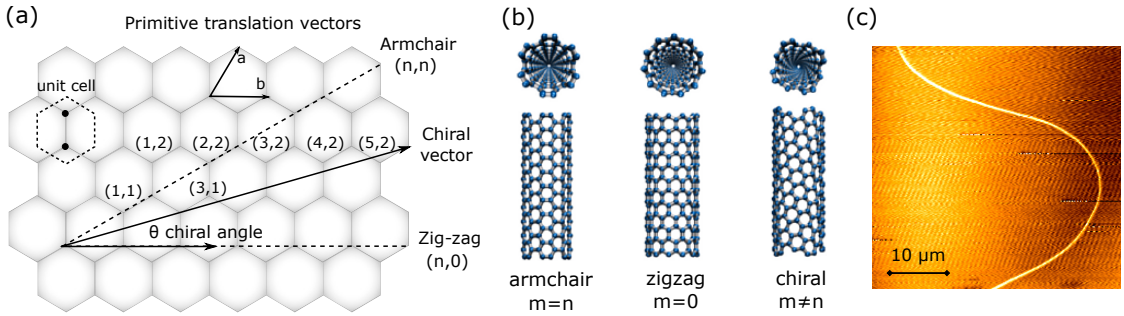


Figure II.1: a. Atomic force microscope picture of a carbon nanotube on a Si substrate, b. The honecomb lattice of carbon atoms showing the chiral vector and the unit cell, c. Three structures of nanotubes defined by the chiral vector.

1.1.1 Structural and Mechanical Properties

Carbon nanotube is formed by a layer of carbon atoms that are bound together in a hexagonal mesh. They can be thought of as rolled-up sheets of graphene. Nanotubes can be single-walled with diameters of 1-3 nm (SWNT) or multi-walled (MWNT) with diameters of 3 nm and higher. Single-walled nanotubes can have three different structures known as armchair, chiral and zigzag. The SWNT structure is characterized by a pair of indices (n,m) representing the chiral vector $\mathbf{C} = n\mathbf{a} + m\mathbf{b}$, where $\mathbf{a}$ and $\mathbf{b}$ are the primitive translation vectors (Fig.II.1b). Nanotubes can be divided into three structural classes defined by the chirality, namely zig-zag ($m = 0$), armchair ($m = n$) and chiral (arbitrary m, n), as illustrated in Fig.II.1b. Multi-walled carbon nanotubes have similar properties to single-walled nanotubes. The outer walls of multi-walled nanotubes protect the inner carbon nanotubes from chemical interactions with the medium they are in. There are two models which can be used to describe the structures of multi-walled nanotubes. In the Russian doll model, a larger nanotube contains a smaller one inside. In the Parchment model, a single graphene sheet is rolled around itself multiple times, resembling a rolled up scroll of paper [58]. The interlayer distance in multi-walled nanotubes is close

to the distance between graphene layers in graphite, approximately 0.33 nm. The walls in multi-walled nanotubes are held together by van der Waals force [59].

The nanotubes studied in the present work have diameters ranging from 1. 7nm to 2.5 nm, measured with atomic force microscopy (AFM). Therefore, they are believed to be single-walled. An atomic force microscope image of a nanotube is shown in Fig.II.1c.

Carbon atoms in the nanotube form sp^2 bonds, stronger than the sp^3 bonds in diamond, which result in a high tensile strength (higher than steel) and elasticity. A nanotube is weakened when defects such as vacancies and rearrangements of carbon bonds are present.

1.1.2 Electronic Band Structure

To describe the electronic band structure of a nanotube we consider the bonding of carbon atoms in a hexagonal or honeycomb lattice of a graphene sheet.

Each carbon atom has electron configuration of $1s^2 2s^2 2p^2$ (Fig.II.2a). The $1s^2$ atomic shell is fully occupied. The outer shell has one s and 3 p orbitals (p_x, p_y, p_z). The $2s$-$2p$ energy splitting is smaller than the typical bond energy, therefore all four outer orbitals can hybridize to form covalent bonds. In graphene, the p_z orbital, which is oriented perpendicular to the lattice plane, has odd parity, whereas $2s, 2p_x, 2p_y$ have even parities. Therefore, the latter can hybridize with each other (sp^2 hybridization) but not with $2p_z$ (Fig.II.2b). The sp^2 hybridization across the neighbouring atoms in graphene forms the low-energy σ band (bonding) and high energy $\sigma*$ band (antibonding) as shown in Fig.II.2c. The hybridization of p_z orbitals across the neighbouring atoms in graphene forms the π band (π and $\pi*$ respectively from bonding and antibonding of orbitals). In graphene, the σ band is filled with electrons and does not participate in transport. This results in transport

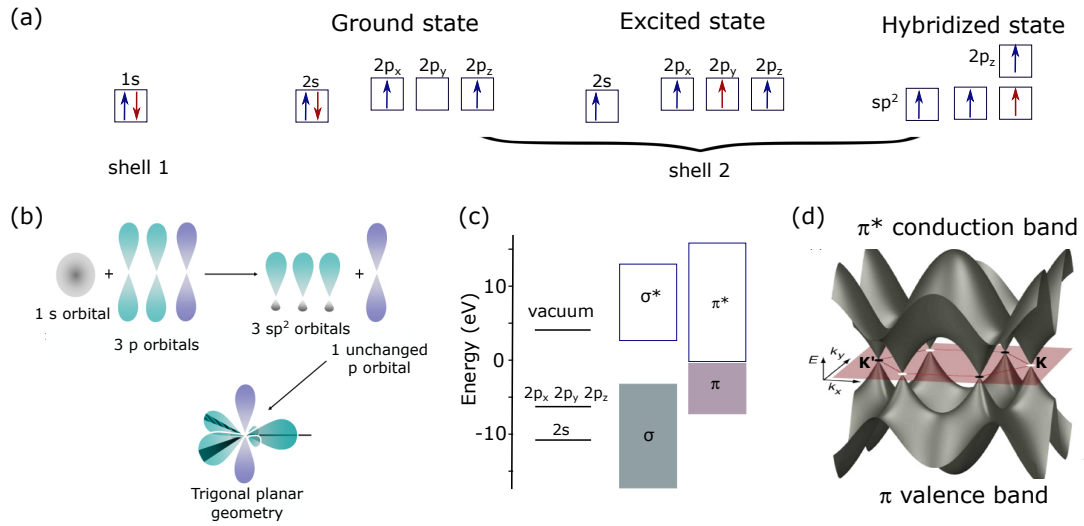


Figure II.2: a. Electronic configuration of a carbon atom, showing two shells. The inner shell has 1 s orbital occupied with a pair of spin up and spin down electrons. The outer shell consists of 1 s and 3 p orbitals. In the ground state 2s orbital is fully occupied and one of 2p orbitals is empty. In the excited state an electron from the 2s orbital occupies the empty 2p orbital. The sp^2 hybridized state of the orbitals is shown. b. sp^2 hybridization process leading to the trigonal geometry of the hybridized orbitals, c. The energy bands in the free and hybridized states. Due to the hybridization, low energy σ and high energy π bands are formed. d. Graphene band structure, calculated from the tight-binding model, showing the π and $\pi*$ bands intersecting at the Dirac points on the Fermi level.

properties being determined entirely by the π band. To construct the graphene band structure we consider the hexagonal lattice structure of carbon atoms. The corners of the Brillouin zone in k-space are labeled K (empty circles) and K$'$ (filled circles), known as Dirac points. Because the three K (K$'$) corners can be connected with reciprocal lattice vectors, according to Bloch's theorem they correspond to equivalent electron states. In the band structure arising from this the π and $\pi*$ bands intersect only at K and K$'$, where the density of states is zero. There is no bandgap and the electrons fill the π band, thus the Fermi level is exactly at the intersection of the two bands [47, 60, 61]. According to this, graphene is neither a true metal nor a semiconductor, but it is a semimetal.

The graphene band structure can be applied to nanotubes by imposing a periodic

boundary condition. This is called the "zone-folding approximation". The boundary condition can be written as $\mathbf{kC} = 2\pi n$, where $\mathbf{k}$ is the primitive translation vector in the reciprocal space, $\mathbf{C}$ is the chiral vector and n is an integer. On the other hand, the nanotube diameter can be expressed by the chiral vector $d = |\mathbf{C}|/\pi$ [61, 62]. Therefore, the component of $\mathbf{k}$ perpendicular to the nanotube axis and parallel to the chiral vector is given by $k_\perp = 2n/d$. Thus, the electron wave number perpendicular to the nanotube axial direction is only allowed to have quantized values, represented as discrete lines in the reciprocal space at a distance of $2/d$ (Fig. II.3a,c). Typically, the nanotube length is much larger than its diameter therefore the parallel component of $\mathbf{k}$ can be regarded to be continuous (infinitely long nanotube approximation). The one-dimensional dispersion relation of a nanotube can be obtained by taking a cross-section of the graphene band structure along the quantization lines (Fig. II.3b,d). Note that the transport properties are only influenced by the dispersion relation close to the Dirac points which form the so-called Dirac cones illustrated in the figure. If the quantization lines run through the Dirac points, then the one-dimensional dispersion relation is linear near $k_\parallel = 0$ with a crossing point at Fermi energy. This results in a zero bandgap and therefore a metallic nanotube. On the other hand, if the lines bypass the Dirac points at a distance of $\delta k_\perp$, the cross-section results in a nanotube dispersion relation of two hyperbolas with a bandgap of $E_g = 2\hbar v_F|\delta k_\perp|$. In this case the nanotube is semiconducting. The Fermi velocity $v_F = 1/h\, dE/dk \approx 8 \times 10^5 m/s$ is determined by the slope of the dispersion relation in the linear regime.

Early studies by Hamada *et. al.* [63] and Saito *et. al.* [64] showed a simple rule between the indices of the chiral vector, that determines the conducting properties of nanotubes. Namely, if $n - m$ is a multiple of 3, then the nanotube is metallic, otherwise it is semiconducting with a bandgap of $E_g = 4/3\hbar v_F d =$

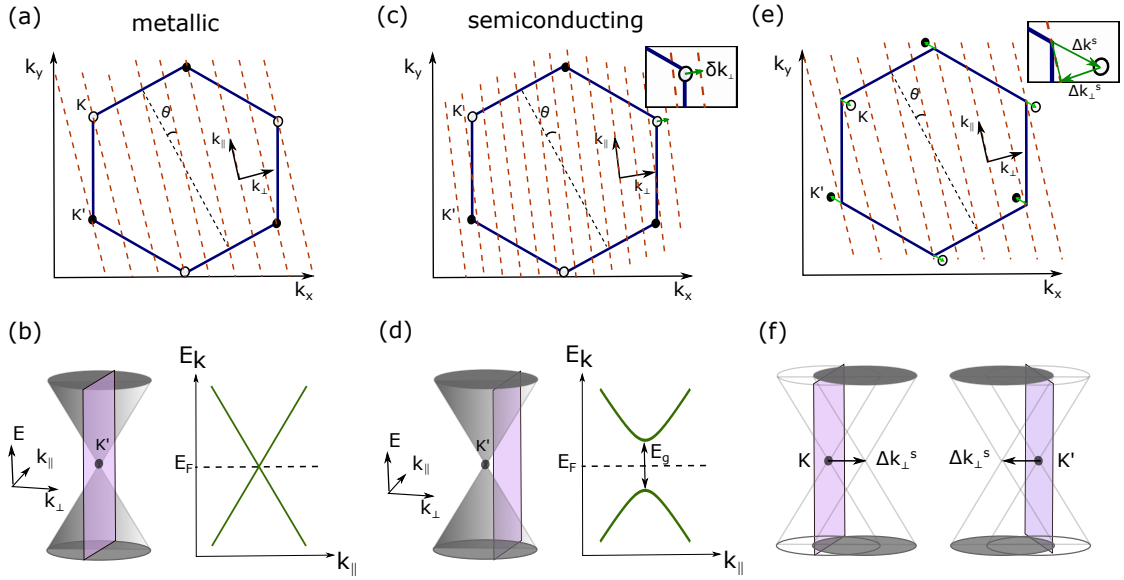


Figure II.3: a. Graphene unit cell in the k-space. The quantization lines of $k_\perp$ run through the Dirac points at an angle of $\pi/3 + \theta$ from the k_x axis, where θ is the chiral angle. b. The nanotube dispersion near the Dirac points is found by taking a cross-section at K and K′. When quantization lines intersect with Dirac points the dispersion relation is linear and no band gap exists at the Fermi level. Therefore, the resulting nanotube is metallic. c. The graphene unit cell superimposed with quantization lines of $k_\perp$ which do not intersect with the Dirac points. The inset shows the offset of quantization lines from K′ d. When a minimum offset of $\Delta k_\perp = 2d/3$ exists between the quantization lines and the K-points, a bandgap is formed in the nanotube dispersion relation and it is therefore semiconducting. e. Graphene unit cell superimposed with quantization lines for a metallic nanotube case. A curvature or strain of the nanotube results in a shift $\Delta k_\perp^s$ of Dirac points shown in the inset. f. The Dirac cones at K and K′ shifted from their original positions. A minigap exists in the dispersion relation due to the nanotube deformation, much smaller than a typical semiconducting nanotube gap.

$700\,meV/d$, where the diameter is given in nm. Thus, the armchair nanotubes are always metallic, whereas zigzag or chiral nanotubes can be either metallic or semiconducting. According to this, approximately 1/3 of nanotubes are metallic. However, experimentally even metallic nanotubes have a small bandgap. This gap is either strain-induced [65, 66, 67] or due to the curvature of the nanotube [68, 69]. The perturbation to graphene electronic band structure induced by rolling up leads to a small renormalization of the Fermi velocity. On the other hand, it results in a displacement of Dirac points in the k-space as a result of symmetry breaking between the 3 bond directions (Fig. II.3)e. In the figure, the shift of Dirac points due to

strain and curvature is introduced by the $\mathbf{\Delta k^s}$ vector, which has opposite directions for K and K′, as they are time-reversed conjugates of each other [60]. Due to this shift the Dirac cones are offset from the quantization lines as illustrated in Fig. II.3f resulting in a minigap in the 1D dispersion relation. The deformation-induced offset is typically much smaller than the quantization-induced offset in semiconducting nanotubes, therefore the curvature and strain deformations have a small effect on the bandgap of semiconducting nanotubes. On the other hand, in metallic nanotubes the deformation-induced shift of Dirac points results in a bandgap of $E_g^s = 2\hbar v_F|\Delta k_\perp^s|$, which is much smaller than the quantization energy difference. In the bandgap energy relation only the component of $\mathbf{\Delta k^s}$ parallel to $\mathbf{k}_\perp$ has an effect.

1.1.3 Metal - Nanotube Electrical Contact

Mechanical and electrical properties of carbon nanotubes make them promising candidates for elements in nanoelectrical circuits. Having ohmic contacts between CNT and metallic electrodes is therefore very important. Although nanotubes have intrinsically high conductivity, the high-resistance electrical contact between a nanotube and a metal hinders its practical applications. The small contact area between the nanotube and the metal makes it challenging to electrically couple the two.

Schottky Barriers Similar to conventional metal-semiconductor contacts [70], a Schottky barrier forms between carbon nanotube and metal electrodes. When using nanotubes for transistor applications or, as in our case, to study the Andreev states, low Schottky barriers and therefore low contact resistance is preferable. In contrast, in Schottky diodes used in high-frequency applications sufficiently high barriers are necessary [71]. Therefore it is very important to understand the formation of Schottky barriers for the correct design of nanotube devices.

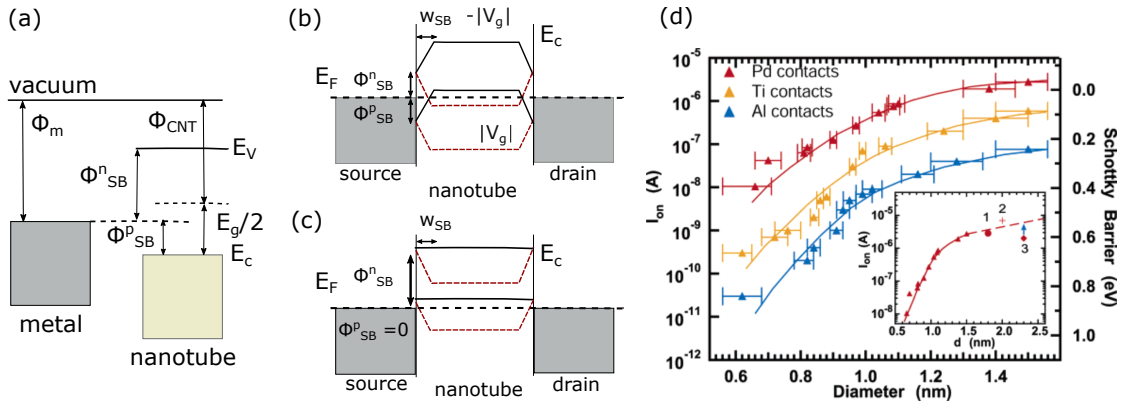


Figure II.4: a. A schematic of the nonaligned metal and nanotube energy levels depicting the relationship between the Schottky-barrier heights for hole and electron injection. ϕ_m and ϕ_{CNT} are correspondingly metal and nanotube work functions. ϕ^p_{SB} and ϕ^n_{SB} are Schottky barrier heights for electrons and holes. E_g is the nanotube gap energy. E_c and E_v are conduction and valence band energies. b. The situation when the Fermi level of the metal is at the mid-point of the nanotube gap. In this case, Schottky barriers for both electron (n) and hole (p) channels exist. c. p-type contacts, when a Schottky barrier exists for the electron, but not the hole transport. d. The nanotube field effect transistor on-state current as a function of the nanotube diameter for Pd, Ti and Al contacts (taken from [72]).

When a semiconducting nanotube is contacted by a metal, charge depletion at the interface leads to the bending of the nanotube energy bands and formation of Schottky Barriers (Fig. II.4b,c) [73]. The Schottky barrier height depends on the band alignment at the interface between the metal and CNT. Figure II.4a shows the case of misaligned Fermi levels. Assuming the Fermi level of an isolated nanotube is in the middle of the gap, the Schottky barrier height for electrons and holes can be written

$$\phi^p_{SB} = \phi_{CNT} + E_g/2 - \phi_m, \qquad \phi^n_{SB} = \phi_m + E_g/2 - \phi_{CNT}. \tag{II.1}$$

ϕ_m and ϕ_{CNT} are metal and nanotube work functions which are equal to the energy required to remove an electron from the Fermi level into vacuum. E_g is the semiconducting nanotube band gap, which is inversely proportional to its diameter.

The Schottky barrier width can be controlled by applying a gate voltage which tunes the energy levels. If the Fermi level of the metal is in the gap of the nanotube, a Schottky barrier exists for both electron (n) and hole (p) transport for respectively positive and negative gate voltages (Fig. II.4b). On the other hand, as illustrated in Fig. II.4c, if it is aligned with the hole band there will be no barrier for hole transport but a large barrier for electron transport. More generally, a metal with a high work function, such as Pd or Rh, will result in a better p-contact, whereas a metal with a low work-function like Al will result in a better n-contact.

The conductance of semiconducting nanotubes contacted by different metals has been studied in Chen *et. al.* [72]. In Fig. II.4c the 'on' state current of a nanotube device and the Schottky barrier height are plotted with respect to the nanotube diameter. For all diameters, the p-type Pd contacts result in the highest I_{on} and the Al contacts result in the lowest I_{on}. This observation closely follows the metal work function: 5.1 eV for Pd, 4.3 eV for Ti and 4.1 eV for Al. In these measurements, a large bias voltage was applied to overcome small interface barriers arising from contaminations and defects. As one can see in Fig. II.4c, Schottky barrier decreases with the increasing diameter (decreasing band gap). Zero Schottky barrier which is an Ohmic p-type contact is obtained only with Pd contacts to nanotubes of diameters larger than 1.5 nm.

Wettability High work function alone is not enough to ensure ohmic contacts between the the nanotube and the metallic electrodes. Pt ($\phi_{Pt} = 5.7$ eV), which has a higher work function than Pd ($\phi_{Pd} = 5.1$ eV), results in lower p-channel conductance [74]. Moreover, experiments show that even in case of metallic nanotubes the contact is far from ohmic [11]. The reason for this is the roughness and the chemistry of the contact interface. One can define a property describing how well the metal physically covers the tubular structure, known as wettability. When the wettability is poor, an

atomic-size physical gap forms between the CNT and the metal. A systematic study of electron beam evaporation coating of suspended SWNT with various metals reveals that Ti (Titanium), Ni (Nickel) and Pd (Palladium) form continuous and quasi-continuous coating, while Au (Gold), Al (Aluminum) and Fe (Iron) form only discrete particles on the SWNT surface [75]. In fact, Pd is a unique metal in that it consistently yields good contacts to both metallic and semiconducting nanotubes.

In conclusion, larger diameter nanotubes contacted by Pd will result in Ohmic contacts necessary for the present work. As mentioned before the nanotubes measured in this work have relatively large diameters of 2 ± 0.5 nm.

1.2 Coulomb Blockade in Carbon Nanotubes

At low temperatures, energy scales other than the thermal energy (e.g. Coulomb interaction energy, exchange interaction energy) play an important role in the transport characteristics. One of the well-studied quantum effects in nanotubes is the Coulomb blockade, where the charging energy of the quantum dot is the most important energy scale. Coulomb blockade in carbon nanotubes was first studied in detail by Bockrath et. al. in 1997 [49]. To understand the Coulomb blockade in nanotubes, we start by describing the quantum dot in a carbon nanotube.

1.2.1 Carbon Nanotube Quantum Dot

When a carbon nanotube is contacted by metallic electrodes, potential barriers are introduced for electron transport. When the resistance of these barriers is larger than the resistance quantum, $R_b \geq h/e^2$, the nanotube becomes isolated and forms a quantum dot. The logitudinal wave vector in the nanotube quantum dot has to fulfill the boundary conditions of standing wave solutions,

$$k_{\parallel} = \frac{n\pi}{L}, n = 1, 2, .. \tag{II.2}$$

where L is the nanotube length. Together with the quantization of the transverse component of the electron momentum described in Section II.1.1.2 this results in discrete energy levels in the nanotube. In this regime single electron charging effects can be observed in the system. Until today many experiments in CNT quantum dot have been done, where the system consists of a nanotube typically on a Si substrate contacted by source and drain leads and an electrostatic gate, which allows tuning of the QD levels [10, 50, 76]. A schematic picture of a typical nanotube device is illustrated in Fig. II.5b showing a nanotube quantum dot coupled to source and drain electrodes via capacitances C_S and C_G and coupling strengths Γ_S and Γ_D. A gate electrode is coupled to the nanotube via capacitance C_G, which is typically smaller than C_S and C_D.

The nanotube QD charging energy, which is the energy required to add an electron to the dot, is given by $E_c = e^2/C$, where C is the total coupling capacitance of the nanotube to its environment. E_c is typically in the meV range. Coulomb blockade is observed when $E_c > k_B T$. Fig. II.5a shows the schematics of the nanotube dot states coupled to metallic reservoirs via barriers. The figure shows the lead Fermi level broadening effect due to the finite temperature, as well as the charging energy that separates occupied and unoccupied states. The dot level spacing for metallic nanotubes and for semiconducting nanotubes far from the band gap is given by [61, 77]

$$\Delta = \hbar v_F \frac{\pi}{L}. \tag{II.3}$$

The nanotube devices measured in this work have typical section length of $200 - 300$ nm, which leads to a level spacing of few meV.

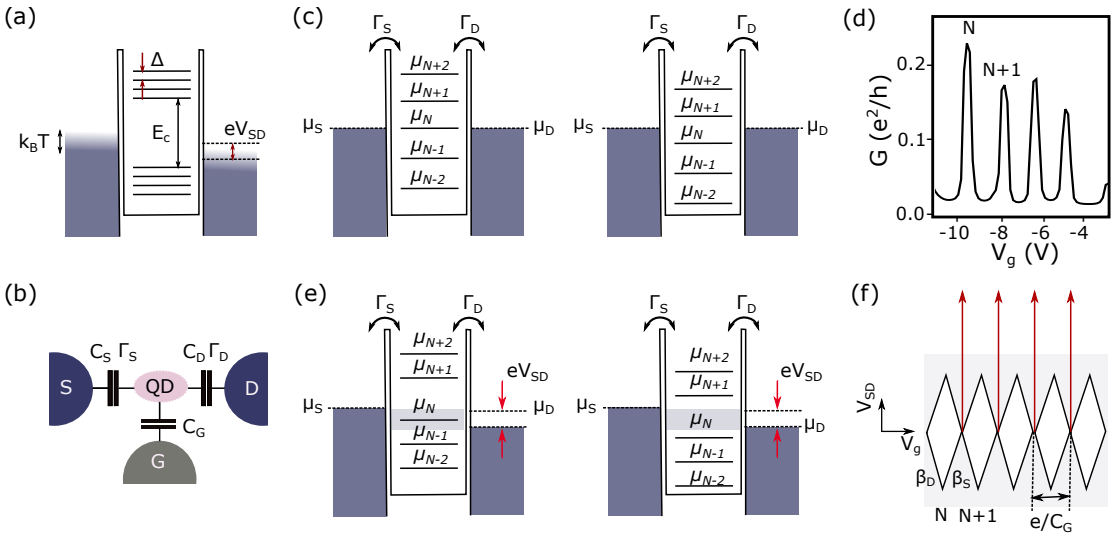


Figure II.5: a. Schematic of CNT dot coupled to metallic leads showing the temperature smearing of the lead Fermi energies. Δ is the dot level spacing, E_c is the charging energy and V_{SD} is the source-drain voltage. b. Schematic representation of the quantum dot coupled to source, drain and gate electrodes. C_S, C_D and C_G are coupling capacitances of the dot to source, drain and gate electrodes. Γ_S and Γ_D are tunneling rates to source and drain electrodes. c. Coulomb resonance (left) and blockade (right) regimes at zero bias voltage when the dot electrochemical potential μ_N is aligned (misaligned) with the lead Fermi energies. d. A measurement of differential conductance for different gate voltages showing the Coulomb resonances (nanotube device discussed in Section IV.1.1). N is the number of electrons on the dot. e. Coulomb blockade for non-zero bias voltage. If the dot level is in the bias window, particle transport takes place. f. Schematics of Coulomb blockade diamonds in the (V_{sd}, V_g) space, referred as the stability diagram. β_S and β_D are slopes of the diamond edges.

1.2.2 Single Electron Tunneling

As mentioned above, the nanotube quantum dot charging energy is inversely proportional to the total capacitance to the environment. In a typical configuration depicted in Fig.II.5b, this capacitance is the sum of capacitances to source, drain and gate electrodes, $C = C_S + C_D + C_G$. One can then write the energy of a quantum dot with N electrons as

$$E_N = \frac{(-|e|(N - N_0) + C_S V_S + C_D V_D + C_G V_G)^2}{2C} + \sum_{n=1}^{N} E_n \qquad \text{(II.4)}$$

Here N_0 is the number of electrons when no voltage is applied to either of the

electrodes. V_S, V_D and V_G are the potentiels of source, drain and gate electrodes. The first term is the electrostatic energy of the capacitors, whereas the second term is the sum of quantum energies of all occupied states. The energy required to occupy a new level with a single electron, known as the electrochemical potential of the dot, is given by

$$\mu_N = E_N - E_{N-1} = N\frac{e^2}{C} - \frac{|e|}{c}\sum_i C_i V_i + E_N \tag{II.5}$$

The electrochemical potential ladder of the quantum dot is illustrated in Fig.II.5c. To move the ladder one uses the capacitively coupled gate electrode. A change in the gate voltage δV_G results in a shift of $\delta\mu_N = -|e|\alpha_G\delta V_G$, where $\alpha_G = C_G/C$ is called gate lever arm, which is a measure of the gate efficiency. Consider the case with no source-drain bias. When μ_{N+1} is aligned with the lead Fermi energies (Fig. II.5c, left), a resonant tunneling of electrons through the dot takes place. This results in a resonance in the conductance measurement of the device. Otherwise, if the Fermi energy of the leads is between two electrochemical potential levels (Fig. II.5c, right), the transport through the dot is blocked (Coulomb blockade regime). Electrons in the source do not have enough energy to tunnel into E_{N+1} and at the same time, because the lead electrochemical potential is higher than μ_N the dot cannot relax to E_{N-1}. Fig. II.5d shows a differential conductance measurement of Coulomb resonances while the gate voltage is tuned on the x-axis. The spacing between two resonant peaks, referred to as the addition energy, is given by

$$E_{add} = \mu_N - \mu_{N-1} = \frac{e^2}{C} + \Delta, \tag{II.6}$$

where Δ is given by Eq. II.3.

1.2.3 Amplitude and lineshape of Coulomb peaks

The thermal broadening of the lead Fermi levels leads to a finite widths of the resonance peaks. Besides the thermal broadening, an intrinsic broadening of the quantum levels exists due to their finite lifetime as a consequence of the Heisenberg uncertainty principle. This means that in infinitely short period of time electrons with energies close but not equal to the dot level energy can tunnel through the dot. One can define a tunneling rate through the dot, $\Gamma = \Gamma_S + \Gamma_D$, where Γ_S and Γ_D are couplings to the source and the drain. If we ignore the thermal broadening of the levels, the intrinsic shape of the Coulomb resonance is

$$G(\epsilon) = g\frac{e^2}{h}\frac{\Gamma_S\Gamma_D}{\Gamma_S+\Gamma_D}\frac{\Gamma}{(\epsilon/\hbar)^2+\Gamma^2/4}, \tag{II.7}$$

where g is the degeneracy of the dot level, which is 4 for nanotubes due to spin and orbital degrees of freedom [78]. ϵ is the distance of the dot electrochemical potential from the Fermi level of the leads. According to this, the maximum value of the Coulomb resonance is

$$G_{max} = 4\frac{e^2}{h}\frac{4\Gamma_S\Gamma_D}{(\Gamma_S+\Gamma_D)^2}, \tag{II.8}$$

which can be used to calculate the dot coupling asymmetry to the contacts.

1.2.4 Charge Stability Diagram and Coulomb Diamonds

At zero bias, the conductance through the dot is suppressed between two resonant peaks. In this case the dot is sitting in a "Coulomb valley" with fixed number of electrons on it. One can overcome the blockade regime by applying a finite bias voltage across the dot (Fig.II.5e). In this case, the electrochemical potentials of the leads are shifted with respect to each other by eV_{sd}, forming a bias window in

the quantum dot. If μ_N is tuned into the bias window using the gate, tunneling through the dot is allowed, otherwise, it is blocked.

The charge stability diagram of the dot, which is the plot of the differential conductance of the device versus gate and bias voltages, shows Coulomb blockade peaks evolving as straight lines away from $V_{SD} = 0$ (Fig. II.5f). Completing this plot leads to the formation of Coulomb diamonds, inside of which the tunneling through the dot is blocked. The edges of the diamonds correspond to $\mu_N = \mu_S$ (positive slope β_S) or $\mu_N = \mu_D$ (negative slope β_D). The width of the diamond is equal to e/C_g. To find the slopes, we assume that the drain voltage is fixed at $\mu_D = 0$. When $\mu_N = \mu_D$, using Eqn.II.5 one obtains $0 = V_{SD}C_S/C + V_G C_G/C$, therefore the negative slope is given by

$$\beta_D = V_{SD}/V_G = -C_G/C_S. \tag{II.9}$$

In the second case, $\mu_N = \mu_S$, $V_{SD} = V_{SD}C_S/C + V_G C_G/C$, therefore

$$\beta_S = C_G/(C_G + C_D). \tag{II.10}$$

The slopes can be easily calculated from the measurements, which allows estimating the coupling capacitances.

1.2.5 Excited States

So far we have only considered the electron transport through the ground states of the nanotube quantum dot. If the tunneling rate exceeds the relaxation time of an excited state of the quantum dot, transport through this state becomes possible. The quantum dot chemical potential can be written as $\mu_N^{(n,m)} = E_N^m - E_{N-1}^n$, where n and m are the single particle states and N is the number of electrons on the dot as before. For a transport involving the n-th excited state to occur, both $\mu_N^{(n,0)}$

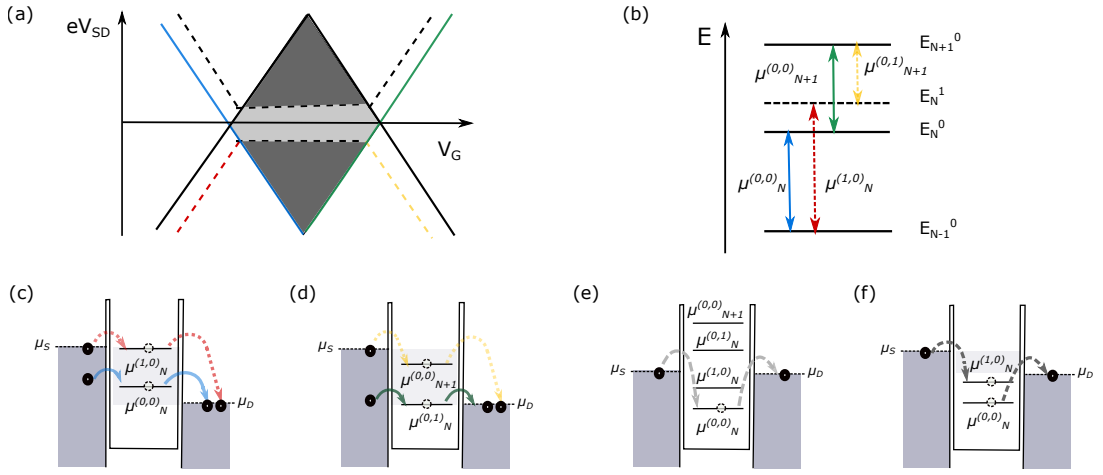


Figure II.6: a. The charge stability diagram of a quantum dot in the (V_{sd}, V_g) plane. The solid diamond edges correspond to alignment of a dot level with the Fermi energy of the leads, resulting in first order tunneling as illustrated in c and d. In the light gray region the conduction is due to the elastic co-tunneling shown in e, whereas the dark gray region is due to the inelastic co-tunneling shown in f. b. The energy diagram of the quantum dot showing the additional excited state E_N^1. Additional electrochemical potential values of the dot due to the excited state are $\mu_N^{(1,0)}$ and $\mu_{N+1}^{(0,1)}$.

and $\mu_N^{(0,0)}$ must be within the bias window. This results in additional resonances appearing in the charge stability diagram, shown in Fig. II.6a as dashed lines parallel to the Coulomb diamond edges. Fig. II.6b shows the corresponding transitions involving ground and excited states. The transport through the dot in both cases is illustrated in detail in Fig. II.6c,d.

The transport discussed so far involved only dot electron number fluctuations by a single electron. This is referred as sequential tunneling. However, higher order tunneling processes are possible. An example of this is the second order tunneling, otherwise called elastic co-tunneling (Fig. II.6e). In this case, one electron enters the dot and the second electron leaves the dot within the Heisenberg uncertainty time $\tau \approx \hbar/E_c$. The current flowing through the dot due to the elastic co-tunneling is proportional to the bias voltage, $I_{el} \propto |e|V_{sd}\frac{\Gamma_S\Gamma_D}{E_c^2}$. Therefore, the differential conductance due to elastic co-tunneling is constant (light gray area in Fig. II.6a). When the bias voltage is larger than the lowest on-site excitation energy, inelastic

co-tunneling events become possible (Fig. II.6f). For instance, an electron can leave from the ground state to the lower Fermi energy of the leads, while another electron enters the dot excited state from the higher Fermi energy of the leads. The excitation is created at the expense of the energy eV_{sd}. This results in a step-like increase in the differential conductance shown in Fig. II.6a as the dark gray region, which is only weakly gate-dependent.

1.2.6 Four-fold Shell Filling

The model to describe quantum dots considered so far is the constant interaction model, which assumes that the charging energy is constant and independent on the occupied single particle states. To describe carbon nanotube quantum dots, this model has been extended to include the following independent parameters [79]: the charging energy E_c, the energy level spacing Δ, the orbital subband mismatch δ, the exchange energy J and the excess Coulomb energy of two electrons occupying the same level dU. J is the energy gain when two electrons have parallel spins compared to the anti-parallel configuration.

The nanotube band structure exhibits twofold orbital symmetry corresponding to the K and K$'$ subband degeneracy, resulting from the equivalence of the two atoms in the graphene primitive cell. For simplicity, we consider a metallic nanotube with a linear dispersion relation shown in Fig. II.7a. The quantization of the electron wave number along the nanotube axis results in equidistant energy levels. These energy levels in the two subbands are shifted by the band mismatch δ. Taking into account the twofold spin degeneracy, this yields four-fold periodicity in the electron addition energy [76, 80, 81]. Fig. II.7a and b qualitatively describe the nanotube quantum dot energy scales.

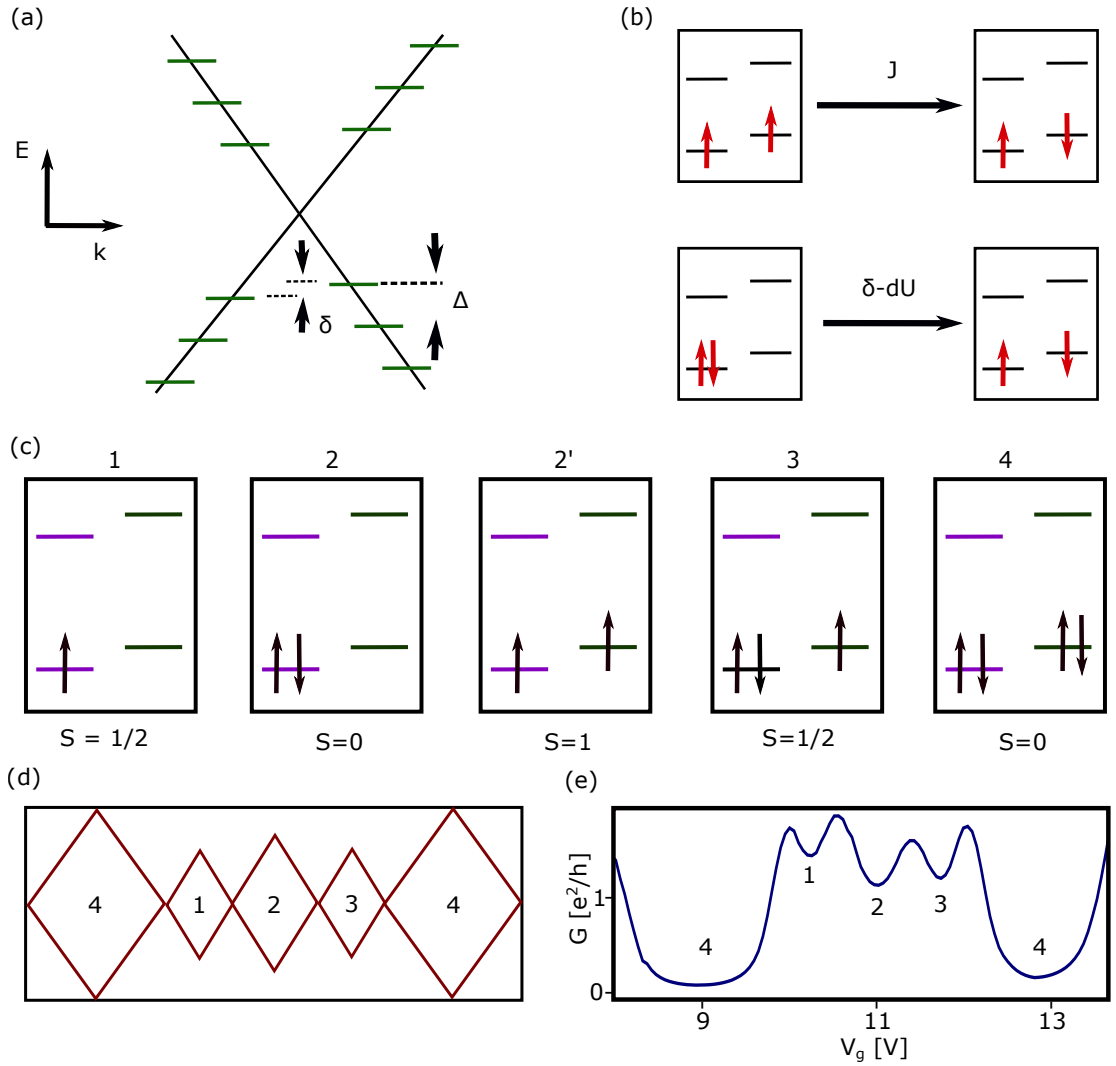


Figure II.7: a. Band structure of a metallic nanotube. δ is the subband mismatch and Δ is the quantum level separation in each band. b. Exchange energy J, which is the enrgy gain between spin-parallel and spin-opposite configurations. Excess Coulomb energy dU, which is the interaction energy of two electrons occupying the same level. c. Two scenarios of shell filling corresponding to spin-singlet (2) and spin-triplet ($2'$) configuration of the two electron ground state. d. Schematic picture of the stability diagram showing a large diamond followed by three smaller diamonds due to the four-fold periodicity of the dot addition energy. e. Measurement of the differential conductance of a device discussed in Section IV.2.3 when tuning the gate voltage. The four-fold shell filling manifests itself as a large conductance valley, followed by four small conductance peaks at the Coulomb resonances.

The nanotube quantum dot level spacing Δ is typically larger than the excess Coulomb energy dU and the exchange interaction energy J. Therefore, two possible spin-filling scenarios exist. When $J + dU < \delta$, lower energy levels are first filled with pairs of spin-opposite electrons resulting in a sequence of net spins $S = 1/2$, $S = 0$, $S = 1/2$, $S = 0$ (Fig II.7c, sequence $1, 2, 3, 4$). In the second scenario, when $J + dU > \delta$, the resulting net spin follows $S = 1/2$, $S = 1$, $S = 1/2$, $S = 0$ (Fig II.7c, sequence $1, 2', 3, 4$). In the first case, the ground state of the two electrons is a spin-singlet, whereas in the second case it is a spin-triplet. From the Oreg model [79], the addition energy for the N-th electron is obtained as,

$$\Delta\mu_1 = \delta\mu_3 = E_c + dU + J \tag{II.11}$$

$$\Delta\mu_2 = E_c + \delta - dU \tag{II.12}$$

$$\Delta\mu_4 = \delta\mu_3 = E_c + \Delta - dU - \delta. \tag{II.13}$$

Experimentally, the four-fold shell filling of a nanotube quantum dot is observed as three small conductance gap regions followed by a large conductance gap region (Fig II.7d). One can extract the energy parameters characterizing the quantum dot by estimating the addition energy $\Delta\mu_N$ corresponding to each diamond and equating them to Eqn.II.11-II.13. Fig II.7e shows a measurement of differential conductance as a function of the gate voltage in one of the devices studied in Chapter IV, where the four-fold shell filling pattern is observed by a large conductance gap followed by four conductance peaks.

1.3 Higher Order Tunneling: Kondo Effect

The field of Kondo physics has been studied since the 1930s. Low temperature experiments showed that metals containing ferromagnetic impurities show increase in resistance below a characteristic temperature ([82, 83]). Until then, only two

types of temperature dependence of resistance of metals were known. Most of the metals show a gradual decrease in resistance up to a saturation point for $T \to 0$. A second class of metals, known as superconductors, display a sudden drop of the resistance to a very low value below a critical temperature.

In 1964 Jun Kondo [84] and later on Appelbaum [85], Anderson [86] and Wilson [87] were able to successfully explain the unusual behaviour of resistance with an enhanced scattering probability due to the screening of spin impurities (Kondo cloud).

More recently, the Kondo effect was studied in mesoscopic physics. In 1998 its first observation was made in semiconductor quantum dots [51, 88]. The revival of the Kondo effect in mesoscopic physics partly owes to the fact that its appearance in these systems is highly tunable (by tunnel-coupling, temperature or gate potential). In quantum dots, Kondo effect results in an increased conductance with a peak at zero-bias. This is in contrast to the expected resistance increase for a bulk metal containing magnetic impurities.

1.3.1 The Quantum Model

In this section we introduce a qualitative explanation of the conductance increase in quantum dots due to the Kondo effect. The role of the impurity is played by an unpaired spin on the dot energy level. We consider a quantum dot, which is in our case a nanotube, coupled to source and drain leads through Γ_S and Γ_D tunneling rates. For simplicity, we assume the dot has a single energy level ϵ occupied with a spin up or a spin down electron. The net spin of the dot is $S = 1/2$ (Fig. II.8a). Addition of a second electron costs an on-site Coulomb energy $E_c = e^2/C$. Therefore, one requires a total of $E_c + \epsilon$ energy to add the second electron, but as this energy is larger than the lead chemical potentials μ_S and μ_D, electrons cannot tunnel from

leads into the dot. On the other hand, $\epsilon < \mu_S, \mu_D$, therefore the electron on the dot cannot tunnel out. However, within a timescale given by the Heisenberg uncertainty principle, $\tau \approx \hbar/E_c$, higher order tunneling processes are allowed. In this case we are interested in processes that cause an effective spin-flip of the dot electron. This is illustrated in Fig. II.8a. Within the time τ the quantum dot spin tunnels into the drain lead and at the same time an opposite spin tunnels from the source lead into the dot. In this spin-flip process the dot goes through a virtual state depicted in the figure. The sum of all successive spin-flip processes effectively screens the local spin on the dot such that the electrons in the leads and on the dot together form a spin-singlet state. Analogous to the singlet state formed by the magnetic impurity in a metal, this macroscopically correlated state gives rise to the Kondo effect. The so-called Kondo cloud of the screening spins results in enhanced scattering, which in bulk metals increases the resistance. On the other hand, in quantum dots this scattering is a transport mechanism therefore it increases the conductance. The Kondo effect in a quantum dot manifests itself as a peak in the dot density of states (DOS) at the lead chemical potential $\mu_S = \mu_D$. The experimental fingerprint of the Kondo effect in the stability diagram is a line of increased conductance at zero bias across the odd-spin Coulomb diamond (Fig. II.8b). Experimental results illustrating this effect are discussed in Section IV.1.2.

1.3.2 Kondo Temperature

Kondo effect is described with a characteristic temperature T_K, above which the enhancement of the conductance in quantum dots (resistance in metals) vanishes. Below T_K the temperature dependence of the zero-bias Kondo conductance follows a simple formula obtained using numerical renormalization group calculations [89]:

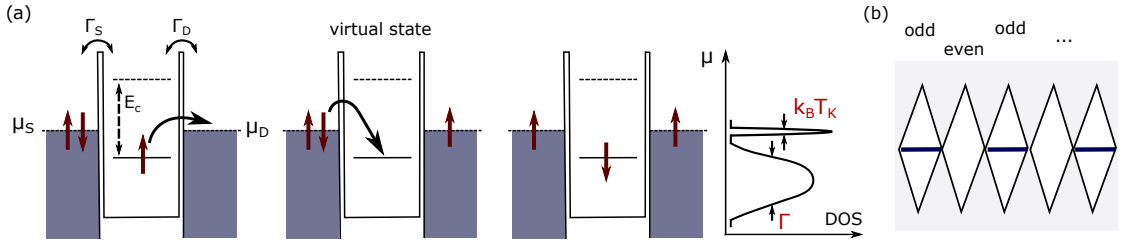


Figure II.8: a. Kondo effect in a quantum dot. Γ_S and Γ_D are the tunneling rates to the source and drain leads. $\Gamma = \Gamma_S + \Gamma_D$ is the quantum dot level broadening. The spin-scattering event due to a virtual spin-flip of the quantum dot spin is illustrated. Kondo effect results in a resonant peak in quantum dot DOS with a width given by the so-called Kondo temperature (see Section II.1.3.2). b. Stability diagram showing Kondo resonances at zero-bias in the odd valleys of the quantum dot net spin.

$$G(T) = G_0\left(\frac{T_K'^2}{T^2 + T_K'^2}\right)^s \tag{II.14}$$

In the equation above $T_K' = T_K/\sqrt{2^{1/s} - 1}$ and therefore $G(T_K) = G_0/2$. s is a fitting parameter and has been found to be $s = 0.22 \pm 0.01$ for a spin-1/2 impurity. Qualitatively, the Kondo temperature corresponds to the binding energy of the spin-singlet formed with the single spin on the dot and the screening spins in the leads. In the single Anderson impurity model [90] T_K is given by

$$k_B T_K = \frac{(\Gamma E_c)^{1/2}}{2} e^{\pi\epsilon(\epsilon + E_c)/\Gamma E_c}, \tag{II.15}$$

where $\Gamma = \Gamma_S + \Gamma_D$ as before, and ϵ is the level position calculated from the lead Fermi level. One can notice that T_K strongly depends on the dot level position ϵ and therefore the gate potential. Kondo temperature is the largest at the degeneracy points $\epsilon = 0, -E_c$, therefore the closer to these points the larger temperature range can be investigated.

Kondo effect in carbon nanotubes has been studied shortly after its observation in quantum dots [13, 31]. Its interplay with the superconducting proximity effect has also been studied, as we will cover in Section II.2 [38, 50].

1.4 Ballistic Transport: Fabry-Pérot interference

Carbon nanotube is a one-dimensional conductor. Different scattering mechanisms affect the electron momentum relaxation length, L_m (mean free path), and the phase relaxation length L_ϕ differently. For example, elastic scattering limits the mean free path but does not affect the phase. On the other hand, inelastic scattering affects both. The relation between these length-scales or their equivalent timescales ($t = L/v_F$, $v_F = 8.1 \times 10^5$ m/s for nanotube) determines whether the transport is ballistic, diffusive or dissipative [91]. Diffusive and dissipative transport happen correspondingly for $L_m << L$ and $L_\phi < L$. Otherwise, when the nanotube length $L << L_m, L_\phi$, ballistic transport of particles takes place through the nanotube. High-transparency contacts and defectless nanotubes necessary to observe ballistic transport must be achieved in growth and fabrication process. In this case, each channel contributes $2e^2/h$ to the conductance, where the factor 2 is due to the spin degeneracy. Considering also the orbital degeneracy due to K and K′ points, the overall maximum conductance through a single channel is $G_{max} = 4e^2/h \approx (6.45\,\mathrm{kOhm})^{-1}$. In experiments this value is decreased due to intrinsic defects and non-ideal contacts with the electrodes.

The observation of ballistic transport in nanotubes giving rise to Fabry-Pérot interference was first achieved by Liang et. al. in 2001 [11]. Since then, similar results have been obtained by multiple groups [74, 92, 93, 94]. Fabry-Pérot interference is the quantum interference of electron wave functions reflected from the metal-channel interfaces, analogous to the light transmission in an optical Fabry-Pérot cavity. Two metal-nanotube interfaces correspond to partially reflecting mirrors. Similar to photons in the Fabry-Pérot cavity, electrons experience multiple reflections between the two barriers separating the metal reservoirs from the SWNT before

escaping (Fig. II.9a). The theoretical model is based on the Landauer-Büttiker formalism which takes into account spin and orbital degeneracies [95, 96]. Fabry-Pérot interference results in conductance oscillations with changing bias and gate voltages (Fig. II.9b). The stability diagram shows a checkerboard pattern as illustrated in the Fig. II.9c adopted from [11]. This pattern can be qualitatively described as follows. As the gate voltage is swept, the energy of the Fermi level with respect to the bottom of the subband (or neutrality point in a metallic nanotube) is changed, and the wavevector of the injected carriers is correspondingly modulated. The wavevector is similarly modulated by changing the source-drain bias voltage. Phase is accumulated as carriers traverse the nanotube, and when the round-trip phase shifts by 2π, the conductance undergoes an oscillation. The energy scale δE_{FP} of these oscillations is found by setting the round-trip phase shift equal to 2π,

$$2Le\frac{\delta E_{FP}}{\hbar v_F} = 2\pi. \tag{II.16}$$

Therefore, one can use the distance between the two maxima to estimate the length of the nanotube Fabry-Pérot cavity. For ballistic transport this length is theoretically equal to the contacted nanotube length and the electron reflections happen at the nanotube/metal interfaces. Experimental results of Fabry-Pérot interference in nanotubes are presented in Chapter IV Section 1.3.

2 Superconducting Proximity Effect in carbon nanotubes

In hybrid structures, where a superconductor (S) is in contact with a non-superconducting (hereafter normal) material, the electron pairs in the superconductor propagate into the normal (N) material and 'contaminate' it with superconducting properties. This phenomenon, referred to as superconducting proximity effect has been heavily

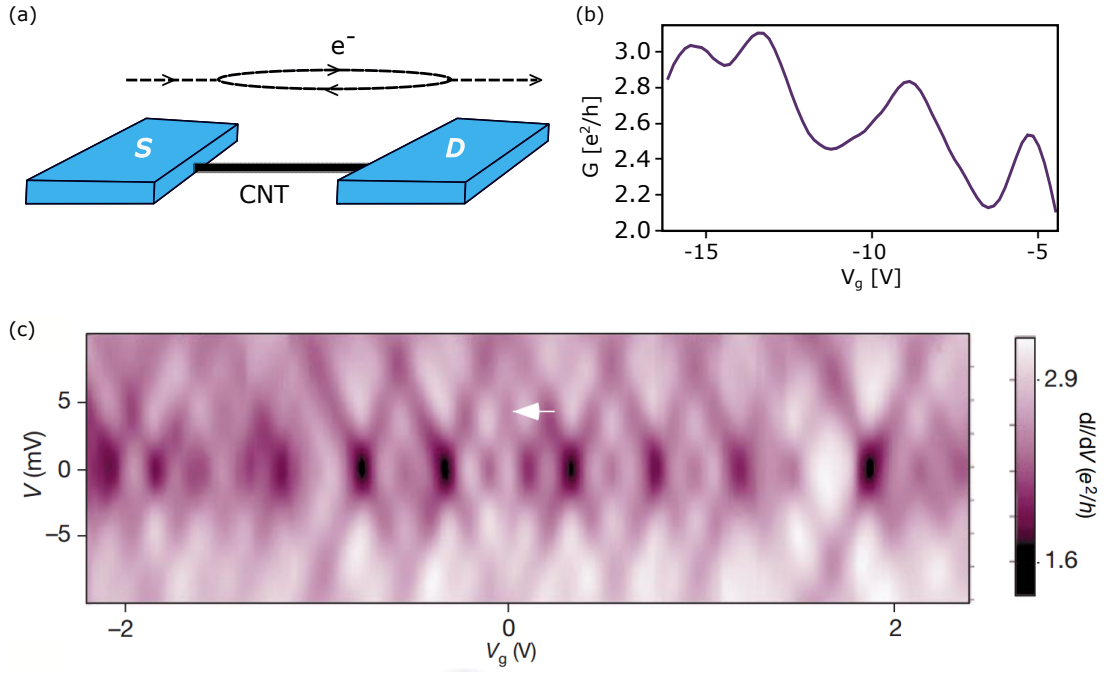


Figure II.9: a. Schematic diagram of a carbon nanotube contacted by two metallic electrodes. Electron wave functions reflected from the contact interfaces interfere with each other giving rise to conductance oscillations. b. Measurement of a differential conductance of a nanotube device discussed in Chapter IV when tuning the gate voltage. Broad oscillations of the conductance are observed due to the Fabry-Pérot interference. c. Stability diagram of a nanotube device in Fabry-Pérot regime showing the checkerboard pattern resulting from conductance oscillations with bias and gate voltages (adopted from [11]).

investigated and theoretically explained shortly after the discovery of the BCS theory of superconductivity [97, 98, 99]. This was additionally driven by the developing microfabrication techniques allowing to construct hybrid heterostructures. The proximity effect exists in various S-N systems, where N can be molecules (graphene, carbon nanotube, fullerene) [33, 100, 101], diffusive normal metals [102], ferromagnetic materials [103, 104], semiconductors (two dimensional electron gas or nanowires) [105, 106] and atomic contacts [107]. In all of these systems its strength and penetration depth depend on the electronic properties of the materials and the quality of the contact interface. The qualitative explanation of the proximity effext in all of the above mentioned systems can be given using the key concepts of the

proximity effect: Andreev reflection and Andreev bound states [16]. These concepts are well-explained in the framework of Bogoliubov-de Gennes (BdG) formalism introduced in the following section [108].

2.1 Andreev Reflection

Andreev reflection is the main transport mechanism of particles at the superconductor-normal material interface. In 1964 A. F. Andreev [16] and de Gennes and Saint-James [97, 99] independently found that an incident electron from the normal region has a finite probability of reflecting as a hole at the S-N interface. To understand this process, we recall that the quasiparticles in superconductor at the Fermi energy are Cooper pairs [109], therefore for an electron with energy smaller than the superconducting gap there are no states available in the superconductor. Moreover, in the absence of a barrier at the N-S interface, the incident electron does not undergo a normal reflection process. At the interface, the incident electron combines with another electron from the Fermi sea of the normal conductor to form a Cooper pair, which condenses in the ground state of the superconductor (Fig. II.10). When the electron from the Fermi sea of the normal conductor is combined with the incident electron, it leaves behind a hole. This hole is retroreflected in the opposite direction and follows the path of the incident electron. For simplicity, we restrict ourselves to the 1D case, such that the inhomogeneity of the superconducting order parameter Δ changes only in x direction. When the normal material is a weak link connected to a massive superconductor, the order parameter is assumed to be a step function. This turns out to be a very good approximation for many experimental studies. When inhomogeneous superconductivity exist in a system, it can be described by

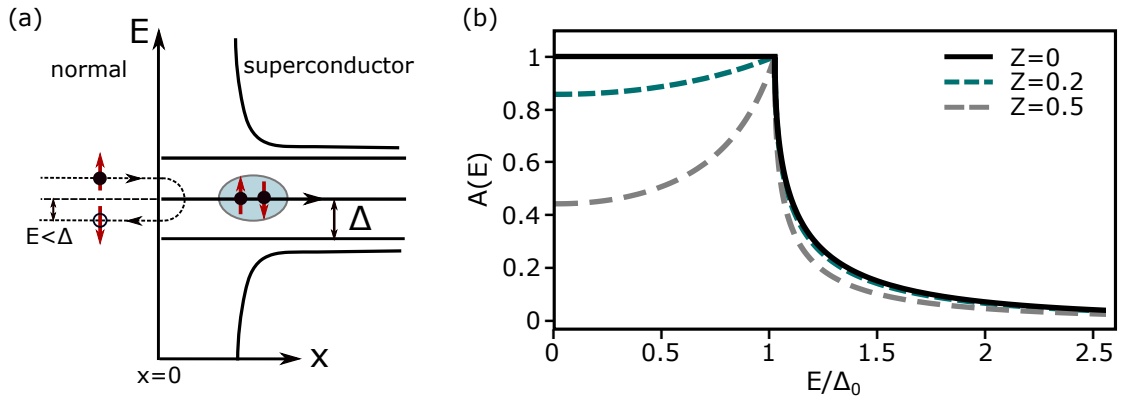


Figure II.10: a.Andreev reflection of a single electron with energy E at the normal-superconductor interface. As a result, a hole with energy $-E$ is reflected into the normal region causing a Cooper pair transfer into the superconducting region. b. Andreev reflection probability depending on the incident particle energy for different interface barrier heights.

an effective Hamiltonian that consists of 'normal' and 'pairing interaction' terms.

$$H_{eff} = H_N + H_S = \sum_{k,\sigma=\uparrow\downarrow} \xi_{k,\sigma} a^+_{k,\sigma} a_{k,\sigma} + \sum_k \Delta_k a^+_{k,\uparrow} a^+_{-k,\downarrow} + \Delta^*_k a_{-k,\downarrow} a_{k,\uparrow} \qquad \text{(II.17)}$$

$a^+_{k,\sigma}(a_{k,\sigma})$ is the creation (annihilation) operator of an electron in the state (k,σ). The electron has a kinetic energy ${\xi_{k,\sigma}}^*$ and it pairs up with another electron in a conjugate state $(-k,-\sigma)$ with a potential

$$\Delta_k = \int \phi_{k,\uparrow^*(x)} \Delta(x) \phi^*_{-k,\downarrow}(x). \qquad \text{(II.18)}$$

The complex order parameter $\Delta(x) = |\Delta(x)| e^{i\phi(x)}$ describes the inhomogeneous superconductivity and $\phi_{k,\uparrow}(\phi_{-k,\downarrow})$ is the wave function of the corresponding state.

Bogoliubov-de Gennes equations are obtained by diagonalizing the Hamiltonian in II.17 in Nambu space. The result is shown in the following matrix equation

$$\begin{bmatrix} \xi_{k,\uparrow} & \Delta_k \\ \Delta^*_k & -\xi_{-k,\downarrow} \end{bmatrix} \begin{bmatrix} u_k \\ v_k \end{bmatrix} = E \begin{bmatrix} u_k \\ v_k \end{bmatrix}. \qquad \text{(II.19)}$$

*For a single particle, $\xi_{k,\sigma} = \hbar^2 k^2/2m - E_F + V(r)$, where m is the electron effective mass, E_F is the Fermi energy and $V(r)$ is the scalar potential.

It has two eigenvectors, $|k_+\rangle = \begin{bmatrix} u_{k+} \\ v_{k+} \end{bmatrix}$ and $|k_-\rangle = \begin{bmatrix} u_{k-} \\ v_{k-} \end{bmatrix}$ with eigenvalues ϵ_{k_+} and ϵ_{k_+}. u_k and v_k are electron-like and hole-like quasiparticle amplitudes. For a homogeneous superconductor $\Delta_k = \Delta_0$ they are given by [110]

$$\begin{aligned} u_0 &= \frac{1}{2}(1 + \frac{\sqrt{E^2 - \Delta_0^2}}{E}) \\ v_0^2 &= 1 - u_0^2. \end{aligned} \tag{II.20}$$

To find the solutions of BdG equations for step-function potential, fundamental systems of solutions are found separately for N and S regions. These are then matched across the interface so that both the wave functions u_k and v_k and their first space-derivatives are continuous. We consider an incident electron from the normal region. It can either be normally reflected if the interface is not perfect, or Andreev-reflected as a hole resulting in a Cooper pair transfer into the superconductor. In the normal region the electron and the hole wave functions are written in terms of spinor functions $\begin{bmatrix} 1 \\ 0 \end{bmatrix} e^{ikx}$ and $\begin{bmatrix} 0 \\ 1 \end{bmatrix} e^{ikx}$. They consists of the incident electron, normally reflected electron and Andreev-reflected hole parts:

$$\psi_N = \begin{bmatrix} 1 \\ 0 \end{bmatrix} e^{ikx} + \alpha' \begin{bmatrix} 1 \\ 0 \end{bmatrix} e^{-ikx} + \alpha \begin{bmatrix} 0 \\ 1 \end{bmatrix} e^{ikx} \tag{II.21}$$

In the superconducting region the excitations are not simple electrons but electron-like or hole-like quasiparticles called Bogoliubons. The transmitted wave therefore consists of electron-like and hole-like terms:

$$\psi_S = \beta \begin{bmatrix} u_0 \\ v_0 \end{bmatrix} e^{i\tilde{k}_e x} + \gamma \begin{bmatrix} v_0 \\ u_0 \end{bmatrix} e^{-i\tilde{k}_h x} \tag{II.22}$$

By matching the wave functions across the interface, $\psi_N = \psi_S$, as well as their first derivatives, and solving for all unknown coefficients, the probability amplitudes for normally-reflected ($A'(E) = \alpha'^* \alpha'$) and Andreev-reflected ($A(E) = \alpha^* \alpha$) particles

can be obtained. In particular, the parametrized Andreev reflection amplitude is obtained as

$$A(E) = \frac{|\eta|^2}{|1 + Z^2(1-\eta^2)|^2}. \tag{II.23}$$

Here Z represents the effective barrier height of the S-N interface given in terms of Fermi velocity mismatch in the two regions and $\eta = v_0/u_0$ [110]. Fig. II.10b shows the Andreev reflection amplitude as a function of the effective barrier height. If the interface is perfectly transparent, the Andreev reflection process has a probability of one for energies below the gap. Andreev reflection probability decreases with increasing barrier height, therefore increasing the normal reflection probability. Outside the gap $A(E)$ rapidly decreases, as expected.

2.2 Subharmonic gap structure: Multiple Andreev Reflections

Until now the transport properties of a single S-N interface were discussed in the framework of Andreev reflection. In this section the transport through SNS junctions is explained. In such structures, successive electron and hole Andreev reflections from the two interfaces result in a Cooper pair transport from one superconductor to another. For simplicity we assume perfectly transparent interfaces and ballistic transport through the normal region. A subharmonic gap structure (SGS) in the stability diagram of an SNS junction appears as conductance peaks at finite bias voltages $V_{sd} = 2\Delta/ne, n = 1, 2, 3$,etc. After its first observation by Taylor and Burstein [111], SGS has been experimentally demonstrated in different SNS systems. According to several theoretical studies, the SGS is a result of multiple Andreev reflection (MAR) processes [112, 113, 114]. The schematic representations of these processes are illustrated in Fig. II.11a-c.

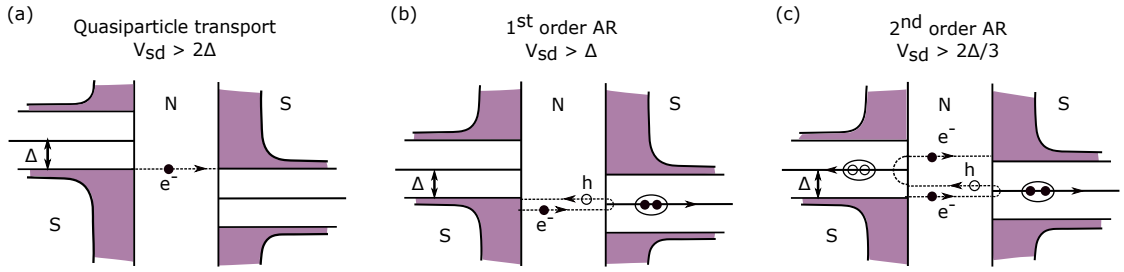


Figure II.11: Multiple Andreev reflection processes: a. Quasiparticle transport for $V_{sd} \geq 2\Delta$, b. First order multiple Andreev reflection for $\Delta/e \leq V_{sd} \leq 2\Delta/e$. Quasiparticle undergoes single Andreev reflection resulting in Cooper pair transfer. c. Second order MAR for $2\Delta/3e \leq V_{sd} \leq \Delta/e$, where Cooper pair transport occurs due to two successive Andreev reflections of quasiparticles.

When $V_{sd} \geq 2\Delta$, quasiparticle transport can occur resulting in a step in the current and therefore a peak in the differential conduction (Fig. II.11a). As illustrated in Fig. II.11b, at $V_{sd} = \Delta/e$ the electron from the left lead is Andreev reflected at the right interface. The resulting hole will eventually occupy the empty state in the left lead only if $V_{sd} \geq \Delta/e$. Thus a quasiparticle from the first lead effectively becomes a Cooper pair in the second. This process is called first order Andreev reflection and appears as a conductance peak at $2\Delta/e$. Note that here the order of the MAR is defined as the number of Andreev reflections from the two interfaces and n-th order MAR results in a conductance peak at $2\Delta/(n+1)e$.

Fig. II.11c shows the second order MAR for $V_{sd} \geq 2\Delta/3e$, where transport happens as a result of two successive Andreev reflections from the two interfaces. The contribution of this process is a Cooper pair as well a quasiparticle transfer and it appears for voltages $2\Delta/3e \leq V_{sd} \leq \Delta$. In general, n-th order MAR is a cascade of n Andreev reflections in which they cross the interface until one finds an empty space in one of the electrodes. The even-ordered MAR result in electron transport, whereas the odd-ordered MAR result in a hole-transport. The contribution of nth order MAR is proportional to t^n, where t is the transmission coefficient of the channel and the conductance through that channel is $G = 2e^2t/h$. Therefore for

non-ideal interfaces, higher order MAR peaks will have lower amplitudes. More generally, because the Andreev reflection probability is strongly suppressed for low interface transparencies, the MAR processes are more likely to be observed for strongly coupled nanotube-lead systems.

2.3 Andreev Bound States

The concept of Andreev bound states (ABS) can be understood in the simple case of a short channel between superconducting electrodes. When no bias voltage is applied, the electrons and holes are multiply Andreev reflected from the interfaces. The constructive interference between the reflected wave-functions can result in bound states forming in the channel. The system acts similar to a Fabry-Pérot interferometer for electrons. The Andreev state wave functions are localized in the vicinity of the contact over a distance of the order of the superconducting coherence length. The number of Andreev bound levels is limited to one pair of levels per conducting electronic mode. To characterize ABS, first assume that the channel has a perfect transmission probability, $\tau = 1$. As shown in Fig. II.12a (solid lines) a right moving electron is Andreev reflected at the right interface acquiring a phase shift corresponding to the phase of the right superconducting order parameter. The Andreev reflected hole is then Andreev reflected at the left interface acquiring a phase shift corresponding to the phase of the left superconducting order parameter. The interference between the reflected wave-functions is constructive when the phase shift acquired in a cycle is an integer multiple of 2π. Similarly, one can start a cycle with a left moving electron. These two cycles therefore result in two Andreev states with energies

$$E_{\rightleftarrows}(\delta) = \mp\Delta cos(\frac{\delta}{2}) sgn[sin(\frac{\delta}{2})], \tag{II.24}$$

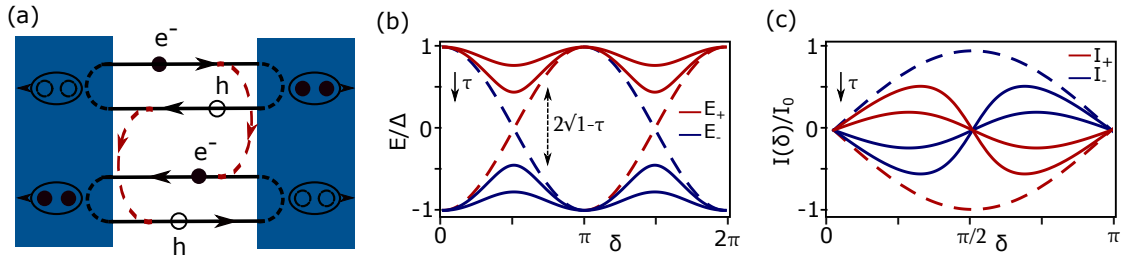


Figure II.12: a. Formation of Andreev bound states in a superconductor-conduction channel-superconductor system. When the interfaces are ideally transparent the particles can only be Andreev reflected (black lines) forming two isolated ABS. Otherwise, also normal reflection happens which mixes the two bound states (red lines). b. Andreev bound state energies given by Eqn. II.25 for $\tau = 1$ (dashed lines) and $\tau < 1$ (solid lines). For $\tau < 1$, degeneracy at $E = 0$ is lifted. c. Supercurrent through the channel carried by the two ABS for for $\tau = 1$ (dashed lines) and $\tau < 1$ (solid lines).

where $\delta = \Phi_L - \Phi_R$ is the superconducting phase difference across the channel. The arrows correspond to the direction of the current carried by the transferred Cooper pairs. The 2π-periodic energies of ABS are plotted with dashed lines in Fig.II.12b, cross at $\delta = \pi$.

If $\tau < 1$, the electrons and holes can also be normally reflected. This couples the two ballistic Andreev bound states, and results in lifted degeneracy and opening of a gap at $\delta = \pi$. The ABS energies in this case are given by*

$$E_{\pm} = \pm\Delta\sqrt{1 - \tau sin^2(\frac{\delta}{2})}. \tag{II.25}$$

As τ is decreased the gap at $\delta = \pi$ is increased (solid lines in Fig. II.12b).

The two ABS are lying within the gap, detached from the continuum, and are symmetric with respect to the Fermi level. One can write the following expression for the density of states of the continuum ($|E/\Delta| \geq 1$):

$$n(E)/n_F = \frac{1}{2}\left|\frac{E}{\Delta}\right|\sqrt{(\frac{E}{|\Delta|})^2 - 1}\frac{1 - \sqrt{1-\tau}}{(E/|\Delta|)^2 - 1 + \tau sin^2(\delta/2)} \tag{II.26}$$

Andreev bound states transfer non-dissipative current (supercurrent) through the SNS structure. The currents carried by the two states are given by the first

* See detailed derivation in [115].

phase-derivatives of ABS energies.

$$I_{\pm} = \frac{1}{\phi_0}\frac{dE_{\pm}}{d\delta} = \mp\frac{e|\Delta|}{2\hbar}\frac{\tau sin(\delta)}{\sqrt{1-\tau sin^2(\delta/2)}} \tag{II.27}$$

The current is plotted in Fig. II.12c for the same values of τ in b. Note that since the conductance channels are independent, in multichannel case, the overall supercurrent can be calculated by adding up the contribution of each channel τ_i.

2.4 Experimental studies of superconductor-contacted carbon nanotubes

In this section a brief review of various experiments on superconductor-contacted nanotubes is presented. As discussed previously, the dominant phenomenon observed in S-N-S systems is the transport due to Andreev reflections and the formation of the Andreev bound states. Many reports addressed the interplay of Andreev reflection and the supercurrent through the nanotube with other quantum transport phenomena, such as Fabry-Pérot interference [33, 116], Kondo effect [31, 32, 34, 50] and Coulomb blockade [117, 118, 119, 120].

In particular, one of these studies shows a transistor behaviour of the supercurrent in a nanotube device in the Fabry-Pérot regime [33]. The authors have found that the maximum value of the supercurrent is strongly correlated with the normal state conductance. In particular, the modulation of the critical supercurrent is due to tuning the quantum states in the nanotube on- and off-resonance with the Fermi level of the leads. Another study of a superconductor-contacted nanotube device in the Fabry-Pérot regime is reported in [116], where a subharmonic gap structure due to Andreev reflections and a zero-bias peak due to a proximity-induced supercurrent transport was observed.

Other studies discuss the interplay between the Kondo regime and superconductivity. It was shown that the interplay between the two can be quantified by the ratio

between the Kondo temperature and the superconducting gap energy [31, 32, 50]. In particular, the supercurrent can coexist with the Kondo resonance when $k_B T_K > \Delta$, where T_K is the Kondo temperature and Δ is the superconducting gap energy. Another study showed that the sub-gap structure resulting from multiple Andreev reflections strongly depends on the spin-state of the quantum dot [34]. In particular, the conductance peak due to the 1st order Andreev reflection is enhanced in the odd-spin state of the nanotube quantum dot.

In low transparency regimes, the competition between the superconductivity and the single particle transport was studied [117, 118, 119, 120]. In this case, interesting transport phenomena, such as π-junction behaviour can be observed, when the supercurrent sign is reversed. In particular, a recent study showed such behaviour in a nanotube quantum dot [118]. When the Kondo effect is strong compared to the proximity effect, both effects coexist and a Kondo-enhanced 0-junction is observed. In the opposite case, the system shows different types of π-junction behaviour, depending on the number of levels involved in the transport.

The first observation of Andreev bound states in nanotubes has been reported in [35]. The local tunneling spectroscopy measurements revealed that these states form from the discrete energy levels of the nanotube and thus contain detailed information about the energies of these states. Nonlocal tunneling spectroscopy measurement of Andreev bound states has been reported in [45], where a second quantum dot is used to probe the sub-gap energies in a superconductor-quantum dot system.

3 Superconducting Microwave Resonators for Circuit QED

As discussed in the introduction of this thesis, in circuit QED the role of the cavity is played by an electrical circuit carrying a microwave field. Despite the

fact that such circuits, otherwise referred to as microwave resonators, have been used since 1960s, interest in these has especially grown in the last two decades. This has been triggered by the demonstration of using high quality microwave resonators as photon detectors [121] and the subsequent usage of these resonators in superconducting quantum circuits [2].

Microwave resonators may either be a lumped-element circuit, such as parallel meandered inductor and an interdigitated capacitor [122], or a transmission-line (distributed element), such as coplanar waveguide resonators [123].

In the planar cQED architecture presented in this work, the objective is to couple a carbon nanotube superconducting quantum interference device to a microwave resonator. As discussed in detail in Section II.4.2, inductive coupling mechanism of the microwave resonator to a potential nanotube flux qubit is chosen. In this case the SQUID-resonator coupling strength is directly proportional to the mutual inductance between them [124]. Unlike distributed-element resonator geometries, large inductance per unit length can be achieved in lumped-element resonators. Therefore, by using lumped-element resonators, one can ensure strong coupling and at the same time keep the SQUID dimensions to the minimal. This results in less magnetic noise through the SQUID, which in general increases with the SQUID loop self-inductance.

In the next section we introduce the theory of the basic LCR circuit. Following this, the transmission matrix model of a capacitively coupled lumped LC resonator is discussed. This model is used to interpret the data presented in Chapter V.

3.1 Basic Theory of Parallel LCR Circuits

Lumped element resonators discussed in this thesis can be modeled as parallel circuits of inductance L, capacitance C and resistance R (Fig. II.13a). The resistance

represents the internal losses in the circuit. The impedance of this circuit is given by

$$Z_{LCR} = (\frac{1}{R} - i\frac{1}{\omega L} + i\omega C)^{-1}. \tag{II.28}$$

An important characteristic of a resonator is its quality factor, which is related to the lifetime of the photons before they escape. Generally, it is defined as the average energy stored in the resonator divided by the energy loss per cycle. In particular, for a parallel LCR circuit it can be written as

$$Q_i = \omega_0 \frac{W_e + W_m}{P_{loss}}, \tag{II.29}$$

where $W_e = 1/4|V|^2C$ and $W_m = 1/4|I_L|^2L$ are the electric and magnetic components of the stored energy and $P_{loss} = 1/2|V|^2/R$ is the power dissipated by the resistor. The resonance condition occurs when $W_e = W_m$, which results in a resonance frequency of $\omega_0 = 1/\sqrt{LC}$. One can then obtain a simple equation for the quality factor: $Q_i = \omega_0 RC$. This is otherwise referred to as the internal quality factor and as mentioned above it describes the photon loss due to internal dissipation.

3.2 Transmission Model for Capacitively Coupled LC Resonator

In our experiments, the LC resonators are studied by capacitively coupling them to a transmission line (Fig. II.13a). The equivalent circuit of the experimental configuration is illustrated in Fig. II.13b. It consists of the parallel LCR resonator which is coupled to a transmission line via a capacitance C_k. The transmission line is designed to be a coplanar waveguide with a characteristic impedance $Z_0 = 50\,\Omega$hm. Dielectric loss is modeled by a resistor R shunting the lumped capacitor C. The circuit includes complex impedances $\Delta Z_{1,2}$ on either side of the resonator, which

can originate for example from coupling the on-chip resonator to the external circuit board via bondwires.

Generally, two-port networks are characterized by the transmission or ABCD matrix, defined in terms of input and output voltages and currents [122]. In a cascade connection of multiple two-port networks, the ABCD matrix is simply the product of the ABCD matrices of the components. It is defined as

$$\begin{bmatrix} V_{in} \\ I_{in} \end{bmatrix} = \begin{bmatrix} A & B \\ C & D \end{bmatrix} \begin{bmatrix} V_{out} \\ I_{out} \end{bmatrix} \tag{II.30}$$

The transmission through the circuit that we are interested in is then given by [122]

$$S_{21} = \frac{2}{A + B/Z_0 + CZ_0 + D}. \tag{II.31}$$

In particular, for the bare LCR resonator these equations become

$$\begin{bmatrix} A & B \\ C & D \end{bmatrix} = \begin{bmatrix} 1 & Z_{LCR} \\ 0 & 1 \end{bmatrix}, \quad S_{21} = \frac{2}{2 + Z_{LCR}/Z_0}. \tag{II.32}$$

For the capacitively coupled LCR resonator, similar calculations result in a transmission coefficient given by [6, 125]

$$\begin{aligned} S_{21} &= \frac{2Z_0}{Z_1 + Z_2} \frac{1}{1 + Z/Z_R} \\ 1/Z &= 1/Z_1 + 1/Z_2, \end{aligned} \tag{II.33}$$

where $Z_1 = Z_0 + \Delta Z_1$ and $Z_2 = Z_0 + \Delta Z_2$. Z_R is the impedance of the resonator in series with the coupling capacitance C_k. In this system an additional dissipation channel exists via the load resistance. This results in a further reduction of the quality factor, which is represented by the external quality factor Q_e. One can define a loaded quality factor for the complete circuit as

$$\frac{1}{Q_l} = \frac{1}{Q_i} + \frac{1}{Q_e}. \tag{II.34}$$

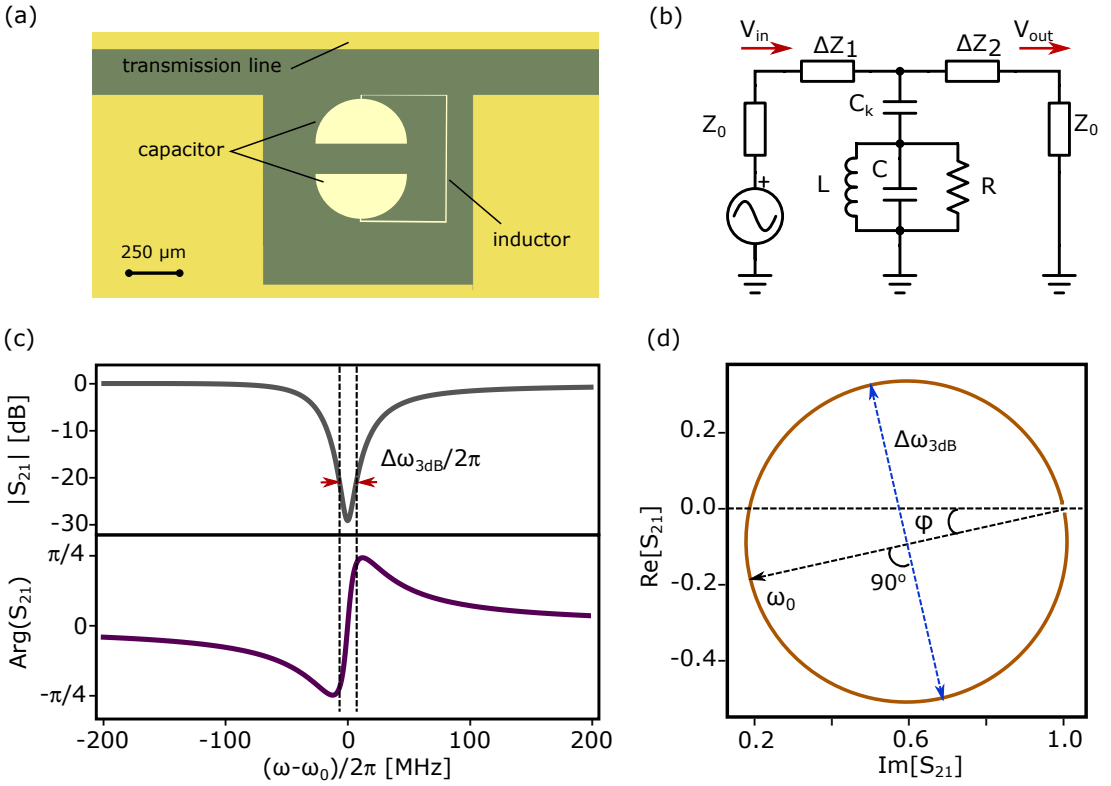


Figure II.13: a. A digital microscope picture of an LC resonator discussed in Chapter V showing the capacitor pads connected with an inductor line. The resonator is capacitively coupled to a transmission line. It is surrounded with ground planes. b. The circuit diagram of an LCR resonator coupled to a transmission line through a capacitance C_k. The input and output ports have $Z_0 = 50\,\text{Ohm}$ impedances. $\Delta Z_{1,2}$ are the impedances due to coupling the on-chip resonator to an external circuitry via the bond wires. c. The amplitude and the phase of the resonance obtained using Eq. II.36 for the following values of the resonator parameters: $Q_i = 1000, Q_e^* = 200, \phi = 11.5^o, \omega_0 = 2\pi \times 10$ GHz. d. The complex plane representation of the transmission showing the impedance mismatch angle ϕ.

Near the resonance frequency ω_0, the impedance of the resonator in series with the coupling capacitance is given by [126],

$$Z_R = \frac{Z_0 Q_e}{2Q_i}(1 + i2Q_i\delta\omega), \tag{II.35}$$

where $\delta\omega = (\omega - \omega_0)/\omega_0$. The resonance frequency ω_0 now depends also on the coupling capacitance C_k. The pre-factor in Eqn. II.33 depends on the physical structure of the chip and the external circuit board and therefore it is nearly frequency independent. Moreover, because of the impedances $\Delta Z_{1,2}$

being small it is nearly unity. This pre-factor can be included in the calibration of the off-resonance transmission through the measurement cables, resulting in a normalized transmission,

$$S_{21}^{-1} = 1 + \frac{Z}{2Z_R} = 1 + \frac{|Z|e^{i\phi}}{2Z_0Q_e/2Q_i(1+i2Q_i\delta\omega)} = 1 + \frac{Q_i}{Q_e^*}e^{i\phi}\frac{1}{1+i2Q_i\delta\omega} \quad \text{(II.36)}$$

Here, we introduced the rescaled external quality factor $Q_e^* = (Z_0/Z)Q_e$, which depends on the magnitude of Z. The obtained form of the transmission will be used when analyzing the data in the following chapters.

Fig. II.13b shows the amplitude and the phase of the resonance given by Eq. II.36. The quality factor of the resonance is proportional to the full width at half maximum (FWHM) of the resonance. The latter corresponds to the width at 3 dB from the minimum when plotted in a logarithmic scale. One can notice the slight asymmetry of the resonance with respect to the base line. This is a direct result of the impedance mismatch in the circuit given by $\Delta Z_{1,2}$ (or otherwise the mismatch angle ϕ). The representation of the resonance in the complex plane is plotted in Fig. II.13c, where it appears as a circle rotated with respect to $y = 0$ axis by angle ϕ. The resonance frequency as well as the frequencies corresponding to FWHM of the resonance are shown with arrows.

3.3 Inductance of the Lumped Resonator

In order to achieve the required resonator frequencies, theoretical estimations for the inductances of the lumped inductor are used in our experiments. We represent the energy in the superconductor via the electrical current carried by particles with mass m and number density n. For a homogeneous conductor of uniform cross section A, length l and current density J_s, the energy is given by [127, 128],

$$E = \int_s \frac{1}{2}\mu_0 H^2 ds + \int_s \mu_0\lambda^2 J_s^2 ds = \frac{1}{2}L_M I^2 + \frac{1}{2}\mu_0\lambda^2\frac{l}{A}I^2. \quad \text{(II.37)}$$

The factor L_m in the first term, referred to as magnetic inductance, is associated with the magnetic field energy density within the superconducting volume created by J_s. The prefactor of the second term, $L_k = \mu_0\lambda^2 l/A$, is called kinetic inductance and is associated with the kinetic energy of Cooper pairs. λ is the penetration depth of the superconductor. The total inductance of the lumped inductor is given by the sum of magnetic and kinetic inductances, $L = L_m + L_k$.

The magnetic inductance is purely geometry-dependent and is well-approximated by the following expression for a microstrip with dimensions l, w, t [129],

$$L_m = 2l(Log\frac{2l}{w+t} + 0.5 + 0.2235\frac{w+t}{l}) \cdot 10^{-7}[H]. \tag{II.38}$$

To further expand the equation for the kinetic inductance we write the penetration depth in terms of the superconducting coherence length ξ_0 and film thickness t (valid for thin films):

$$\lambda \approx \frac{4}{3}\lambda_L\sqrt{\frac{\xi_0}{t}}, \quad \xi_0 = \frac{\hbar v_F}{\pi\Delta(0)} \tag{II.39}$$

where $\lambda_L = \sqrt{m/\mu_0 n_s e^2}$ is the London penetration depth [130]. Note that the coherence length is assumed to be temperature independent *. In Eqn. II.39, v_F is the Fermi velocity and $\Delta(0) = 1.764 k_B T_c$ is the superconducting energy gap at zero temperature, given by the critical temperature T_c.

3.4 Temperature Dependence of the Quality Factor

According to the two-fluid model used to describe superconductivity before the BCS theory, two conduction channels of Cooper pairs (n_s) and thermally excited quasiparticles (n_n) coexist independently [130, 131]. At high frequencies, the dissipations in these channels are due to the existance of normal quasiparticles

*This is an approximation of the BCS theory, referred as the Pippard model [130].

and the kinetic inductance of Cooper pairs. The resistance for a superconductor of length l and cross-sectional area A can be written as

$$R = \sigma_n L_k^2 \frac{A}{l} \omega^2. \tag{II.40}$$

Here $\sigma_n = n_n \tau_n e^2/m$ is the conductivity of the normal quasiparticle channel with relaxation time τ_n. Using the equation for the kinetic inductance introduced in the previous section, we obtain

$$R = \frac{n_n}{n_s} \tau_n \lambda^2 \omega^2 \mu_0 \frac{l}{A}. \tag{II.41}$$

The temperature dependence of the resistance can be obtained by taking into account the following equations introduced in the two-fluid model and the BCS theory: [132, 133]

$$n_n/n_s = exp(-1.764 T_c/T), \quad \lambda(T) = \frac{\lambda(0)}{\sqrt{1-(T/T_c)^4}}. \tag{II.42}$$

One can thus write the temperature dependence of the kinetic inductance and therefore the resonance frequency as

$$L_k(T) = \mu_0 \frac{\lambda(0)^2}{1-(T/T_c)^4} \frac{l}{A}, \quad \omega_0(T) = \frac{1}{\sqrt{(C(L_m + L_k(T)))}} \tag{II.43}$$

Finally, for the temperature dependence of internal quality factor of the resonator we obtain

$$Q_i(T) = \frac{\omega_0 L}{R} = \frac{L_m + L_k(T)}{\tau_n \omega_0(T) L_k(T)} exp(1.764 T_c/T). \tag{II.44}$$

3.5 Quantization of the LCR Resonator

Until now we have described the properties of LCR resonators using a classical model. Such treatment is useful when designing and measuring unloaded resonator properties, such as resonance frequenciy and quality factors, and their power and

temperature dependences. On the other hand, when incorporating these systems in quantum circuits for cQED experiments, their full quantum-mechanical description is necessary. To derive the Hamiltonian of the quantized LC resonator, we consider a parallel lossless resonator with inductance L and capacitance C. The energy stored in these components is given by,

$$\begin{aligned} E &= \frac{1}{2}LI^2 + \frac{1}{2}CV^2, \\ V &= \frac{Q_c}{C} = -L\frac{\partial I}{\partial t} \end{aligned} \tag{II.45}$$

where I is the current through the inductor and V is the voltage drop across the capacitor. Taking into account the equation for the flux through the inductor, $\Phi = LI$, we rewrite this equation as

$$E = \frac{\Phi^2}{2L} + \frac{Q_c^2}{2C}. \tag{II.46}$$

One can replace the charge and the flux by corresponding operators to obtain the Hamiltonian,

$$\hat{H} = \frac{\hat{\Phi}^2}{2L} + \frac{\hat{Q_c}^2}{2C}. \tag{II.47}$$

Using Eqs. II.45 and II.47, we can write

$$\frac{\partial \hat{H}}{\partial \Phi} = \frac{1}{L}\hat{\Phi} = \dot{\hat{Q}}_c, \quad \frac{\partial \hat{H}}{\partial Q_c} = \frac{1}{C}\hat{Q}_c = -\dot{\hat{\Phi}} \tag{II.48}$$

The equations above indicate that Φ and Q_c can be thought of as the generalized position and momentum operators of the system, in analogy to the mechanical oscillator, obeying the canonical commutation relation $[\hat{\Psi}, \hat{Q_c}] = -i\hbar^*$. Therefore, similar to the mechanical oscillator, the Hamiltonian in Eqn. II.47, can be

*For a mechanical oscillator with mass m, momentum p and resonance frequency ω_r, the Hamiltonian is given by $\hat{H} = \hat{p}^2/2m + m\omega^2\hat{x}^2/2$.

diagonalized by introducing the photon creation and annihilation operators,

$$\begin{aligned}\hat{a}^{+} &= \frac{1}{\sqrt{2\hbar\sqrt{L/C}}}(\sqrt{L/C}\hat{Q}_c - i\hat{\Phi}),\\ \hat{a} &= \frac{1}{\sqrt{2\hbar\sqrt{L/C}}}(\sqrt{L/C}\hat{Q}_c + i\hat{\Phi})\end{aligned} \tag{II.49}$$

The Hamiltonian can we rewritten as

$$H = \hbar\omega(\hat{a}^{+}\hat{a} + \frac{1}{2}), \tag{II.50}$$

where $\omega^2 = 1/LC$ is the resonance frequency.

Using Eqn. II.49, the circuit operators can be explicitly written in terms of the annihilation and creation operators,

$$\begin{aligned}\hat{\Psi} &= (1/\hbar\sqrt{L/C})^{1/2}(\hat{a} - \hat{a}^{+})\\ \hat{Q}_c &= (1/\hbar\sqrt{L/C})^{-1/2}(\hat{a} + \hat{a}^{+})\end{aligned} \tag{II.51}$$

The quantum-mechanical description of a resonator is valid when the dissipation is negligible. This can be achieved, for example, by fabricating the resonator from a superconducting material and measuring it at very low temperatures ($T \ll T_c$).

4 CNT-SQUID Resonator Coupling

If we are to consider the Andreev bound states in a superconducting contacted carbon nanotube as a qubit for potential use in quantum computing, or if we simply wish to study such states in a quantum coherent fashion, then we must find a way to effectively isolate the device from its electrical environment (to suppress decoherence) whilst maintaining the capability to control and measure it. This capability is provided by cavity or circuit QED, in which a qubit is embedded in a resonator, which both protects the qubit from its electrical environment, and provides a quantum non-demolition (QND) measurement of the qubit (via qubit state-dependent resonator frequency shifts).

Theoretical studies have been carried out into the potential for realizing an Andreev bound state version of circuit QED [27, 134]. In the following, we discuss in detail the embedding of a nanotube in a SQUID loop, and inductively coupling this to a microwave resonator.

4.1 Carbon Nanotube RF SQUID

The superconducting quantum interference device combines two quantum properties of the superconductivity: tunneling of Cooper pairs through a normal weak link connected to superconductors, and flux quantization in a superconducting loop. An RF SQUID consists of a single weak link integrated into a superconducting loop. It is subjected to magnetic flux ϕ_{ext} generated by an external magnetic field perpendicular to the loop, which periodically modulates the Josephson current through the link. In particular, the phase across the junction can be directly linked to the flux threading the loop, $\delta\phi = 2\pi\Phi_{ext}/\Phi_0$, where $\Phi_0 = h/2e$ is the flux quantum. For carbon nanotube junctions, a capacitively coupled elecrostatic gate can be used together with the flux as a second degree of freedom of the SQUID system.

As previously discussed, the Josephson current or the supercurrent in nanotube junctions is carried by Andreev bound states with energies given by Eqn. II.25. One can introduce a Hamiltonian that describes the dynamics of ABS in a SQUID device (Fig. II.14a). We restrict ourselves to the simple case of a single conduction channel junction carrying two Andreev states. The transition frequency between the two states is given by,

$$\begin{aligned} \nu_{ABS}(\delta) &= \frac{E_+ - E_-}{h} = \frac{2\Delta}{h}\sqrt{1 - \tau sin^2(\delta/2)}, \\ \nu_{ABS}^{min} &= \frac{2\Delta}{h}\sqrt{1-\tau} \end{aligned} \tag{II.52}$$

Fig. II.14b shows ν_{ABS}^{min} as a function of the phase across the junction for different transmission probabilities. When τ increases, the minimum transition frequency

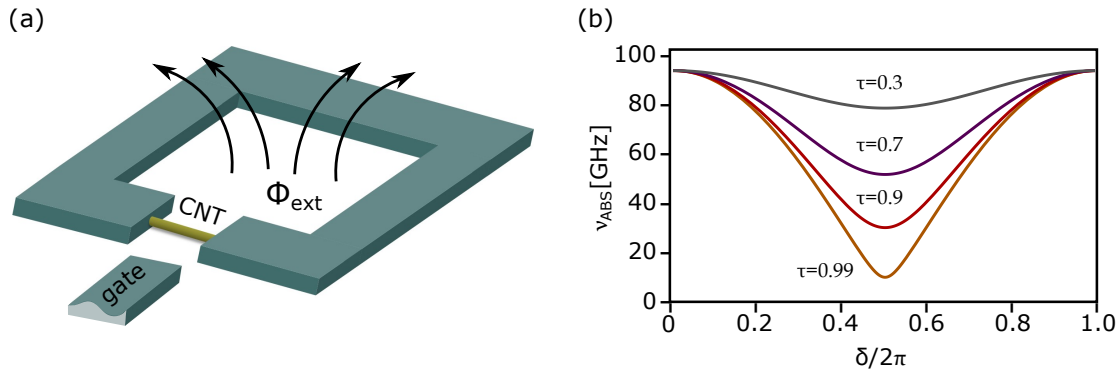


Figure II.14: a. Schematic picture of a carbon nanotube RF SQUID, where a nanotube is embedded in a superconducting loop. An external flux threading the loop tunes the phase across the nanotube. A side-gate can be used to tune the quantum levels in the nanotube. b. The Andreev level transition frequency as a function of the phase across the nanotube for different transmission probabilities.

decreases. Taking into account Eqn.II.52, the Hamiltonian in the eigen-basis of Andreev levels $\{|+\rangle, |-\rangle\}$ can be obtained as [135]

$$\hat{H}_{ABS} = \begin{bmatrix} E_+ & 0 \\ 0 & E_- \end{bmatrix} = \frac{h\nu_{ABS}(\delta)}{2}\hat{\sigma}^z, \tag{II.53}$$

where σ^z is the Pauli matrix. The physics of the ABS system therefore resembles that of a spin-1/2 in a magnetic field.

For large transmission probabilities, Andreev levels lay deep in the superconducting gap, well detached from the quasiparticle continuum. In this case, coherent coupling of the Andreev levels to the supercurrent flowing through the junction makes the Andreev levels accessible for manipulations and for measurements. Therefore, one can think of a new type of a superconducting qubit, where the switching between the two persistent current states is due to the true microscopic system formed by the two-level Andreev bound states embedded in a SQUID. The readout of this qubit can be achieved by measuring the macroscopic current in the SQUID.

4.2 Inductive Coupling of CNT SQUID to MW Resonator

The motivation of coupling a nanotube SQUID to a resonator is due to the possibility of studying the above described Andreev level qubit in a cQED architecture. Generally, the coupling of a qubit to a microwave resonator can be capacitive (voltage) or inductive (current). For example, in charge or phase qubits both types of couplings have been demonstrated [136, 137, 138]. On the other hand, for superconducting flux qubits typically the inductive coupling is used [124, 134, 139, 140]. This is partially due to the fact that in flux qubits the states are often related to the currents circulating in two directions in the loop. This is true for the Andreev level qubit where the currents in two directions are carried by the two Andreev bound states. In this section we discuss the inductive coupling mechanism of a nanotube SQUID to a microwave resonator for RF probing the quantum states in the nanotube as well as possible cQED measurements of the Andreev level qubit. In this case the SQUID and the resonator share a section of the inductor and they are mutually coupled via the phase difference across that section. The Hamiltonian describing the magnetic-dipole interaction between the 2-level Andreev system and the resonator is given by

$$H_{int} = \hbar g(\hat{a}^\dagger \hat{\sigma}_A^- + \hat{\sigma}_A^\dagger \hat{a}), \tag{II.54}$$

where $\hat{\sigma}^\dagger$ ($\hat{\sigma}^-$) is the creation (annihilation) operator of the two-level system. The coupling constant is given by $g = MI_pI_{r0}$, where M is the mutual inductance, I_p is the persistent current in the SQUID loop and $I_{r0} = \sqrt{h\nu_r/L_r}$ is the zero-point current in the resonator with a total inductance L_r and resonance frequency ν_r [139]. The coupling strength can therefore be increased by increasing the mutual inductance and reducing the total inductance of the resonator. In addition to this, the SQUID loop are should be minimized to reduce the coupling of the external magnetic noise

via the self-inductance of the loop. Taking into account the Hamiltonian and for the harmonic oscillator in Eqn. II.50 and the Hamiltonian of the Andreev levels II.53, the total Hamiltonian for the coupled system can be written as

$$\hat{H} = \frac{h\nu_{ABS}(\delta)}{2}\hat{\sigma}^z + \hbar\omega(\hat{a}^+\hat{a} + \frac{1}{2}) + \hbar g(\hat{a}^\dagger\hat{\sigma}_A^- + \hat{\sigma}_A^\dagger\hat{a}). \tag{II.55}$$

The eigenvalues of this Hamiltonian are the dressed states of the resonator, which are different from the bare resonator states for a non-zero g. These dressed states have energies of $h\nu_r(n+1/2) \pm \nu_A/2$, where n is the photon number in the resonator and $h\nu_A/2$ is the level-separation of the Andreev qubit.

In the classical model, when coupled to the resonator, the state-dependent impedance of the nanotube loads the resonator, resulting in a resonance frequency shift. This therefore allows a readout of the nanotube state. The classical case is further discussed in Chapter VI.

III

Experimental Techniques

Contents

1 Carbon Nanotube Devices 56
1.1 Sample Fabrication 56
1.2 Measurement Setup Description 60
2 Microwave Resonators 64
2.1 Sample Preparation 64
2.2 Measurement Techniques 66
3 Nanotube-Resonator Coupled Devices 67
3.1 Design and Fabrication of Coupled Devices 68
3.2 Measurement Setup 70

In this chapter the fabrication techniques of the measured samples as well as corresponding measurement setups are described. In the first part of the chapter we introduce the experimental methods for preparing and measuring the nanotube samples in DC transport experiments. In the second part, the fabrication techniques and the measurement setup for microwave resonators is presented. Finally, in the third part we introduce the experimental techniques for measuring the samples consisting of nanotubes embedded in microwave circuits.

1 Carbon Nanotube Devices

1.1 Sample Fabrication

1.1.1 Precise Placement and Growth of Nanotubes

Carbon nanotubes used in the experiments have been grown by our collaborator Fei Pei at Kavli Institute of Nanoscience, TU Delft. For this the well established chemical vapor deposition (CVD) method was used with organic iron catalyst. The catalyst recipe has been proven to function well for a decade at the group in TU Delft [141]. The catalyst consists of a mixture of 30 mg Aluminium oxide, 40 mg $Fe(NO_3)_3 \cdot 9H_2O$ and 9 mg $MoO_2(acac)_2$ dissolved in 40 mL methanol. The mixture has been sonicated for one hour.

Scanning electron microscope (SEM) picture of a substrate with carbon nanotubes used in the DC transport experiments is shown in Fig. III.1a and b. The substrate is highly resivitystive silicon ($\rho > 20000$ Ω·cm). High resistivity is necessary reduce the microwave loss when incorporating nanotube devices in microwave circuits.

The precise positioning of nanotubes is implemented by exposing arrays of catalyst sites on a PMMA coated substrate with electron beam lithography (EBL). Few drops of the catalyst mixture are then deposited on the developed substrate. The substrate is subsequently baked at 150°C for 10 minutes and the resist is lifted off leaving the catalyst only at the predefined sites. The substrate is then put in a CVD oven at 900°C with CH_4 and Argon gas for 15 minutes.

Nanotubes grown with this procedure generally have diameters in the 1.5-2.5 nm range, measured with atomic force microscopy (AFM) and lengths of up to 50 μm (Fig. III.1b,c). Based on the nanotube diameters it is believed that they are mostly single- or double-walled [142].

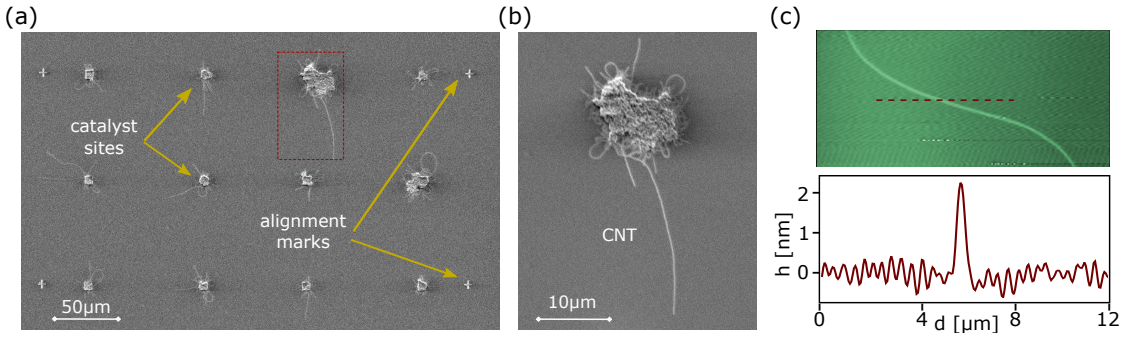


Figure III.1: a. Scanning electron microscope picture of the Si substrate showing carbon nanotubes grown from catalyst sites and substrate alignment crosses. b. A zoomed in picture of the catalyst and the nanotube in the red rectangle in a. The length of the nanotube is approximately 25 μm. c. An AFM picture of a nanotube and its cross-section. The Nanotube height is about 2.2 μm.

In order to precisely locate the nanotubes when imaging the substrate, three sets of Ti/Pt alignment marks were deposited on the substrate before the growth. The material for the marks has been chosen such that they survive high growth temperatures.

1.1.2 Nanotube Imaging and Sample Design

After the growth, nanotube substrates are coated with protective resist and cleaved into 5×5 mm samples. The protective resist layer is subsequently removed by rinsing the samples in acetone and isopropanol.

The first step towards designing nanotube devices is the nanotube imaging. This is done using a scanning electron microscope or atomic force microscope. The advantage of using SEM is that it is considerably faster. However, it can result in contamination of samples by amorphous carbon deposition from the SEM gun. Therefore, the imaging time should be minimized. As shown in Chapter IV, we have found that SEM imaging does not prevent us from obtaining high contact transparencies between nanotubes and metal leads. Nanotubes are located using three sets of alignment marks with variable sizes. The estimated error on the

nanotube location in the sample design is less than 0.5 μm. Autocad is used to design source drain and gate electrodes contacting the nanotubes.

1.1.3 Lithography Techniques

The contacts to the nanotubes are fabricated by successive electron beam lithography and metal electron beam evaporation techniques. Before the EBL the chips are spin-coated with 950 K PMMA resist layer of about 150 nm and baked at 150°C. The substrates are developed at room temperature in a solution of MIBK:IPA (1 : 3). Development opens a window in the PMMA to subsequently be able to deposit contact metal on the nanotubes. Since we are interested in very high transparency contacts, it is of utmost importance that the PMMA is fully removed and that the nanotubes are clean after this stage. We therefore add an additional step before the evaporation, which is the etching of the PMMA traces in the developed areas with a UV light. For this purpose the developed samples are placed in a UV ozone cleaner (ProCleaner Plus, BioForce Nanosciences), where a high intensity mercury vapor lamp generates 254 nm light which cleaves the bonds of organic molecules on the surface. We have found that this enables consistently high transparency contacts to be realized (see Chapter IV), whereas without this step the contact transparencies were low. In particular for SN-metal contacted nanotubes, it has been possible to observe Andreev reflection transport, which require high transparency of the contacts, only when adding the ozone cleaning step. More powerful etching techniques are not used, as they tend to remove the nanotubes as well. For the DC devices with normal metal contacts, 50 nm of Pd is evaporated on the substrate. As discussed in Section 1.1.3, Pd-nanotube interfaces are highly transparent due to the well-matching work-function and wetting properties of Pd. The superconductor-contacted nanotube devices are fabricated using the Pd (4 nm)/Al (80 nm) bilayer.

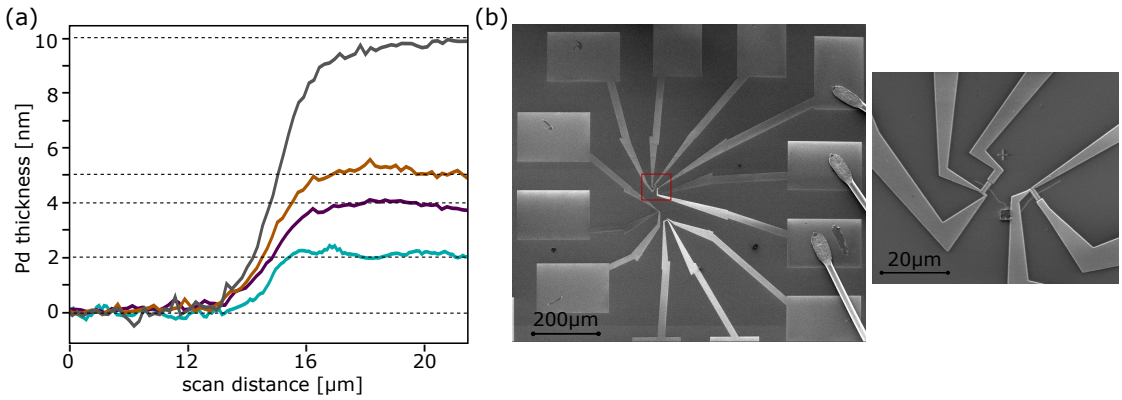


Figure III.2: a. AFM measurements of Pd films with $2, 4, 5, 10$ nm thicknesses evaporated on a Si substrate after thickness calibration. b. SEM image of a sample with four nanotube devices. The right device is bonded with Au wires to the external circuit board. Source and drain leads contact 300 nm sections of separate nanotubes. A gate lead is capacitively coupled to the nanotube. The zoomed-in picture on the right shows the catalyst sites and the contacted nanotubes.

This bilayer is superconducting due to the superconducting proximity effect between the two metallic layers. The thickness of the Pd layer was optimized such that it is thick enough to cover the nanotubes completely. On the other hand, it should be thin enough such that it only weakly affects the superconducting properties of the Al layer (e.g. the bilayer critical temperature is not strongly reduced compared to the critical temperature of Al).

Generally, Pd is deposited at low rates (around 0.25 nm/s) in order to obtain uniform films. As the Pd thickness is a crucial parameter, it is calibrated by evaporating a range of thicknesses on a Si substrate covered with a wire mask in electron-beam evaporator and measuring them on AFM. Fig. III.2a shows AFM measurements of the evaported Pd films of $2, 4, 5, 10$ nm after the calibration. The roughness of the films is less than 0.5 nm for up to 2 nm films. Since the adhesion of the Pd layer to the Si substrate is weak, the Pd/Al bilayer is not suitable for the bond pads. Instead, Ti/Au bond pads are deposited in advance in a separate lithography step. 1 μm diameter Au wires are used to bond the nanotube devices

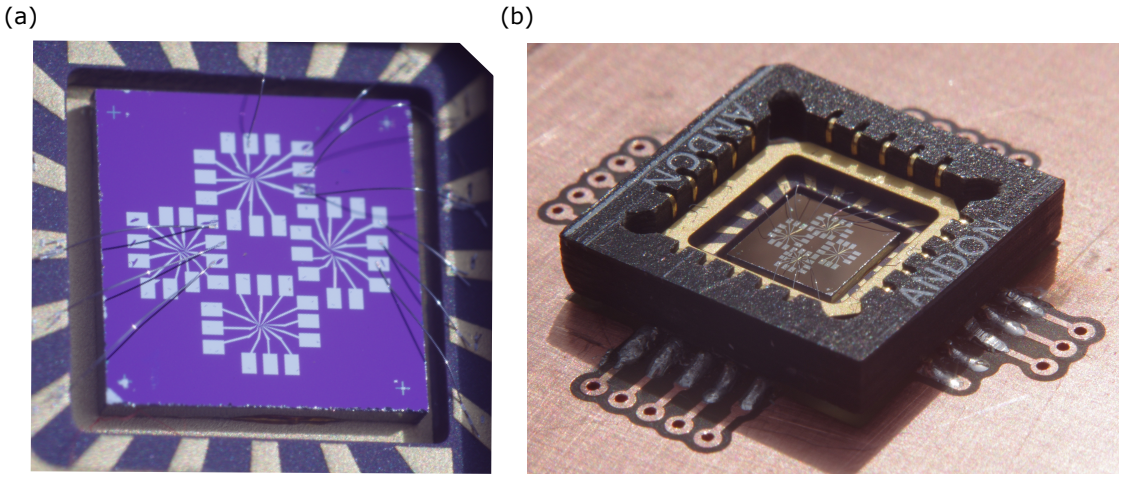


Figure III.3: a. Picture of a nanotube DC sample with nanotube devices. The sample is mounted in a non-magnetic chip-carrier with GE varnish. Au bond wires bond the Au pads on the sample and the chip carrier. b. Picture of the chip carrier containing the sample inserted in a ANDON socket. The socket is mounted on the sample holder circuit board.

to the external circuit board.

SEM picture of a sample with few nanotube devices is shown in III.2b. The length of the contacted nanotube sections is designed to be 300 nm. Its measured values are within 5% of the designed value. The typical scattering length due to intrinsic defects in CVD grown nanotubes is less than 1μm, therefore we choose a smaller contact distance to minimize the effects of scattering [92]. In addition, it has been shown that the transport in Pd contacted 300 nm length nanotubes is nearly ballistic [74]. The distance of the gate electrode from the nanotube is 2.5 μm. Although the gate is partially screened by the source and drain electrodes, we find that it is still effective for tuning the quantum levels in the nanotube (see Section IV1.1).

1.2 Measurement Setup Description

The DC resistance of each contacted nanotube is first measured in a DC probe station, and the lowest resistance devices ($R < 100\,\mathrm{k}\Omega$) are subsequently bonded for low temperature measurement. Low temperature measurements are performed in a

Oxford Triton 200 dilution refrigerator. An accurate measurement of the electron temperature of the devices mounted at the 10 mK stage has been done by measuring Josephson junction qubits in 3D cavities, yielding an electron temperature range of 60-100 mK. Note that this is the stage at which all of the devices throughout this thesis were mounted at.

Nanotube samples are positioned and glued with GE varnish in a non-magnetic chip carrier (Fig. III.3a). The individual devices are then bonded to the gold pads of the chip carrier with Au bond wire in a wedge bonder system. The chip carrier is inserted into a socket mounted on the sample holder printed circuit board (PCB) (Fig. III.3b). A picture of the copper sample holder containing the nanotube sample is shown in Fig. III.4a. The sample holder is attached to the 10 mK plate of the fridge. A cryogenic Microminiature-D connector with sockets is soldered on the PCB*. A second Microminiature-D connector with pins soldered to a loom connects the individual devices to the BNC connectors on a room temperature breakout box. The loom is made of sections of copper and constantan (copper-nickel alloy). The pairs of the loom wires connected to source and drain leads of each device are twisted to cancel out the magnetic noise. The loom is well thermalized between copper plates mounted at each temperature stage of the fridge using a thermally conductive grease. Since nanotube devices are static sensitive, each BNC connector on the breakout box is controlled with a switch that has 'ground' and 'on' states.

Filtering of DC Lines For low noise measurements as well as low electron temperatures in the leads it is crucial to filter the noise on DC lines connected to the nanotube devices. Note that both low frequency (e.g. 50 Hz from power supplies) as well as high frequency (electromagnetic sources outside the fridge) noise needs to be filtered. Firstly, shielded BNC cables are used for connecting the breakout

*25-way Microminiature-D connectors with pins or sockets are obtained from CMR-Direct.

(a) (b)

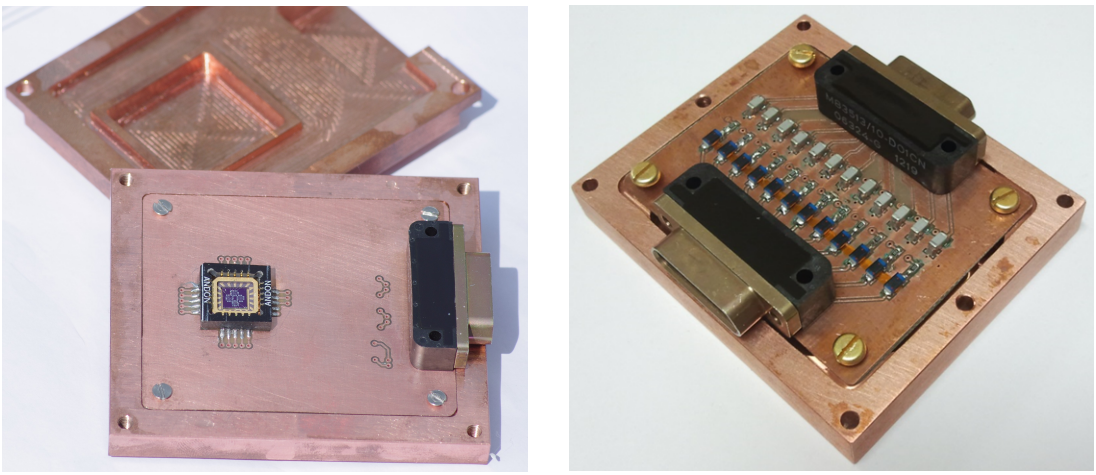


Figure III.4: a. Copper sample holder used for the DC experiments. A D-shaped cryogenic connector is soldered to the DC lines on the PCB. A separate copper cover is used to shield the sample. b. The RLC low-pass filter with 160 Hz cutoff frequency. The filter is inserted in a copper shield. It is mounted at the 10 mK stage of the Fridge and connected to the DC loom via two D-shaped cryogenic connectors.

box to the measurement instruments. The custom built circuit components (such as the current to voltage converter and the voltage divider) are shielded in metallic cases. The high frequency noise is reduced using 10 MHz cutoff frequency Pi-filters attached to each BNC connector in the breakout box. The low frequency noise is filtered out with a low temperature LRC filter with a cutoff at 160 Hz (Fig. III.4b), which is mounted at the 10 mK stage.

Lock-In Techniques DC measurements are performed using standard lock-in techniques, where the differential conductance (resistance) of the nanotube is measured as a function of the bias and gate voltages. A schematic diagram of the measurement setup is illustrated in Fig. III.5. The instruments are controlled by a computer via a GPIB interface. A small amplitude sinusoidal excitation from the Lock-in amplifier internal waveform generator is combined with a DC voltage from SIM928 voltage source and divided 1000 times using a home-built potential divider to obtain low amplitudes of the sinusoidal excitation. By replacing the divider with

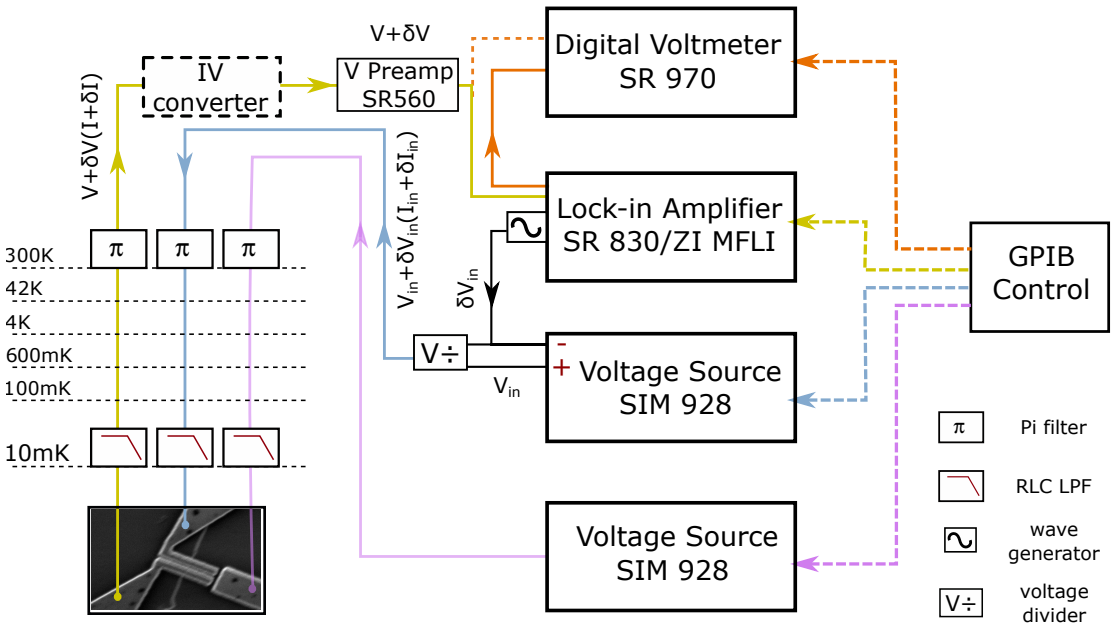


Figure III.5: Diagram of the measurement setup. The sample is attached to the 10 mK stage of the dilution refrigerator. The input and output lines are filtered with 10 mK RLC and room temperature Pi-filters. Output DC voltage from SIM928 source is combined with a sine-wave ac voltage (generated by the internal wave-generator of the Lock-in) and applied to the input of the device. The output signal from the device is measured with a Lock-in amplifier and a digital voltmeter. A low-noise currect-to-voltage converter is used on the output line in voltage-biased measurements. Instruments are controlled via a GPIB interface by a computer.

a 10 MΩ resistor, which is much larger than the nanotube resistances, the nanotube becomes effectively current biased*. The input and output lines are attached to 10 mK LRC low pass filters (LPF) and room temperature Pi-filters. In voltage-biased measurements, a current to voltage converter is attached to the output BNC cables. A SRS560 voltage preamplifier is used to amplify and additionally filter the output signal from the device before measuring it with the Lock in amplifier. The component of the output signal ∂I (δV) at the input sine wave frequency is then measured with the Lock-in amplifier and SIM970 digital voltmeter. The differential conductance (resistance) is then given by $\partial I/\partial V_{in}$ ($\partial V/\partial I_{in}$), where ∂V_{in} (∂I_{in}) is the amplitude of the input sine wave. Simultaneously the DC component of the received signal is

*In this case it is also necessary to remove the current to voltage converter.

measured using a separate channel of the digital voltmeter. The frequency of the excitation is chosen to be much smaller than the cutoff frequencies of the filters to avoid the signal reduction. Note that when doing low noise measurements, one should pay attention to some of the important parameters on the lock-in amplifier, such as the sensitivity and time constant. In the measurements the time constant was chosen large enough to avoid artificial signal cutoffs, especially when measuring fine transport characteristics. The signal averaging time was chosen to be 3-5 times larger than the Lock-in time constant. The sensitivity was tuned depending on the input voltage. The amplitude of the output sine wave is chosen according to the desirable resolution of the measurement (typically changing between $1 - 100\,\mathrm{mV}$).

In order to perform magnetic field dependent measurements a superconducting magnet is used, above which the sample holder is fixed. The magnet was built by the Cryomagnetics group at the Physics Department, University of Oxford. It consists of a copper housing, onto which superconducting wire is wound. The magnet was calibrated using a magnetic sample from Alexy Karenowska's group at the Physics Department with well-known magnetic properties. The relation between the current and the induced field was found to be about $0.079\,\mathrm{T/A}$.

2 Microwave Resonators

In this section we briefly describe the preparation and measurement technique for the microwave resonators.

2.1 Sample Preparation

Two types of samples of microwave resonators have been fabricated and measured. The first type of samples consist of a single LC resonator on a highly resistive Si substrate (Fig. III.6a). The high resistivity of the substrate reduces the microwave

loss therefore increasing the internal quality factor of the resonators. The resonator capacitor C consists of semicircular pads within a small distance from each other*. They are connected with a meander inductor L. The resonator is coupled to input and output microstrip lines, which are designed to have 50 Ω impedances. The resonance frequency can be tuned by changing the size and distance of capacitor pads as well as the length of the inductor.

In the second type of samples, multiple LC resonators are fabricated on the same substrate, coupled to a coplanar transmission line (Fig. III.6b). The inductor in this case is a straight line and is designed to have much lower inductance compared to the first type of samples. This is necessary for having a large coupling strength for smaller nanotube SQUID sizes when coupling the resonators to nanotube SQUIDs. The resonators are surrounded by ground planes to electromagnetically isolate them from each other. The resonance frequencies are tuned by changing the diameters of the capacitor plates and keeping all other dimensions constant.

The fabrication of the above described samples consists of the following steps. First, Ti/Au ground planes and coplanar transmission line are deposited on 20×20 mm Si wafers which is rinsed beforehand in acetone and isopropanol. This is achieved in successive photo lithography and electron-beam evaporation steps. The wafer is then covered with a protective photoresist layer and cleaved into 10×5 mm chips with a diamond cleaver. After cleaning the chips in 50°C acetone and rinsing in IPA, resonator designs are patterned using EBL and Al, Ti/Al or Pd/Al metal bilayers are evaporated. The first two bilayers are used for general testing of the resonators, whereas Pd/Al is used for the purpose of later integrating resonators in a

*The semicircular shape is not critical, but was chosen as a convenient shape that reduces the area and hence electron-beam lithography writing time, in comparison to rectangles, without significantly changing the capacitance.

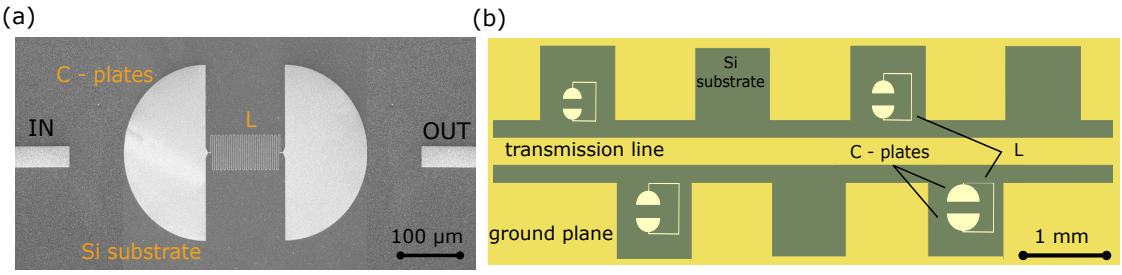


Figure III.6: a. SEM picture of the first type of microwave resonator samples. The resonator consists of capacitively coupled semicircular pads and a meander line inductor. It is coupled to 50 Ohm input and output microstrip transmission lines. b. A digital microscope picture of the second type of samples. Multiple resonators, consisting of capacitor pads and straight inductors, are coupled to a coplanar transmission line in the middle of the sample. Au ground planes surround the resonators to minimize the microwave coupling between them.

circuit with nanotube devices. In particular it is important to ensure that resonators made from the same bilayer as the nanotube devices have high quality factors.

2.2 Measurement Techniques

The measurements of microwave resonators were performed at millikelvin temperatures in an Oxford Instruments dilution refrigerator. Fig. III.7a shows the sample holder with four positions for the samples. Oxygen-free high conductivity copper is used for the sample holder material as it is non-magnetic and has good thermal conductivity at low temperature ensuring good thermalization to the fridge plate. The samples are glued in the holder positions with GE varnish. They are bonded with Au wires to the 50 Ohm impedance coplanar transmission lines on the external circuit board. The transmission lines on the circuit board are connected to the microwave lines in the fridge via MMPX connectors. The samples are isolated from each other with a separate insert lid between the stage and the cover of the sample holder, to minimize the electromagnetic cross-coupling. The sample holder is attached to the 10 mK plate of the fridge. To thermalize the inner conductor of the RF cables, 3 dB attenuators are installed at three different temperature stages in

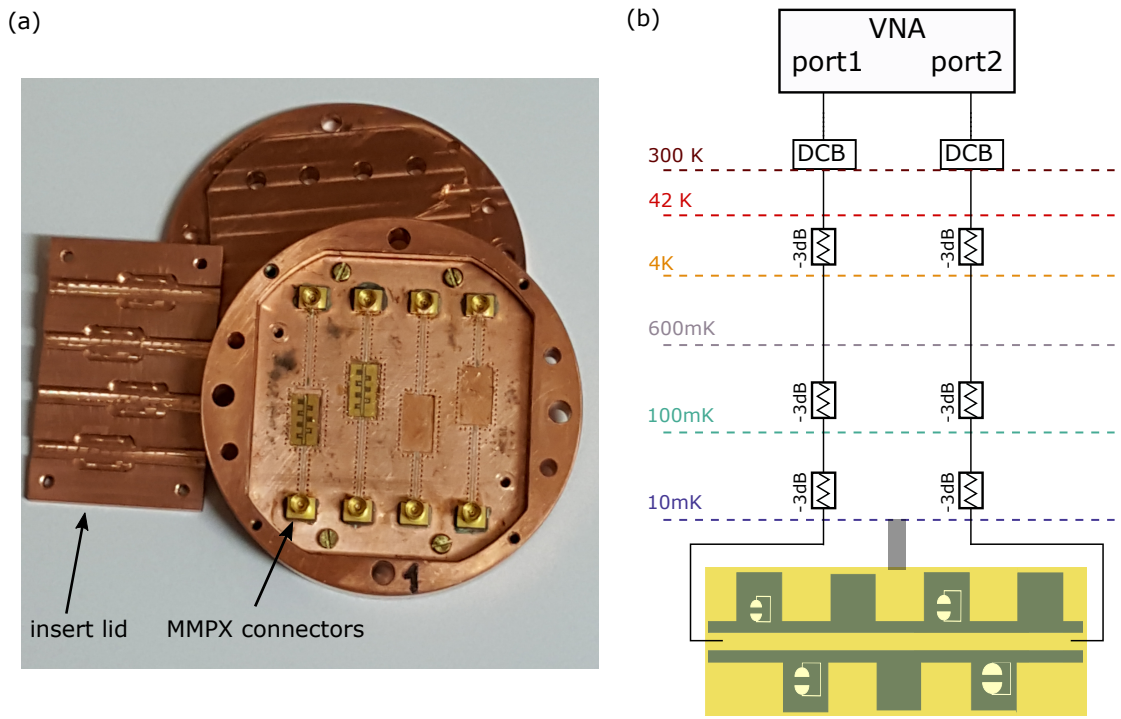


Figure III.7: a. Sample holder of the microwave resonators, showing two samples mounted in the slots. On the left the insert lid is shown, which electromagnetically decouples the samples from each other. The cover of the sample holder is shown on top. MMPX connectors are soldered onto the transmission lines of the circuit board. b. A diagram of the measurement setup. The sample holder is attached to the 10 mK plate of the fridge. Input and output lines are attenuated with 3 dB attenuators at three temperature stages and connected to the signal output and input ports of the vector network analyzer. DC blocks are used at room temperature to decouple the fridge and instrument grounds.

the fridge. Transmission through the resonators is measured with a vector network analyzer (VNA, Rohde & Schwarz ZVA50). Room temperature DC blocks are used to avoid ground loops between the VNA and the fridge. The diagram of the fridge and the measurement setup is illustrated in Fig. III.7b. Temperature dependent measurements are performed by heating up the mixing chamber stage of the fridge.

3 Nanotube-Resonator Coupled Devices

Having established the fabrication and measurement techniques separately for DC nanotube devices and microwave resonators, one can now use these when

preparing and measuring the microwave circuits consisting of nanotube SQUIDs coupled to LC resonators.

3.1 Design and Fabrication of Coupled Devices

Fig. III.8a shows an SEM image of a sample on which nanotube SQUID-resonator coupled devices are fabricated. Each sample consists of four coupled devices, which are capacitively coupled to input and output coplanar transmission lines. Fig. III.8b shows a coupled device with the LC resonators and the nanotube SQUID loop that shares a section of the resonator inductor. An SEM image of a nanotube embedded in the SQUID loop is shown in Fig. III.8c. A gate electrode is capacitively coupled to the nanotube to tune its Fermi energy.

The resonator frequencies are designed to be different from each other by changing the capacitor plate distance. The SQUID dimensions are designed such that it shares a large inductor section with the resonator and therefore the coupling to the resonator is strong. On the other hand, the SQUID should be small enough such that the flux noise threading it, as well as the inductance of the metallic part of the loop is much smaller than the inductance of the nanotube.

When fabricating coupled nanotube-resonator circuits, one should take into consideration the important lithography techniques for the two separate systems. First of all, as mentioned earlier the Pd/Al bilayer is used to achieve highly transparent superconducting contacts. The thicknesses of the deposited Pd and Al metals are important. To find the optimal thicknesses, nanotube DC devices and resonators with different material thickness were fabricated and measured separately. It has been found that the choice of 4 nm and 80 nm for correspondingly Pd and Al layers results in measuring superconducting proximity-induced transport

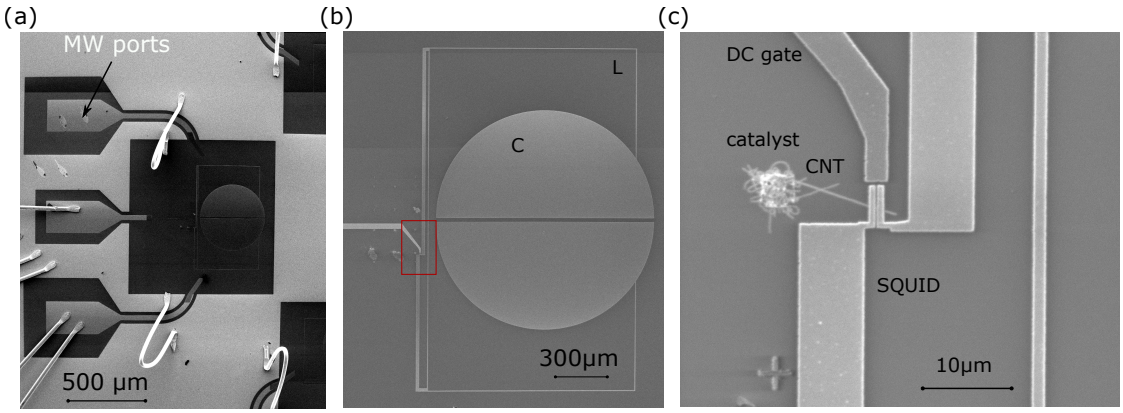


Figure III.8: a. SEM image of a coupled nanotube SQUID - resonator sample. The input and output coplanar transmission lines are bonded to the external PCB and capacitively coupled to the resonator. The DC gate in the middle is bonded to the DC lines on the PCB. The individual devices are isolated from each other with ground planes. Loops of bond wires connect sections of the ground planes, which are also connected on the back of the bond pads. b. SEM image of the resonator coupled to a nanotube SQUID. c. SEM image of a catalyst site and a nanotube integrated in the SQUID loop.

characteristics in DC devices. On the other hand, microwave resonators made from the same bilayer show internal quality factors around 1000.

Since the same bilayer is used for nanotube SQUIDs and resonators, they can be fabricated in the same electron beam lithography and evaporation step. A small number of lithography steps are preferred such that the contamination and damage of nanotubes is kept to the minimum. Similar to the fabrication of resonators, Ti/Au ground planes and coplanar transmission lines are deposited on the substrates. This is done in a photo lithography system with a pre-designed photomask. The nanotube catalyst arrays on the substrates designed for the coupled devices are positioned such that each sample can carry up to four devices. After the photo lithography step, the samples are rinsed in 50°C acetone and isopropanol. The microwave resonators and nanotube SQUIDs are then exposed in an EBL system and Pd/Al bilayer is evaporated in the electron-beam evaporator.

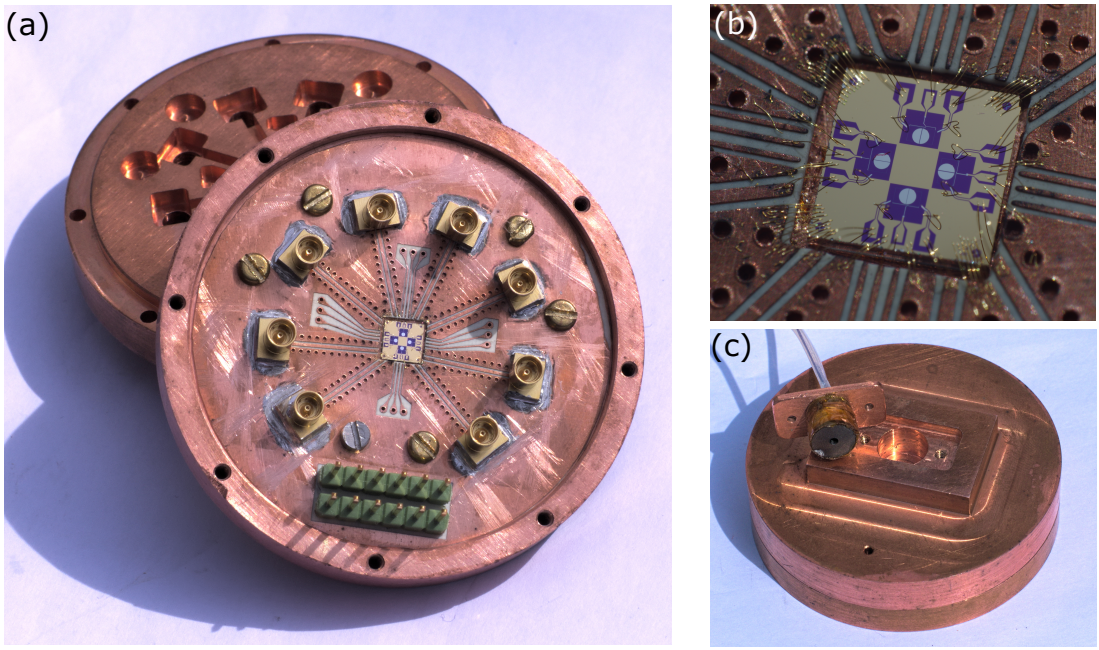


Figure III.9: a. Picture of the copper sample holder used for coupled devices. The PCB combines microwave transmission lines for resonators and DC lines for the nanotube gates. Transmission lines are soldered to MMPX connectors, whereas gate lines are soldered to DC pins. b. Picture of a sample mounted on the holder surrounded with the PCB. Gold bond wires are used to connect the on-chip electrodes and ground planes to the PCB. c. Sample holder picture from the back, showing the circular recess for the coil. The small superconducting magnetic coil shown on top of the sample is made from 0.25 μm NbTi wire. It is glued on a copper stage. The two ends of the coil wire are soldered to a superconducting Nb loom and protected with the plastic tubes in white.

3.2 Measurement Setup

The copper sample holder used for the coupled nanotube SQUID-microwave resonator samples is illustrated in Fig. III.9a. The sample is mounted in the center of the holder, surrounded with the external PCB. The PCB is built using a custom-designed photomask. It combines the microwave lines for the resonators and the DC lines for the gates. Two additional DC lines for each device are designed such that DC transport through the nanotube could also in principle be designed into the devices, though this was not used in experiments so far. The transmission lines of the individual devices are bonded to the coplanar lines of the external PCB with Au bond wires (Fig. III.9b). In order to electromagnetically decouple

individual devices, the ground planes should be kept at the same electrical potential. The ground plane on the sample are bonded to the ground plane of the external PCB via multiple bond wires from all sides of the sample.

The rear side of the sample holder has a circular recess, where a fine superconducting coil is inserted (Fig. III.9c). The coil is used to apply a magnetic flux through the nanotube SQUIDs. The coil is made of 8000 turns of NbTi wire (SC-T48B-M-0.025 mm wire acquired from Supercon) and has a diameter of 2.5 mm and length of 5 mm. It has an estimated inductance of 0.07 H and is at around 1.5 mm distance from the sample.

The sample holder is fixed at the 10 mK plate of the dilution fridge. It is necessary to isolate the sample from the external magnetic noise, especially when using fine magnetic coils. For this reason, cylindrical magnetic shields are used, made of 1 mm thick mu-metal (high magnetic permeability metal alloy).

Fig. III.10a shows the diagram of the measurement setup. As before, room temperature DC blocks are used to decouple instrument grounds from the fridge ground and avoid ground loops. The input signal is attenuated via 20 dB attenuators at three temperature stages and is connected to the input coplanar transmission line. MMPX connectors are soldered to the transmission lines on the PCB to connect the latter with microwave cables. The output signal from the device is connected to a microwave switch, which allows measuring multiple devices using the same input and output microwave lines. The switch is controlled with an Arduino board by sending DC pulses through the Nb superconducting DC loom. The output microwave line is connected to a cryogenic 12 GHz low-pass filter and 8-12 GHz band-pass filter. Two Raditek 8-12 GHz circulators are used at the base plate to redirect the thermal noise coming from a cryogenic amplifier into a 50 Ohm

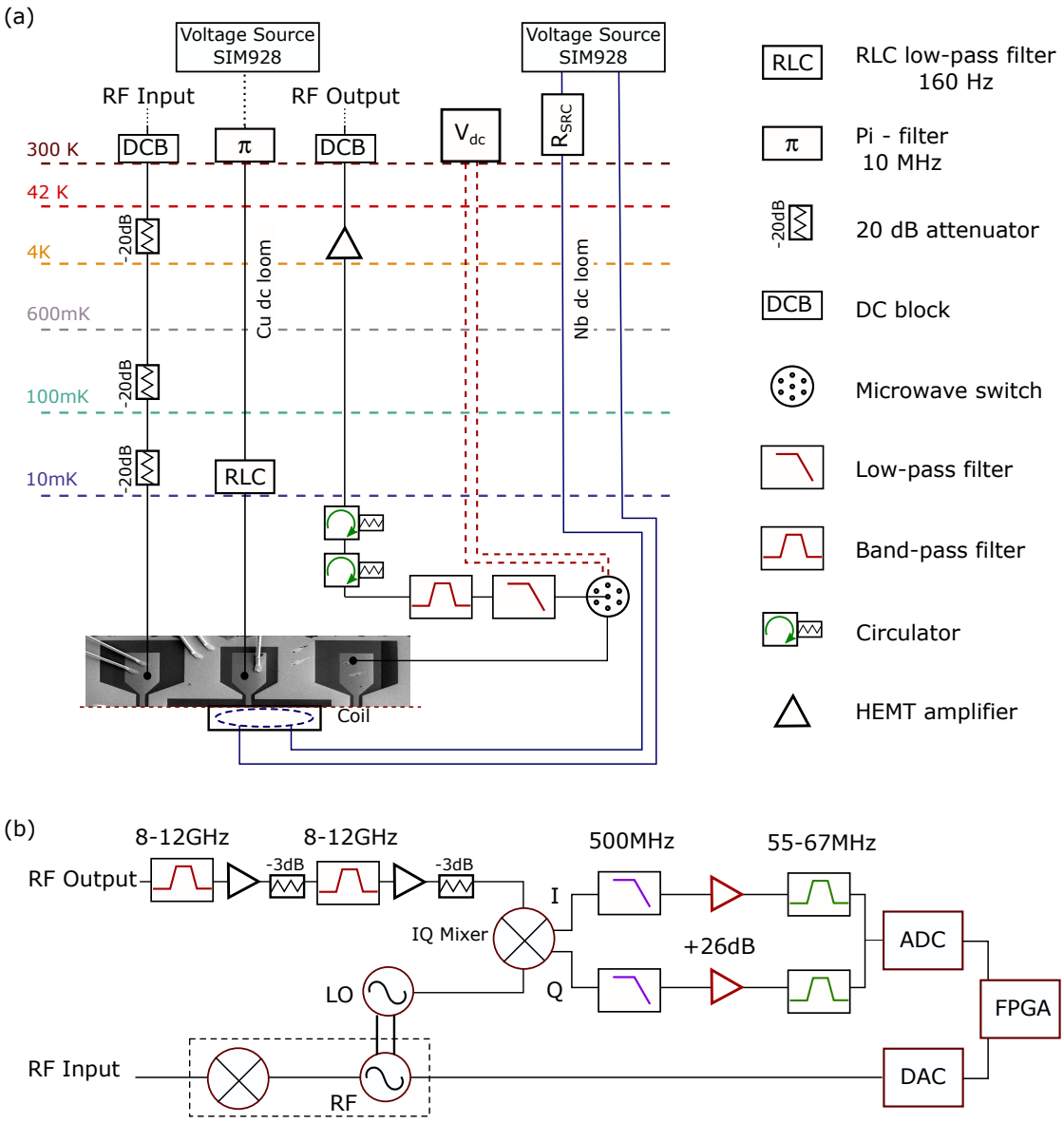


Figure III.10: A schematic diagram of the RF setup for coupled device measurements.

termination*. Past the circulators, the cables are attached to an ultra-low noise HEMT amplifier with a bandwidth of 1-12 GHz, which amplifies the signal by 39 dB. The amplifier is thermalized at the 4 K stage of the fridge.

Cu and Nb DC looms are used correspondingly for connecting the gates to the nanotubes and the magnetic coil to the external current source. All three of the DC looms are well-thermalized between two metallic plates mounted at each stage

*Circulators are passive devices, usually with three ports, that redirect the input microwave signal at port i to the port $i+1$.

of the fridge using a thermally conductive grease. The wires of the Cu loom are connected to the 160 Hz low-pass filters and Pi-filters described in the previous section. SIM928 voltage source is used to send signal to the gates. A second SIM928 source in series with a large resistor is used to supply current to the coil.

First measurements of the transmission through the devices are done with the VNA. In this case the 'RF Input' and 'RF Output' in the diagram are respectively attached to signal output and input ports of the VNA.

Better accuracy measurements of the resonance response when tuning the gates and the coil are done using an FPGA (field-programmable gate array) as illustrated in the diagram of Fig. III.10b. The input signal to the device (RF) is supplied by microwave signal generator (Rohde & Schwarz SGS100A) and an upconverting IQ mixer controlled from the FPGA via a digital-to analogue converter (DAC) board. The wave generator can output powers between -130 dB and $+30$ dB, and frequencies in 100 kHz-22 GHz range. The output RF signal from the device is additionally filtered with room temperature *K&L* 8-12 GHz band-pass filters. It is amplified by two wideband low noise amplifiers each by $+28$ dB. Two -3 dB attenuators are used for stopping the thermal reflections from the amplifiers from going back down the cables. A second signal generator is used for the local oscillator (LO) to drive the IQ downconverter mixer. The output I and Q components of the signal are subsequently filtered with 500 MHz low-pass filters, amplified by $+26$ dB and filtered with $55-67$ MHz band-pass filters. The combined signal is then passed to the analogue-to-digital converter (ADC) board on the FPGA. The RF and LO signal generators are set to operate at the same frequency and their relative phase is locked.

IV

DC Transport in Nanotube Devices

Contents

1 Normal Metal Contacted Nanotubes 76
- 1.1 High Interface Barrier: Coulomb Blockade 76
- 1.2 Medium Interface Barrier: Kondo Effect 79
- 1.3 Low Interface Barrier: Fabry-Perot Interference 80

2 SN-bilayer Contacted Nanotubes 82
- 2.1 Multiple Andreev Reflection in the Fabry-Pérot Regime 82
- 2.2 MAR at Fabry-Perot to Coulomb Blockade Transition . 91
- 2.3 Interplay of Four-fold Degeneracy and Multiple Andreev Reflections in a Carbon Nanotube Quantum Dot 105
- 2.4 Discussion and Conclusion 111

In this chapter experimental results of measured nanotubes contacted by normal metal and superconductor-normal (SN) bilayers are presented. In normal metal contacted devices, we observe the expected range of physical effects, dependent on contact transparency, namely Coulomb blockade, Kondo effect and Fabry-Pérot interference. In SN-bilayer devices we observe the interplay between the above effects and Andreev reflection processes.

1 Normal Metal Contacted Nanotubes

In this section we present the DC transport measurements of carbon nanotubes contacted by 50 nm Pd layer. The motivation behind these experiments is to test metal-nanotube contacts and to estimate the interface transparency between the Pd layer and the nanotube.

As discussed in Section II.1.1.3, Pd is known to be a good metal for achieving high transparency contact interfaces with nanotubes. This is due to the good match between the work functions of the Pd and the nanotube. In addition to this, Pd tends to uniformly cover the nanotube due to its good wetting properties.

The transport regime through the nanotube changes as the interfaces between the nanotube and the metallic contacts go from being highly reflecting to being highly transmitting [10]. The measurements of the different transport regimes depending on the interface tunnel barrier height are discussed in the following sections.

1.1 High Interface Barrier: Coulomb Blockade

As discussed in Section II.1.2, when the nanotube is weakly tunnel-coupled to the metallic leads, single electron charging can be detected through the quantum dot formed in the nanotube. Transport measurements of a two-terminal nanotube device with high tunnel barriers at the interfaces at 10 mK show clear signatures of the Coulomb blockade. In Fig. IV.1a, the measurement of the differential conductance as a function of the gate voltage at zero source-drain voltage is shown. Coulomb resonances separated with conductance valleys can be seen. When tuning the source-drain voltage across the device these resonances evolve to form the familiar Coulomb diamonds Fig. IV.1b. The regularity of the Coulomb diamonds indicates that the measured nanotube is free of disorder [143].

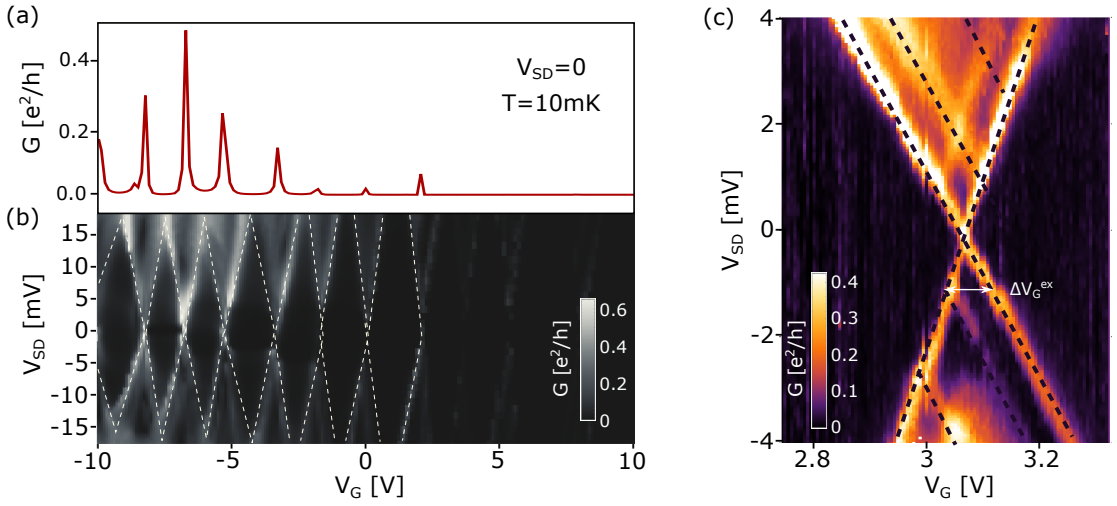


Figure IV.1: a. Differential conductance of a carbon nanotube device (DC-Pd-1, see Appendix B for device description) at $V_{SD} = 0$ and $T = 10\,\text{mK}$ when tuning the gate voltage. A sequence of Coulomb resonances separated by conductance valleys are observed. b. Stability diagram of a carbon nanotube device at 10 mK obtained by tuning gate and bias voltages. Coulomb diamonds are observed. The conductance is decreased with increasing gate voltage due to the semiconducting nature of the nanotube. b. A detailed measurement of a Coulomb resonance showing resonances parallel to the diamond edges due to the transport through the excited states.

For positive gate voltages the conductance strongly decreases, which is an indication of a p-type semiconducting device. This semiconducting nature of the nanotube has been additionally confirmed in measurements at room temperature, where a strong gate-dependence of the conductance has been observed.

The conductance of the nanotube at low temperature changes between 0 and $0.65G_0$, where $G_0 = e^2/h$ is the conductance quantum. In the differential conductance measurement the four-fold degeneracy of the nanotube quantum levels is not observed. The addition energy of the quantum dot, given by Eqn. II.6, can be estimated from the intersection of the diamond edges, where $\mu_{N-1} = \mu_S$ and $\mu_N = \mu_D$. μ_S and μ_D are the chemical potentials of the source and drain leads. Taking into account that $V_{SD} = (\mu_S - \mu_D)/|e|$ one can obtain $E_{add} \approx 18\,\text{meV}$. Using the quantum dot capacitance model described in Section II.1.2 and [70], one can estimate additional parameters describing the quantum dot. In this model, the

nanotube quantum dot is represented as a metallic island with a discrete energy spectrum. The electron-electron interactions on the island as well as with the electrons on the leads are given by coupling capacitances. The coupling capacitance of the dot to the gate electrode is calculated from the width of the Coulomb diamond, $C_G = |e|/\Delta V_G \approx 0.089\,\mathrm{aF}$. Using the equations for the slopes of diamond edges introduced in Section II.1.2.4, the coupling capacitances of the dot to the source and drain electrodes can be found as $C_S = 3.9\,\mathrm{aF}$ and $C_D = 4.6\,\mathrm{aF}$. Note that there is a slight coupling asymmetry between the two leads and the nanotube which results in diamonds being at an angle with respect to the perpendicular axis. The gate capacitance is almost two-orders of magnitude lower than source and drain capacitances, which is a result of the side-gate geometry and the strong screening of the gate electrode from the nanotube by the source and drain contacts. The gate lever arm describing its efficiency can be calculated from the slopes to be $\alpha_G = 1/(\beta_S - \beta_D) = 0.014$.

When the excited states of the quantum dot are in the bias window and their relaxation rate is lower than the tunneling rate through the dot, transport through these states can be detected in the charge stability diagram (see Section II.1.2.5). Fig.IV.1b shows a detailed measurement of a Coulomb diamond in a smaller voltage range. One can see additional lines parallel to the diamond edges owing to the transport through the excited states. The single particle excitation energy Δ can be found from the stability diagram by using the following equation:

$$\Delta = \mu_N^{(1,0)} - \mu_N^{(0,0)} = \frac{e}{|\Delta V_G^{ex}|}. \qquad \text{(IV.1)}$$

ΔV_G^{ex} is the distance between the intersections of the ground and excited state transport resonances with the gate axis. Using the obtained value for the lever arm, we find $\Delta = 1.2\,\mathrm{meV}$. This value can be compared with the value obtained from

the momentum quantization along the tube axis given by Eqn. II.3. Taking into account the Fermi velocity in the nanotube $v_F = 8.1 \cdot 10^5\,\mathrm{m/s}$ and the designed nanotube length $L = 300\,\mathrm{nm}$, we obtain $\Delta = 1.4\,\mathrm{meV}$. Therefore, there is a good agreement between the obtained values of Δ. Note that Eqn. II.3 ignores the valley degree of freedom. In disordered nanotubes this causes a reduction of the level spacing by a factor of two. From the average size of the Coulomb diamonds the charging energy is estimated as $E_c \approx 17\mathrm{meV}$.

1.2 Medium Interface Barrier: Kondo Effect

When the coupling of the quantum dot to the metallic leads increases transport mechanisms such as Kondo effect can result in additional features appearing in the stability diagram [10]. In this case, contrary to what one might expect from normal Coulomb blockade, zero-bias conductance ridges develop in every second diamond. As explained in Section II.1.3, transport due to the Kondo effect happens when the quantum dot has an odd number of spins (its net spin is $S = 1/2$). Fig. IV.2 shows the differential conductance of an example nanotube device exhibiting Kondo transport. Maximum value of the conductance through the device is $2.8e^2/h$. The stability diagram shows the usual picture of the Coulomb blockade. In addition to this high conductance resonances at zero-bias are observed in alternating diamonds, where the number of the electrons on the dot is odd. Due to intermediate transparency contacts significant cotunneling is allowed which tends to smear the features. The width of a Kondo resonances is a measure of the binding energy of the spin-singlet state of the quantum dot-metallic lead correlated system. It is characterized by the Kondo Temperature T_K described in Section II.1.3. By fitting the observed Kondo resonances to a Lorentzian shape, one can obtain $T_K = 4.8\,\mathrm{K}$, 11 K, 7.1 K and 6.7 K correspondingly for K_1-K_4. Fig. IV.2b shows data and the

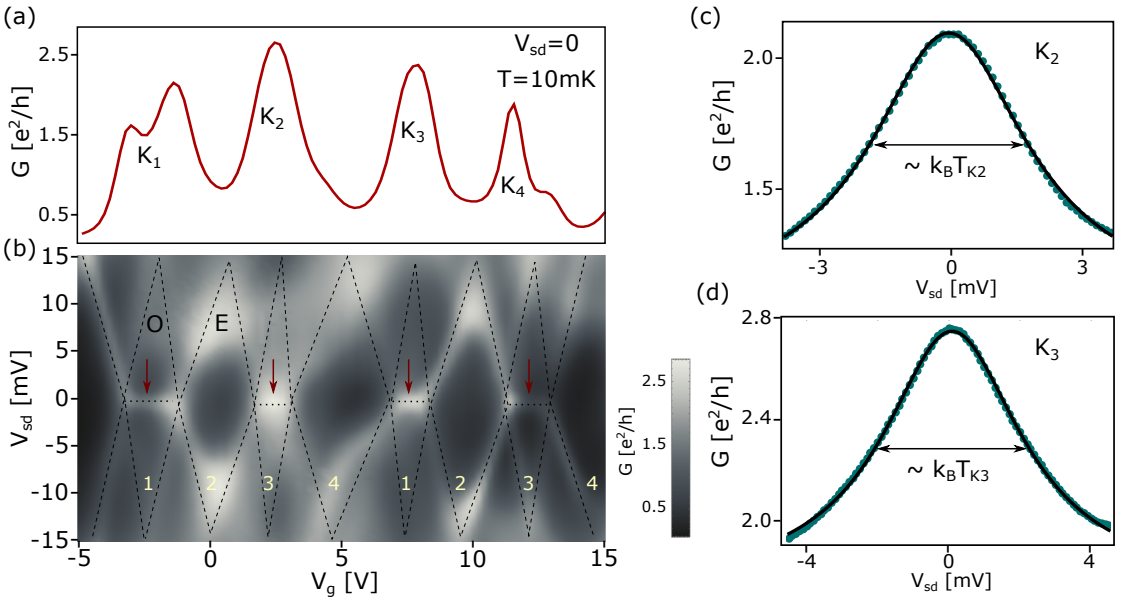


Figure IV.2: a. The differential conductance of a nanotube device (DC-Pd-2) at zero bias voltage and 10 mK with an intermediate height of the interface tunnel barriers. b. Stability diagram showing a Coulomb blockade pattern. Kondo resonances at zero bias voltage are observed in diamonds, where the total spin of the dot is $S = 1/2$. c,d. Cross-sections of the Kondo ridges observed in two diamonds fitted to Lorenzian functions. The Kondo temperature is obtained from the widths of the Kondo resonances.

fitted curves for resonances K_2 and K_3. These measurements are in agreement with other studies of the Kondo effect in single walled nanotubes [13, 52]. Note that the four-fold shell structure of the nanotube is probably observed here reflected in the stability diagram by the alternating sizes of the diamonds enumerated as 1-4.

1.3 Low Interface Barrier: Fabry-Perot Interference

Nearly perfect, barrier-free metal-nanotube interfaces can be achieved when using Pd as the contacting material. In this case, when the transport through the nanotube is ballistic, conductance can reach its theoretical value of $4e^2/h$. In other words, when the phase coherence length is the longest in the nanotube device, the electron wave functions backscattered from the partially-reflecting interfaces can constructively and distructively interfere with each other. This results in a Fabry-Pérot interference pattern in the differential conductance measurement when

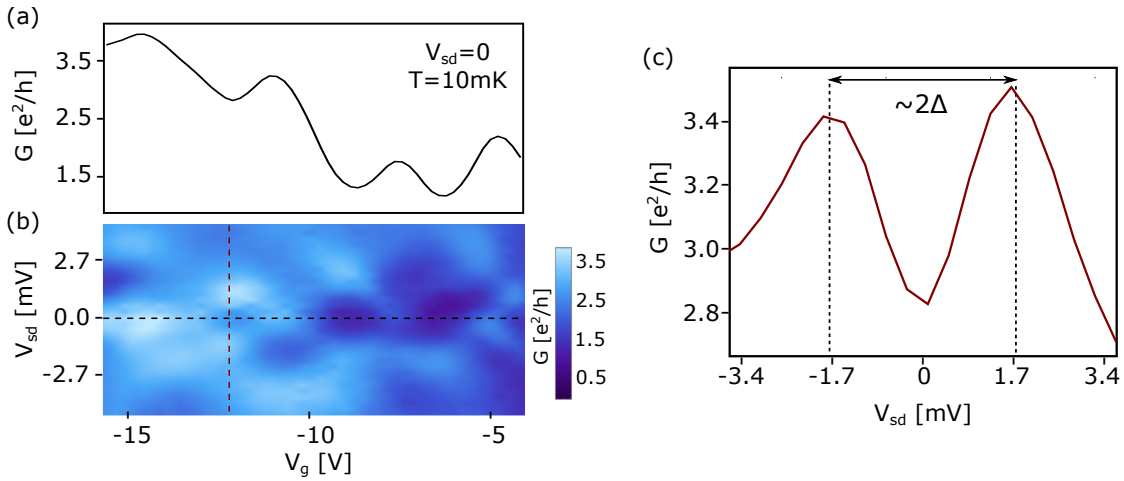


Figure IV.3: a. Differential conductance of a carbon nanotube device (DC-Pd-3, see Appendix B) measured at $V_{sd} = 0$ and 10 mK showing oscillations with the gate voltage. b. Stability diagram of Dc-Pd-3 showing a checkerboard pattern due to Fabry-Pérot interference of particle waves in the nanotube. c. A cross-section of b at the position of the vertical dashed red line. The nanotube quantum dot level spacing is found from the distance between the two conductance peaks.

changing gate and bias voltages.

A measurement of an example nanotube device with highly transparent interfaces is illustrated in Fig. IV.3. The measured device is designed to have a contacted nanotube section length of 1 μm. Fig. IV.3a shows a measurement of the differential conductance as a function of the gate voltage. Unlike the previous devices, where sharp conductance resonances were observed, now the conductance undergoes broad oscillations. When tuning also the gate voltage a checkerboard pattern of the conductance can be observed (Fig. IV.3b). Such behaviour has been observed in around 25% of Pd contacted nanotubes. The maximum value of the conductance in the measured gate range is $3.8e^2/h$. From this value the coupling asymmetry of the nanotube to the source and drain leads can be estimated from Eqn. II.8 to be $\Gamma_S/\Gamma_D = 0.67$. Regarding the nanotube as a quantum dot with discrete energy levels, the level spacing can be approximately estimated by the distance of the conductance resonances as shown in the Fig. IV.3c. Using Eqn. II.16 one

can find $L \approx 980\,\mathrm{nm}$, which agrees with the designed nanotube length. Note that when obtaining this value linear dispersion has been assumed. This assumption is valid as the stability diagram in the applied gate voltage range does not exhibit a semiconducting gap. On the other hand, due to the fact that the room temperature measurements of the device show a negligible gate dependence of the differential conductance, the nanotube is believed to be metallic.

2 SN-bilayer Contacted Nanotubes

When a carbon nanotube is contacted with superconducting leads new phenomena are observed in the transport measurements relating to the tunneling of Cooper pairs and to Andreev reflection processes. In this section we present measurements of devices contacted by Pd(4 nm)/Al(80 nm) bilayer in different interface transparency regimes.

2.1 Multiple Andreev Reflection in the Fabry-Pérot Regime

In hybrid superconductor-carbon nanotube devices Andreev reflection is the main transport mechanism within the superconducting gap. Therefore, it is responsible for the so-called sub-gap structure (SGS) observed in measurements of the density of states or stability diagram of such devices.

The transport characteristics due to the superconducting nature of the leads are most clearly observed when the metal-nanotube contact transparencies are high. In this case the normal state transport characteristics typically correspond to Fabry-Pérot oscillations of the differential conductance. In this section measurements of the interplay of the Fabry-Pérot transport regime with the transport characteristics due to the multiple Andreev reflections is presented.

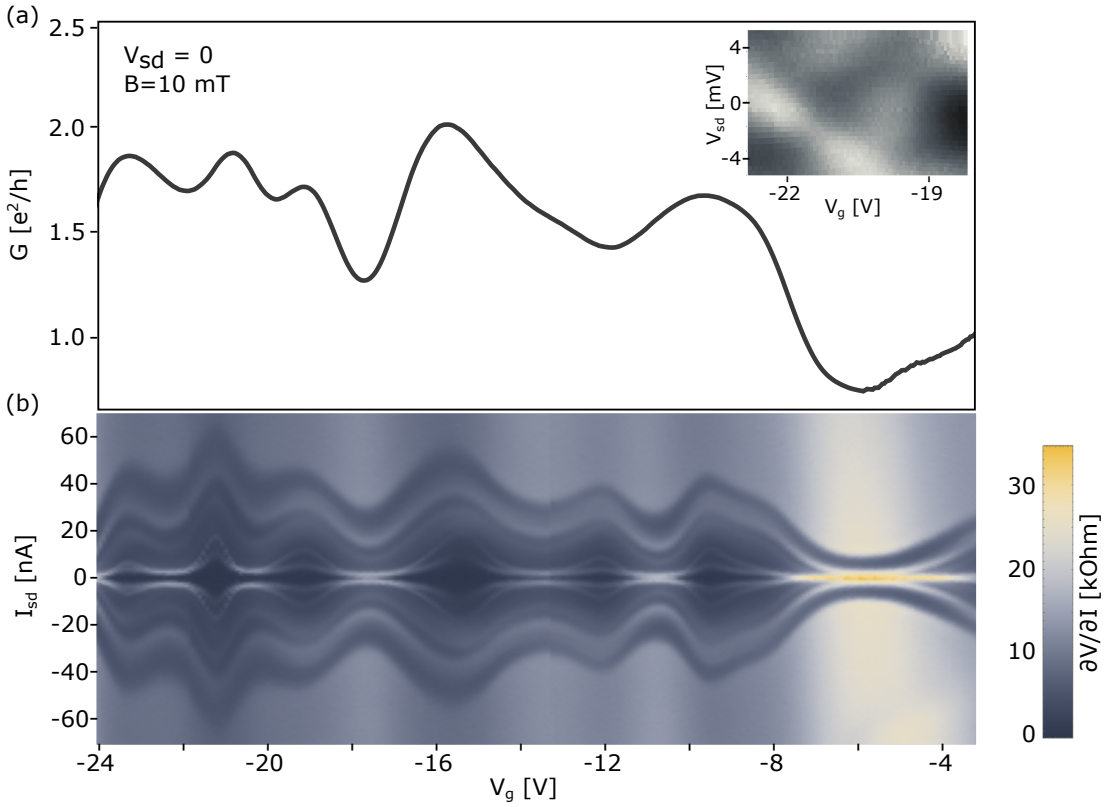


Figure IV.4: a. Differential conductance as a function of the gate voltage when the contacts to the nanotube are turned normal by applying a perpendicular magnetic field of $B = 140\,\mathrm{mT}$ (device label DC-SN-1 in Appendix B). The broad oscillations of the conductance are due to Fabry-Pérot interference of the reflected electron waves in the nanotube. The inset shows the stability diagram obtained by tuning the gate voltage. The checkerboard pattern of the differential conductance can be clearly seen. b. Differential resistance of the nanotube device as a function of the bias current and the gate voltage. Resonances modulated with the gate voltage are due to multiple Andreev reflections of different orders. The black region near zero bias current is due to the proximity-induced supercurrent flowing through the nanotube.

The length of the measured device is 300 nm and it is made of the Pd (4 nm)/Al (80 nm) bilayer. The resistance of the device measured at room temperature on the probe station is around 20 kOhm. At room temperature, the resistance shows no noticeable gate-dependence indicating the metallic nature of the nanotube. Low temperature measurements of the differential resistance as a function of the bias current and gate voltage are done at 10 mK in the dilution fridge. The transparency of the interfaces and the transport regime of the nanotube device are

first characterized for normal contacts by applying a magnetic field, $B \approx 10\,\mathrm{mT}$ perpendicular to the sample. Fig. IV.4a shows a measurement of the differential conductance of the nanotube device in the normal state of the contacts when tuning the gate voltage. The observed broad oscillations of the conductance are a result of the Fabry-Pérot interference of the electron wave functions. The device shows a maximum conductance value of $2.35\,e^2/h$. The inset of Fig. IV.4a shows a checkerboard pattern the conductance with a characteristic voltage scale of 5.5 meV corresponding to the energy level separation between the discrete electronic states. Using Eqn. II.16 the distance at which the reflection of the electron waves happens is found to be $L \approx 305\,\mathrm{nm}$. The obtained value is consistent with the designed nanotube length of 300 nm, therefore the electrons reflect at the nanotube/metal interfaces and the electron transport in the nanotube is nearly ballistic.

When the magnetic field is turned off, the contacts become superconducting and new features are observed in the transport through the nanotube at low current bias. In this case, it is more appropriate to plot the differential resistance than the conductance, since this approaches a constant value of zero when a non-dissipative current flows. When the contacts are superconducting, the transport through the nanotube is strongly affected by the superconducting proximity effect. This is evident from the measurement of the differential resistance as a function of the bias current and the gate voltage Fig. IV.4b. In addition to the broad Fabry-Pérot oscillations, fine features are observed which move up and down with the gate voltage. The dark region in the vicinity of zero bias corresponds to a non-dissipative current or supercurrent flowing through the nanotube. It can be seen that the maximum value of the supercurrent is modulated by the gate voltage. As no semiconducting gap is observed in the measurement, the nanotube is believed to be metallic. This means that the gate dependence of the supercurrent is different than in conventional

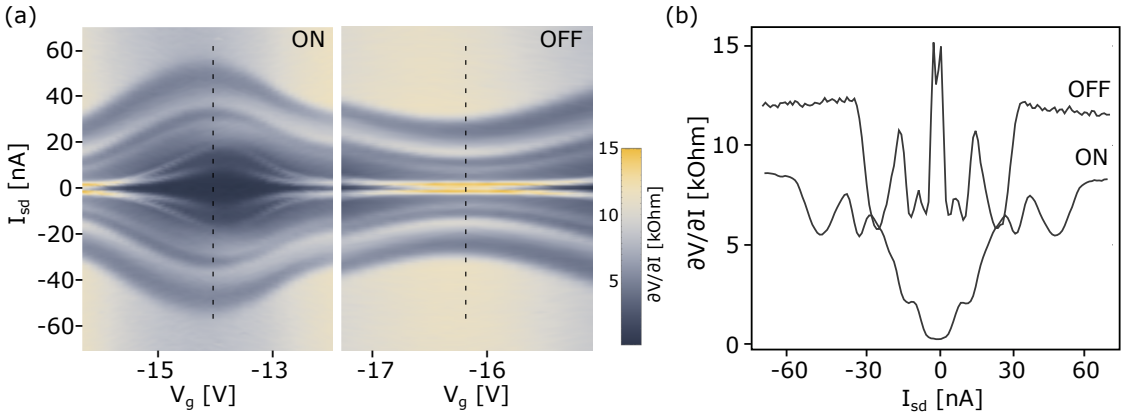


Figure IV.5: a. Differential resistance in two gate voltage regions where either large supercurrent is observed or it is suppressed corresponding to the 'On' and 'Off' states of the supercurrent transistor. b. The vertical cross-sections at the positions shown in a. Along with the observed MAR peaks in the 'On' state a critical current exists below which the resistance switches to zero. In the 'Off' state the supercurrent is strongly suppressed and a finite zero-bias resistance is observed.

semiconducting devices. When comparing the behaviour of the maximum of the supercurrent with that of the normal state differential conductance at zero bias, one can notice a consistent trend (Fig.IV.4). Whenever the normal state conductance is high, the supercurrent through the nanotube is largely enhanced. On the other hand, at the valleys of the normal state conductance, the supercurrent is strongly suppressed. Therefore, the modulation of the supercurrent is due to tuning the discrete quantum levels in the nanotube on and off resonance with the Fermi level of the leads when changing the gate voltage. This behaviour has been observed before [33] and suggested to be of use in a 'supercurrent' transistor. The enhancement and suppression regions of the supercurrent are correspondingly referred to as the 'On' and 'Off' states of this 'supercurrent' transistor. Here we will concentrate on gaining further understanding of the fine features of the superconducting behaviour and their relation to Andreev reflection processes in the nanotube.

The detailed measurements of the two transistor states are shown in Fig. IV.5a. The cross-sections in the two cases show two distinct behaviours of the differential

resistance with the bias current. In the 'On' state, the resistance decreases with the decreasing bias current and below a critical current becomes zero. Therefore, below the critical value of the applied current a supercurrent is flowing through the nanotube. On the other hand in the 'Off' state the resistance increases with the decreasing bias until it reaches a strongly suppressed value of the supercurrent. In addition to this, multiple Andreev reflection peaks are observed in both states.

The current-biased measurement is useful when it is necessary to visualize the regions of the supercurrent flow. However,we can learn more about the fine features observed at low current bias by plotting the data instead as a function of voltage bias. This is done by independently measuring the voltage drop across the nanotube. The differential conductance is plotted as a function of the measured source-drain voltage and the gate voltage. Fig. IV.6a shows the resulted plot for the same gate voltage range as in Fig. IV.4b. The transport due to the multiple Andreev reflections is revealed as a series of nearly gate-independent horizontal resonances appearing at $2\Delta_g, \Delta_g$ and $2/3\Delta_g$, where the superconducting energy gap is estimated to be $\Delta_g = 125\,\mu$eV. This corresponds to a critical temperature of about 850 mK, which is reduced from the Al critical temperature due to the normal Pd layer.

As discussed in Section II.2.2, in SNS structures the Andreev reflections of particles at the interfaces result in cooper pair transport from one superconductor to the other. Depending on the bias voltage, transport can occur due to n successive Andreev reflections, resulting in conductance peaks appearing at $V_{SD} = 2\Delta/ne$, where Δ is the superconducting gap energy and n is an integer. For n=1,2,3, the conductance peaks correspond to quasiparticle transport and 1st and 2nd order multiple Andreev reflections (see Fig. II.11). The observed peaks in Fig.IV.6 are consistent with these for $\Delta = 125\,\mu$eV.

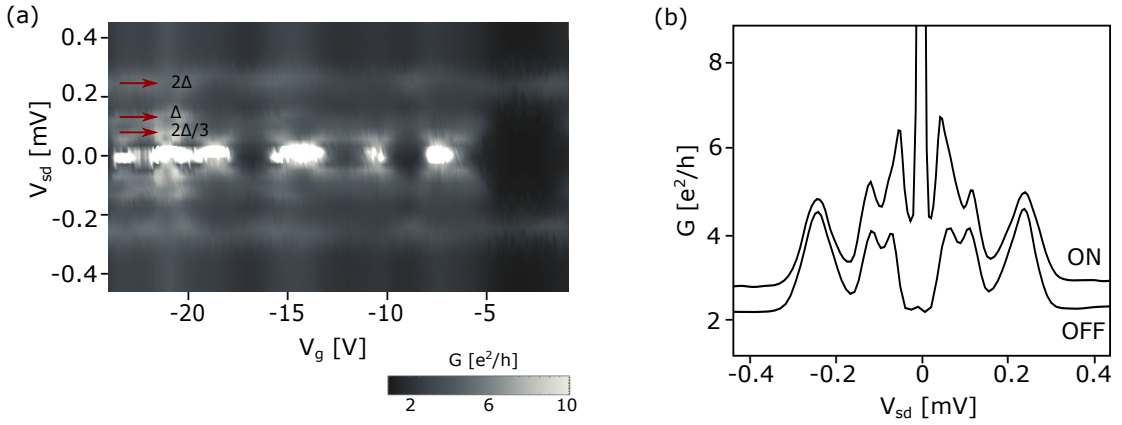


Figure IV.6: a. Differential conductance as a function of the measured sourcee-drain voltage and the gate voltage. MAR peaks appear as gate-independent resonances at bias voltages $2\Delta/ne$, where Δ is the gap energy and $n = 1, 2, 3$. The white features near zero bias are due to the conversion at the supercurrent region. b. The cross-sections in the two states of the supercurrent transistor. Large supercurrent peak is observed at zero bias in the 'On' state. In the 'Off' state the supercurrent peak is strongly suppressed. For clarity the data is limited from above to $9\,e^2/h$.

Fig. IV.6b shows the cross-sections at gate voltages in the two states. In the 'Off' states the supercurrent peak at zero-bias is strongly suppressed, whereas in the 'On' state a large supercurrent peak exists with a maximum conductance reaching a conductance value of $80\,e^2/h$.

2.1.1 Temperature Dependence of the Sub-Gap Structure

Additional proof of the nature of the observed sub-gap structures is done by performing temperature and field-dependent measurements. Fig. IV.7a and b show respectively the temperature dependences of the differential resistance as a function of the bias voltage in the 'On' and 'Off' states. The corresponding plots of the differential conductance as a function of the bias voltage in the two states for increasing temperature are illustrated in Fig. IV.7c and d. The quasiparticle transport peaks at $\pm 2\Delta/e$ and 1-st and 2-nd order MAR peaks correspondingly at $\pm\Delta/e$ and $\pm 2\Delta/3e$ can be seen. The conductance curves at different temperature values are shifted upwards by e^2/h for clarity. When the temperature increases

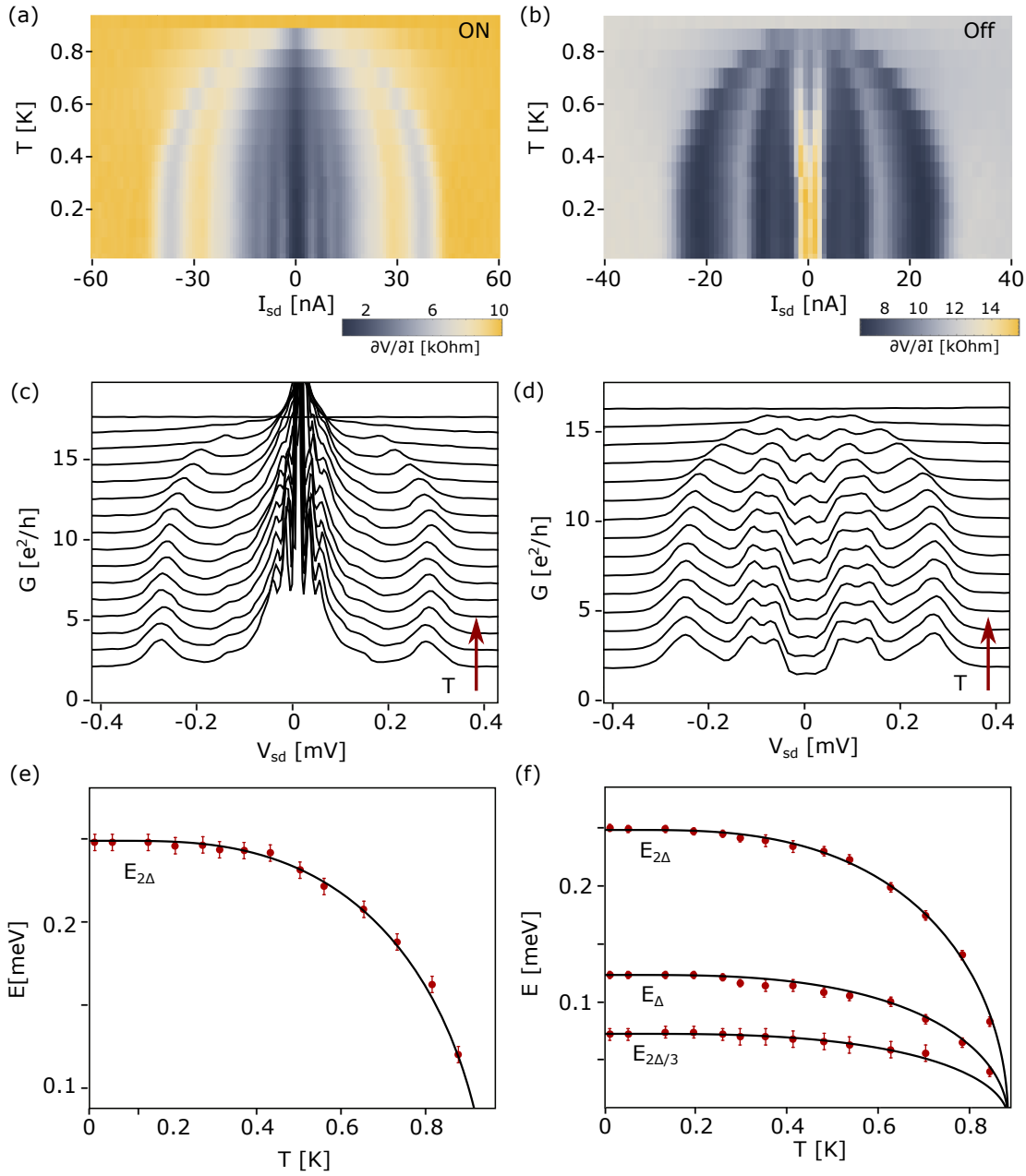


Figure IV.7: a,b. $\delta V/\delta I$ in the 'On' and 'Off' states measured as a function of the temperature. With the increasing temperature the superconducting gap closes and the peaks disappear. c,d. $G = \delta I/\delta V$ in the two states plotted as a function of the measured bias voltage for increasing temperature. The curves at different temperatures are shifted upwards for clarity. In the 'On' state a large zero-bias peak is observed with decreasing amplitude. In the off state a small zero-bias peak emerges as the temperature is increased due to the thermal tunneling of Cooper pairs. e,f. Energies at which the observed peaks appears as a function of the temperature that decrease due to the suppression of the gap. Data is fitted with Eqn. IV.2 yielding $\Delta = 123\,\mu$eV and $T_c = 880\,$mK.

the quasiparticle transport and MAR peak energies decrease. This is due to the suppression of the superconductivity of the leads and the decrease of the gap energy Δ_g. In the 'On' state, the amplitude of the supercurrent peak decreases and disappears with the temperature. In the 'Off' state a small zero-bias peak emerges for intermediate values of the temperature and disappears at the critical temperature. This peak is believed to be due to thermal cotunneling of Cooper pairs [144]. The temperature evolution of the conductance peak energies $E^{j\Delta}$ in the two transistor states are shown in Fig. IV.7c and f. The data is fitted with the approximate BCS gap function [34],

$$E^{j\Delta} = K_{j\Delta}\Delta_0 tanh(1.74\sqrt{T_c/T-1}), \tag{IV.2}$$

where the BCS gap at zero temperature is given by $\Delta_0 = 1.76\, k_B T_c$ which is estimated to be $125\,\mu$eV. $K_{j\Delta}$ coefficients and the critical temperature act as the fitting parameters. We obtain $K^{On}_{2\Delta}/K^{On}_{\Delta} = 2.02 \pm 0.026$, $K^{Off}_{2\Delta}/K^{Off}_{2\Delta} = 2.01 \pm 0.034$ and $K^{Off}_{2\Delta/3}/K^{Off}_{\Delta} = 0.6 \pm 0.058$*. The coefficients of 2Δ peaks are consistent with each other as well as the expected values for quasiparticle transport and MAR peaks. The fitted value of the critical temperature is 880 mK, which agrees with the value estimated from the gap energy in the previous section.

2.1.2 Magnetic Field Dependence of Sub-Gap Structure

Next, the magnetic field dependence of the sub-gap structure is studied. It is shown for the 'On' and 'Off' states of the transistor in Fig. IV.8a and b. Similar to the temperature dependence, the observed sub-gap structures disappear as the field is increased. The voltage-biased cross-sections at the two states are illustrated in Fig. IV.8c and e. As before, the curves are shifted upwards for clarity. The increase

*$K^{On}_{\Delta} = K^{Off}_{\Delta} = 1$ has been used in the fitting.

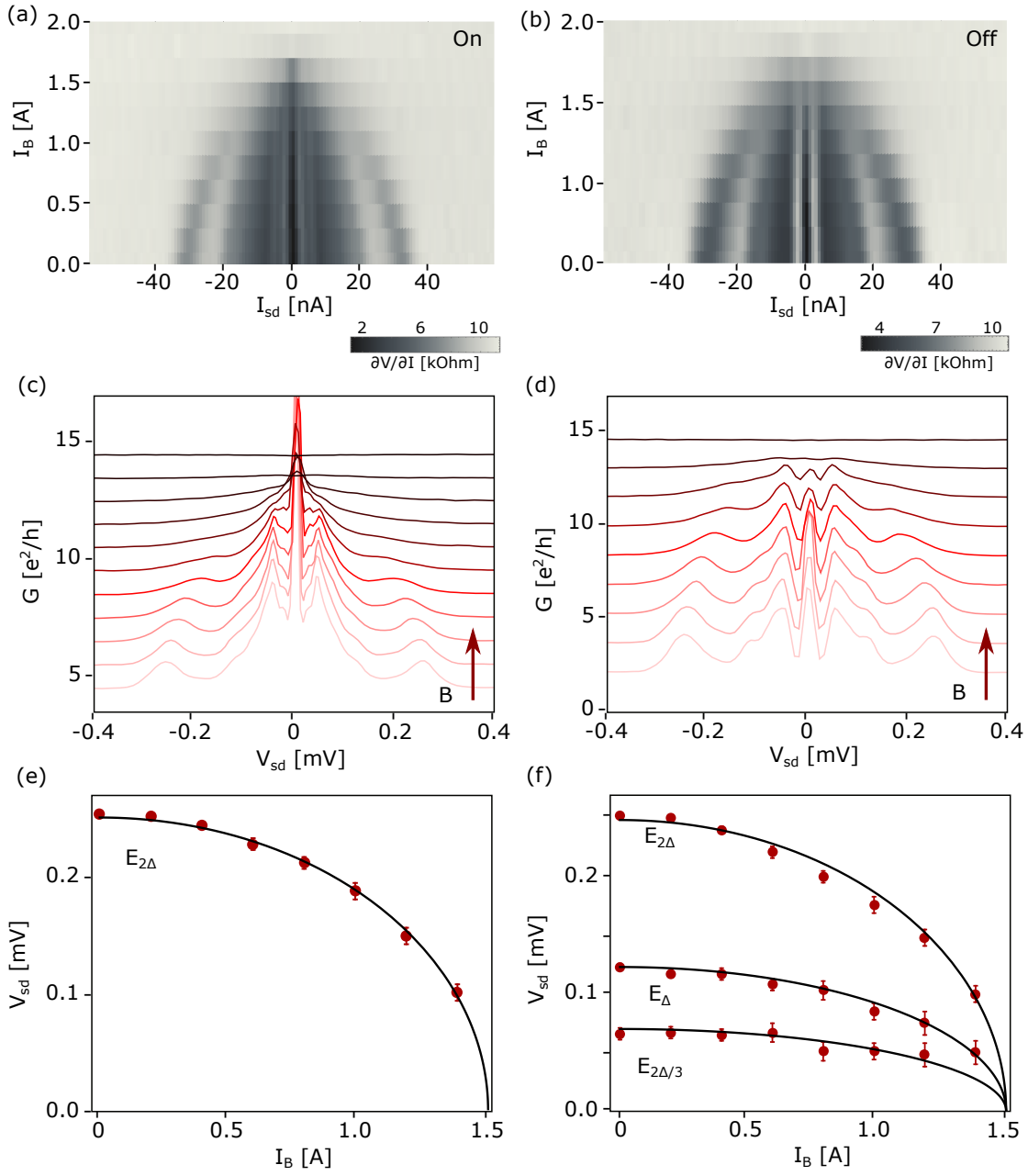


Figure IV.8: a,b. Colorplots of magnetic field dependence of the sub-gap structures in a current-biased measurement for respectively 'On' and 'Off states'. As the field increases the gap closes and the structures disappear. c,d. Differential conductance as a function of the measured voltage bias for increasing magnetic field respectiveli in 'On' and 'Off' states. The MAR peaks are observed with decreasing amplitudes and energies at which they appear. Large supercurrent peak is observed in the 'On' state with a decreasing amplitude. e,f. The positions of 2Δ, Δ and $2\Delta/3$ peaks as a function of the applied fields correspondingly in the two states. The data is fitted with Eqn. IV.3.

of the field results in a decrease of the absolute value of the MAR peak positions as well as their amplitudes. The 'Off' state cross-section is taken at a gate voltage value where the supercurrent peak at the zero-bias is not completely suppressed. In both states the zero-bias peak amplitude decreases with the field eventually disappearing at the critical field. The energies of the quasiparticle tunneling and MAR peaks as a function of the applied magnetic field is plotted in Fig. IV.8d and f. The data is fitted with an approximated function of the magnetic field dependence of the superconducting energy gap [145],

$$E^{j\Delta} = K_{j\Delta}\Delta_0\sqrt{1-(B_c/B)^2}, \tag{IV.3}$$

where B_c is the critical field. The parameters obtained from the fits are $K^{On}_{2\Delta}/K^{On}_{\Delta} = K^{Off}_{2\Delta}/K^{Off}_{\Delta} = 2.02 \pm 0.025$, $K^{Off}_{2\Delta/3}/K^{Off}_{\Delta} = 0.55 \pm 0.07$. Therefore, the peaks indeed correspond to the quasiparticle transport and 1-st and 2-nd order multiple Andreev reflections.

The good agreement of the temperature and field dependences of the observed structures with the theory as well as the consistency between the $K_{j\Delta}$ coefficients and the critical temperature prove the Andreev reflection origin of the observed gap structures.

2.2 MAR at Fabry-Perot to Coulomb Blockade Transition

In this section we present studies of supercurrent transport and multiple Andreev reflections in a nanotube device showing both Fabry-Pérot interference (at more negative gate voltages) and fourfold shell filling (at more positive gate voltages). The measured device has a length of 300 nm and is fabricated from the superconducting Pd/Al bilayer with material thicknesses of 4 nm and 80 nm. At room temperature, the resistance of the device is around 50 kOhm at $V_G = 0$ V. At low temperatures,

the transport properties of the device are revealed by bias spectroscopy, where the differential resistance is measured as a function of the bias current and the gate voltage. The voltage drop on the device is separately measured allowing to study the transport in the voltage-bias picture.

A bias spectroscopy plot at 10 mK and zero magnetic field is shown in Fig. IV.9, where the differential resistance is plotted as a function of the bias current and gate voltage.

The observed regular transport pattern is consistent with a single quantum dot model of the nanotube. Near the zero-bias, fine transport features are observed, owing to the superconductivity of the contacts. A more familiar measurement diagram of the transport can be obtained when plotting the differential conductance as a function of the measured voltage drop on the nanotube and the gate voltage (Fig. IV.10). The oscillations of the conductance at $V_G \lesssim -6\,\mathrm{V}$ are due to the Fabry-Pérot interference of particles reflected back and forth. At $V_G \gtrsim -6\,\mathrm{V}$ the pattern turns into large diamonds followed by smeared conductance resonances. This is reminiscent of the four-fold shell structure of the nanotube energy band. A plot of the cross-section at the white dashed line in Fig. IV.10 is shown in Fig. IV.11a. It shows broad oscillation of the conductance at low gate voltages followed by clusters of four conductance peaks divided by large blockade valleys. The transition between the two regions is accompanied by an overall decrease of the conductance*. A clearer picture is observed when the contacts are turned normal by applying a perpendicular magnetic field of approximately 10 mT. The differential conductance in the observed two transport regions in the normal state is plotted in Fig. IV.11b and c, revealing the Fabry-Pérot and four-fold shell filling regimes. From

*The overall decrease of the conductance with the increasing gate may indicate that hole transport takes place in the measured gate voltage region. However, a semiconducting gap has not been observed in this region.

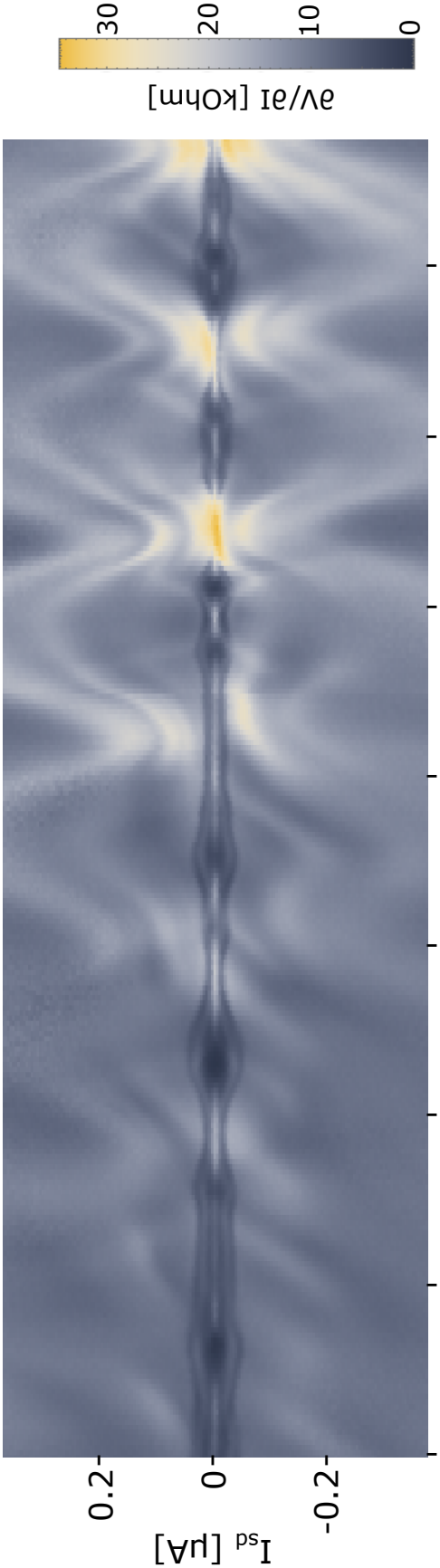


Figure IV.9: Current-biased measurement of the differential resistance of a nanotube device (DC-SN-2) showing a regular pattern. A superconducting proximity-induced transport can be seen in the vicinity of zero bias.

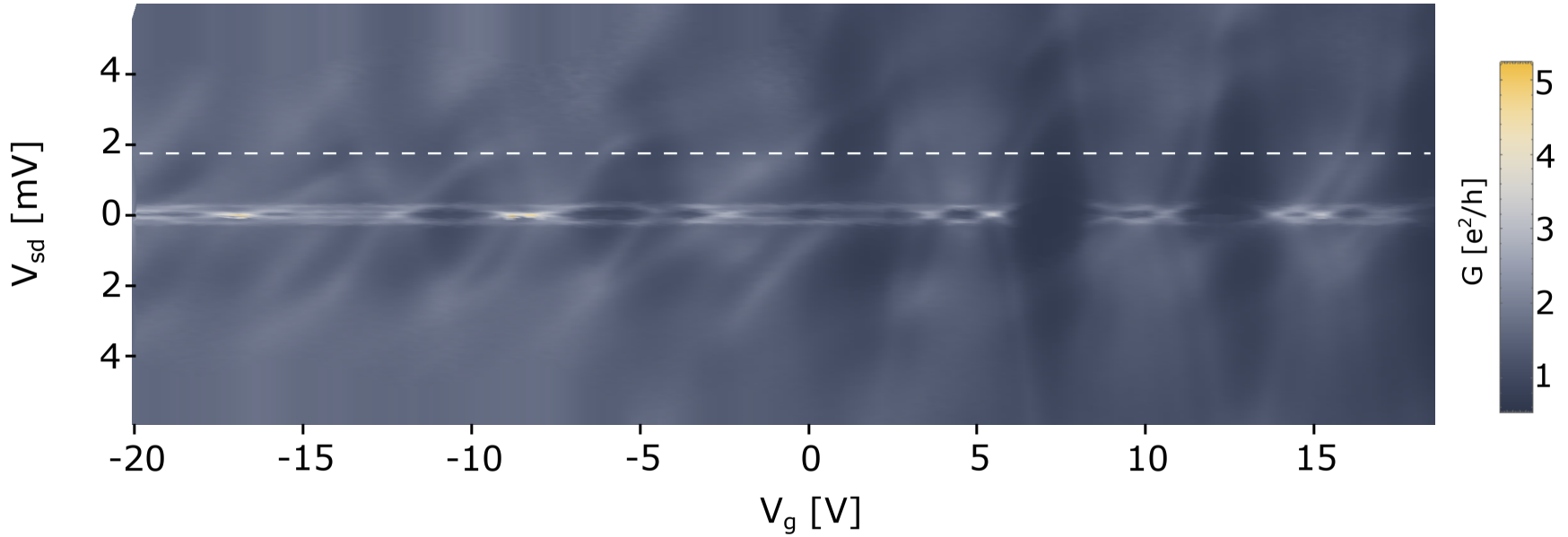


Figure IV.10: Voltage-biased measurement of DC-SN-2, where differential conductance is plotted as a function of the measured voltage drop and the gate voltage. At negative voltages Fabry-Pérot oscillations of the conductance are observed followed by a four-fold shell filling pattern.

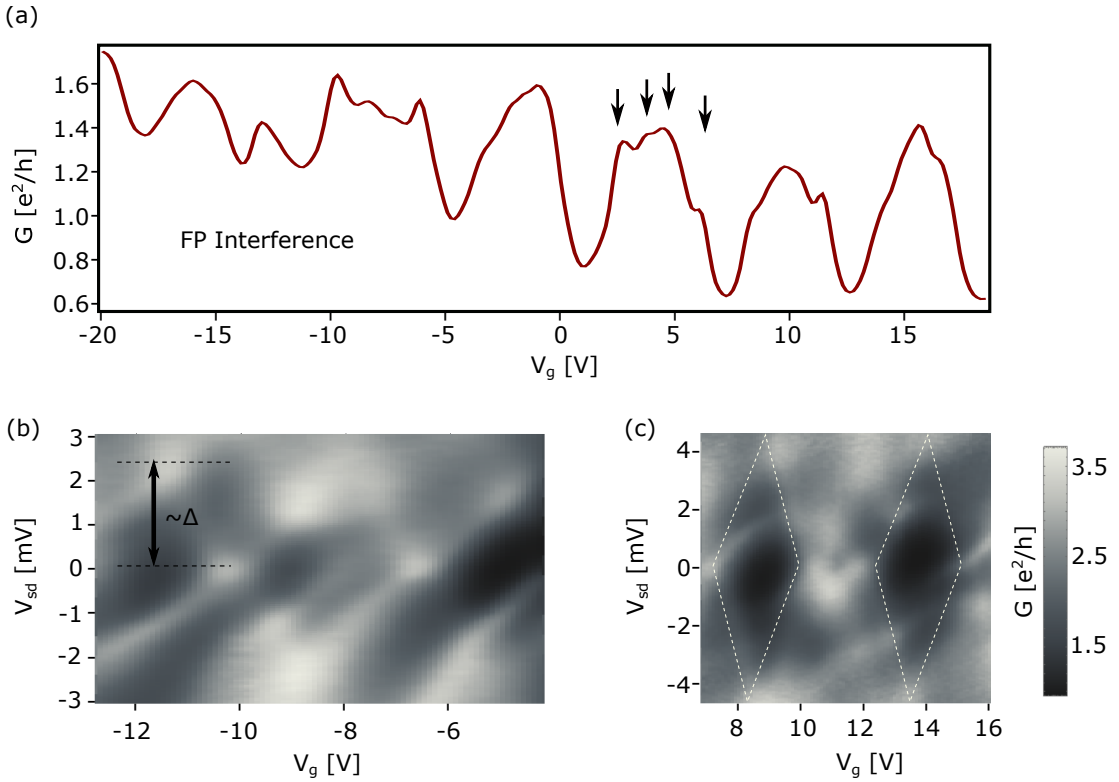


Figure IV.11: a. Differential conductance at $V_{sd} = 1.8\,\mathrm{mV}$ as a function of the gate voltage when a perpendicular field is applied to suppress superconductivity. Broad Fabry-Pérot oscillations are observed followed by four-fold shell filling pattern. b. Stability diagram in the Fabry-Pérot regime showing the typical checkerboard pattern. The distance between the conductance resonances is proportional to the quantum dot level spacing. c. Stability diagram at positive gate voltages. Four-fold degeneracy of the dot levels are revealed by a large diamond where transport is blocked, followed by four smaller conductance resonances, which are smeared due to the strong coupling to the leads.

the maximum value of the conductance at a Fabry-Pérot resonance $G_N^{max} = 3.3\,e^2/h$ the coupling asymmetry of the device to the leads can be estimated as $\Gamma_S/\Gamma_D \approx 0.4$.

The dot quantum levels are four-fold degenerate which is revealed in the lower conductance region. Signs of the Fabry-Pérot oscillations are still visible in this region, but now they are split into clusters of four smaller peaks (indicated by arrows in Fig. IV.11a) followed by large diamonds (see Fig. IV.11c). At lower conductance regime the particles are more localized on the quantum dot levels. The smaller peaks are therefore due to Coulomb blockade and single particle tunneling through the dot. The smearing of the diamonds is due to the large transparency

of the metal-nanotube interfaces and therefore strong coupling of the dot to the leads. In the spin-odd states of the four-fold degenerate structure Kondo effect shows a dominant role in the transport at zero bias voltage.

Now that the transport through the nanotube device is characterized, the superconductivity-related transport patterns can be analyzed in detail. Measurement of the differential resistance in the superconducting state at 10 mK and zero magnetic field is shown in Fig. IV.12a. The gate voltage range is the same as in Fig. IV.9. Similar to the device discussed in the previous section, supercurrent modulation with the gate voltage along with multiple Andreev reflection resonances are observed. In the Fabry-Pérot regime (the region $-13\,\mathrm{V} \lesssim V_G \lesssim -6\,\mathrm{V}$) the supercurrent transistor behaviour with successive 'On' and 'Off' states can be seen, as in the previous device (Section IV.2.1).

At positive gate values, however, the pattern is clustered into three successive 'On'-'Off'-'On' states followed by wide 'Off' states. This behaviour closely follows the normal state conductance behaviour in the four-fold shell filling region.

The transition between the two transport regions happens at around $V_G = -5\,\mathrm{V}$. The cross-sections at gate voltages in 'On' and 'Off' states in the two transport regions are shown in Fig. IV.12b. In the two states similar behaviour is observed as for the previous device in Section IV.2.1. Fig. IV.12c shows the V(I) characteristics of the device at different gate values. As the bias current increases a sudden jump to a finite resistance state is observed at a critical value of the applied current. Below this value, the resistance is expected to be zero theoretically. A small resistance observed in the measurement is due to the finite accuracy of the calibration of the 2-point measurement. The observed critical value of the current is tuned with the gate voltage as shown in the figure.

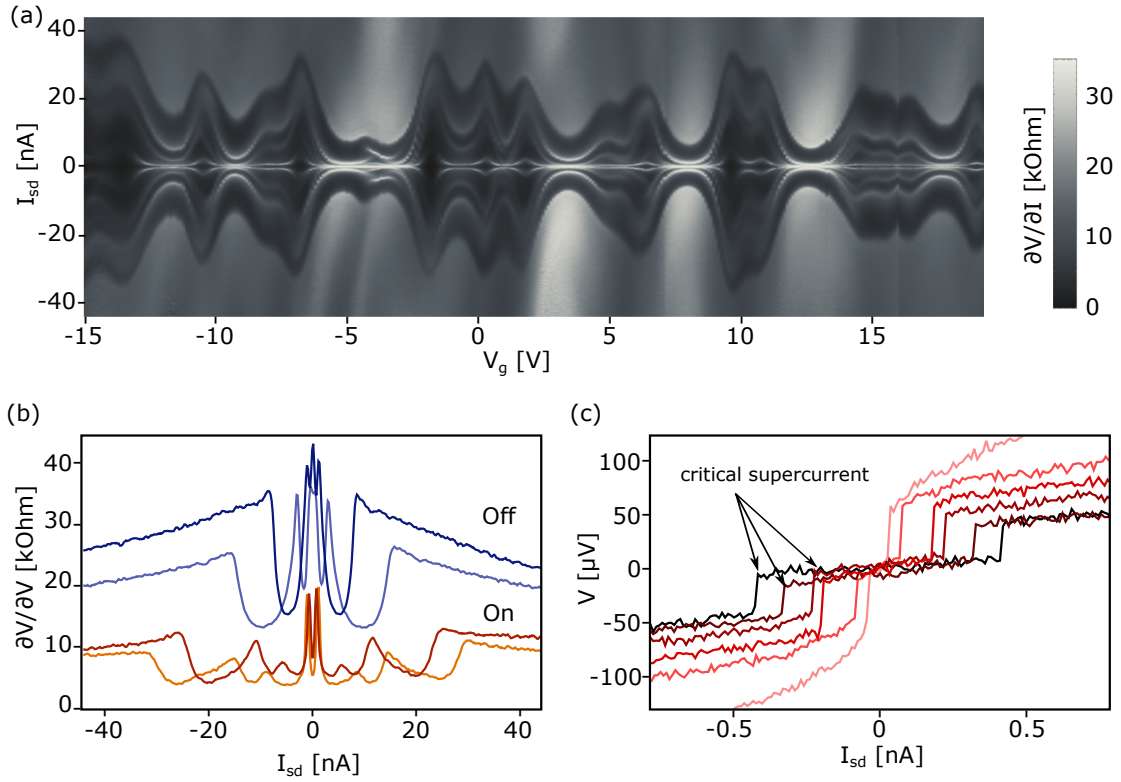


Figure IV.12: a. Stability diagram at low current bias when the magnetic field is off. MAR peaks are observed along with a dark supercurrent region near zero-bias current. 'On' and 'Off' states of the supercurrent follow the normal state conductance oscillations. b. Cross-sections of a at gate values in 'On' and 'Off' states in Fabry-Pérot and four-fold shell filling regions. The 'Off' state curves are shifted upwards by 10 kOhm for clarity. c. V(I) characteristics of the device at different gate voltages. The critical value of the supercurrent, at which a sudden transition to a finite resistance state is observed, is tuned with the gate voltage. A small residual resistance below the critical current is due to a finite calibration accuracy of the measurement.

The proximity-induced supercurrent transport as well as the multiple Andreev reflection can be further characterized in a voltage-biased picture (Fig. IV.13a). As before, the MAR peaks are observed as horizontal resonances at bias voltages $2\Delta/ne$, where n is an integer and Δ is estimated to be around 125 μeV. The measurements of the differential conductance in the 'On' and 'Off' states are illustrated in Fig. IV.13b showing a similar behaviour to the device discussed in Section IV.2.1.

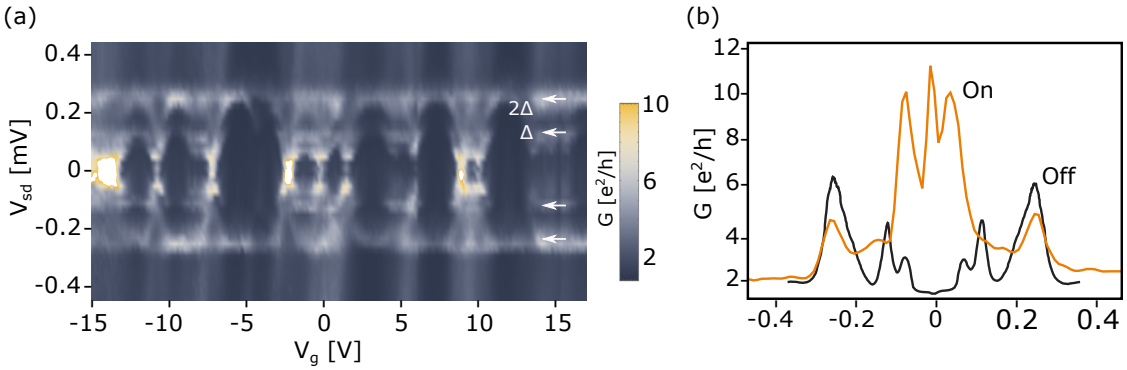


Figure IV.13: a. Differential resistance as a function of the measured voltage drop and applied gate voltage. MAR transport is now seen as horizontal, nearly gate-independent resonances at voltages $2\Delta/ne$. In the 'On' states, a zero-bias peak is observed corresponding to the supercurrent transport. Maximum conductance of the zero-bias peak reaches $30\,e^2/h$. b. Cross-sections of a at gate voltages in 'On' and 'Off' states.

2.2.1 Correlation Between Critical Supercurrent and Normal State Conductance

We now turn to a more quantitative description of the supercurrent and in particular its correlation with the normal state conductance. For short junctions in diffusive systems and ideal NS contact interfaces it has been found that $I_c/G_N \propto \Delta_g/e$, where I_c is the critical value of the supercurrent and G_N is the normal state conductance at zero bias [130]. This situation changes when a single conductance channel with conductance given by Eqn. II.7 connects the two superconducting leads. The lineshape of the critical current in such systems (more specifically for a quantum dot connected to superconducting leads) has been studied by Beenakker and van Houten [43]. The theory has been further extended to a more general case including the finite length effects by Galaktinov and Zaikin [146]. In the limit where the quantum level width is much larger than the superconducting gap ($h\Gamma >> \Delta_g$), it has been found that the critical supercurrent is

$$I_c = 2\frac{e\Delta_g}{\hbar}\left(1-\sqrt{1-T_{BW}}\right), \tag{IV.4}$$

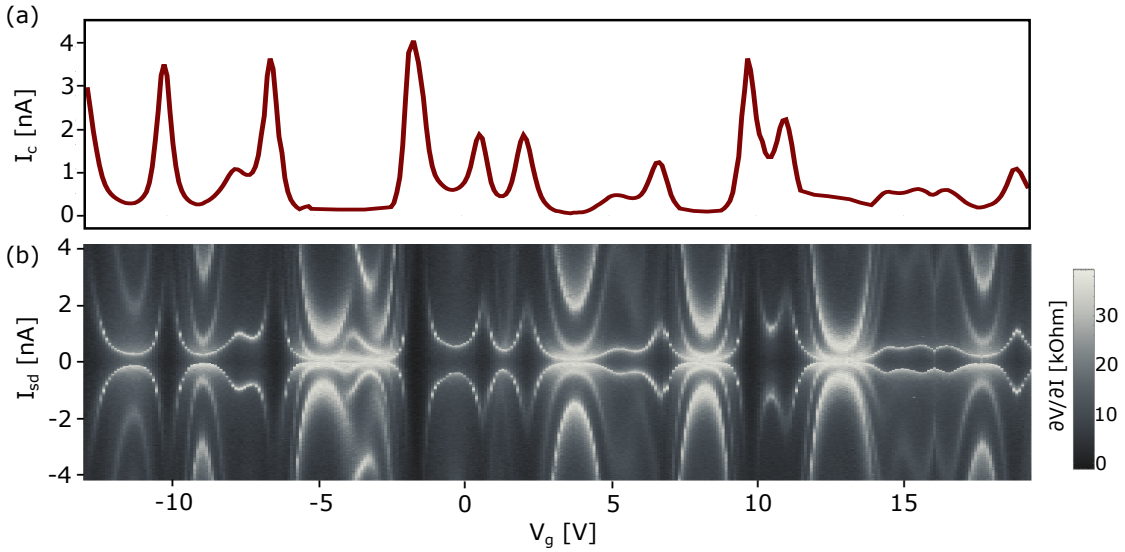


Figure IV.14: a. Gate-dependence of the critical value of supercurrent showing successive peaks corresponding to the 'On' states and suppressed regions corresponding to 'Off' states. b. A zoomed-in current biased measurement of the supercurrent region and MAR resonances. The 'On' and 'Off' states of the supercurrent transistor are clearly observed when tuning the gate voltage.

where $T_{BW} = \Gamma_S\Gamma_D/((\epsilon/\hbar)^2 + \Gamma^2/4)$ is the Breit-Wigner transmission probability (see Eqn. II.7).

In carbon nanotubes the correlation between I_c and G_N has been previously studied by P. Jarillo-Herrero in [33]. To study this correlation in the present device, a fine measurement of the supercurrent flowing through the nanotube is done. The critical value of the supercurrent as a function of the gate voltage is plotted in Fig. IV.14a. It is obtained from the maximum of the black region near zero bias in the differential resistance measurement shown in Fig. IV.14b. The supercurrent data can be fitted to the above described theoretical model. A finer measurement of the first supercurrent peak in Fig. IV.14a is shown in Fig. IV.15a. To fit the data we use the estimated value of the lead-coupling asymmetry, $\Gamma_S/\Gamma_D \approx 0.4$.

The supercurrent peak is fitted to the following function:

$$I_c = I_0(1 - \sqrt{1 - \frac{\Gamma_S\Gamma_D}{(V_G - V_G^R)^2 + \Gamma^2/4}}). \tag{IV.5}$$

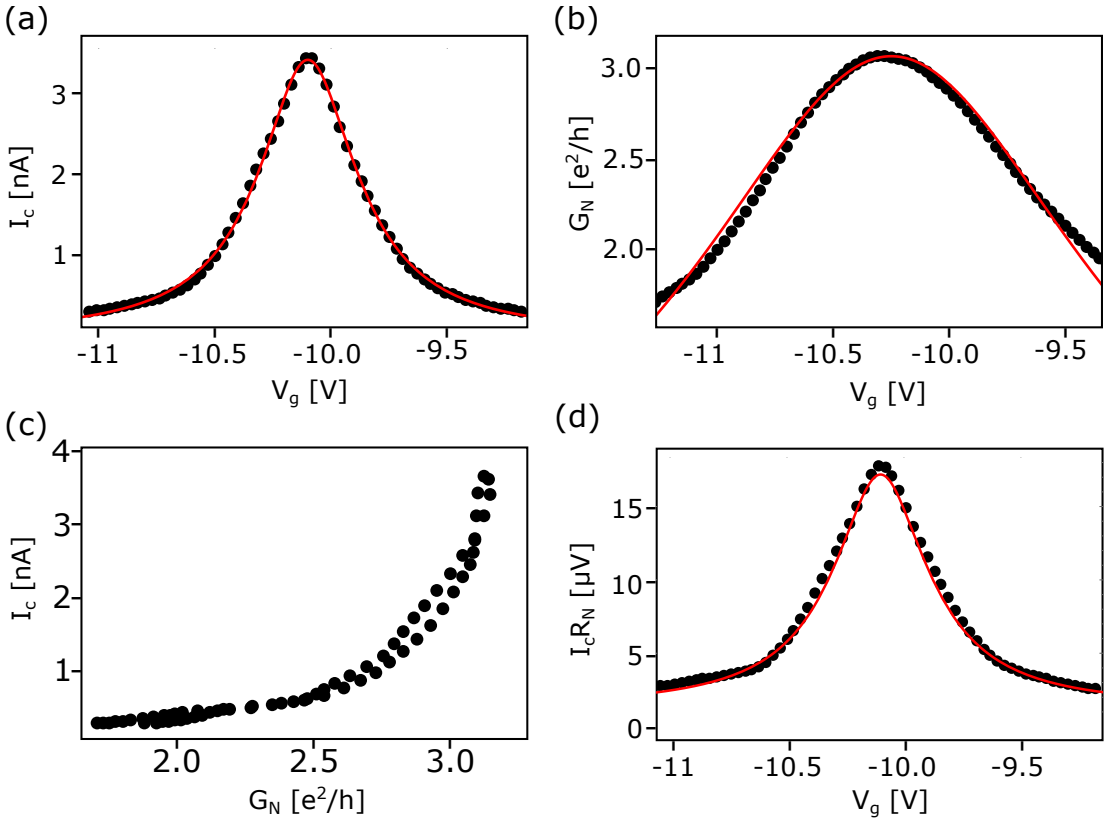


Figure IV.15: a. Gate dependence of a supercurrent peak fitted with Eqn. IV.5 showing good qualitative agreement with the theoretical model. The maximum value of the supercurrent obtained from the fit is much smaller than predicted in the model due to coupling to the external electromagnetic environment. b. Gate dependence of the normal state conductance peak fitted with Eqn. II.7. c. Correlation between the critical supercurrent and the normal state conductance showing a fast decrease of the measured I_c with decreasing G_N. An ideal SNS junction, with N a normal metal with continuous density of states, would exhibit a linear correlation curve. d. I_cR_N product as a function of the gate voltage obtained by dividing the data and theoretical curves in a and b. The lineshape of the supercurrent peak implies a resonance shape of the I_cR_N product observed in the data.

The maximum value of the critical supercurrent obtained from the fit is $I_0 = 6.1\,\mathrm{nA}$. This is smaller than the expected theoretical value of $I_0^m \approx 33.6\,\mathrm{nA}$ estimated taking into account the lead-coupling asymmetry. A similar reduction of I_0 compared to its theoretical value has been observed in [33, 147].

To understand the suppression of the supercurrent, nanotube device is described by an extended resistively and capacitively shunted Josephson junction (RCSJ)

model [33]. The circuit representing the sample consists of an ideal Josephson junction with a current phase relation $I_J(\phi)$ in parallel to the junction resistor R_J and capacitor C_J (Fig. IV.16). The extended RCSJ model also includes the contribution of the environment, represented by a parallel capacitor C and a series resistor R. Assuming a sinusoidal current-phase relation ($I_J(\phi) = I_0 sin\phi$), the dynamics of ϕ becomes equivalent to that of a motion of a particle in a tilted washboard potential. An important parameter characterizing whether the Josephson junction is overdamped or underdamped is its quality factor. It is defined in the extended RCSJ model as [33]

$$Q = \frac{1}{\omega_p[RC + \frac{\hbar}{2e}\frac{1}{I_0 R_J}]}, \quad \omega_p = \sqrt{\frac{2eI_0}{\hbar[C(1 + R/R_J) + C_J]}}, \tag{IV.6}$$

where ω_p is the plasma frequency. For the present device, the junction capacitance is $C_j \approx 400\,\mathrm{fF}$ estimated from the charging energy. $R_j \geq 5\,\mathrm{kOhm}$ represents the dissipation due to the quasiparticles, estimated by the differential resistance at the switching current. The capacitance C is mainly determined by the capacitance between the bond pads, estimated to be in a few pF range. Resistance R of the gold bond pads is estimated to be in a few Ohm range. Using these values we find $Q \approx 20$, corresponding to an underdamped junction. In this case a small fluctuation causes the particle in the washboard potential to go into a 'runaway' state, resulting in a critical current much smaller than the true I_0, as observed in our experiment.

The conductance peak in the same gate voltage range as in Fig. IV.15a in the normal state (Fig. IV.15b) is fitted with the equation

$$G_N = 4\frac{e^2}{h}\frac{\Gamma_S\Gamma_D}{(V_G - V_G^R)^2 + \Gamma^2/4} \tag{IV.7}$$

Fig. IV.15c shows the correlation between the critical supercurrent and the normal state conductance. For an ideal diffusive SNS junction a linear correlation

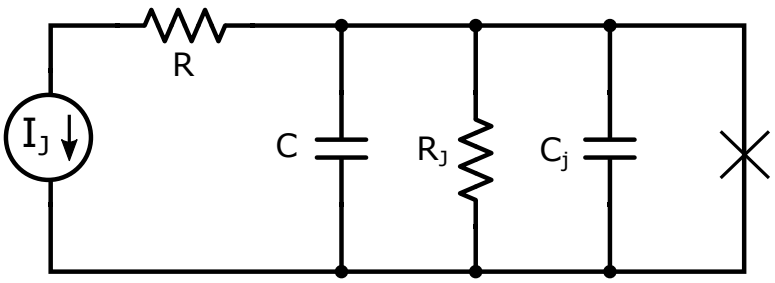


Figure IV.16: The equivalent circuit of the nanotube device in the extended RCSJ model. The nanotube junction is represented by an ideal Josephson junction in parallel with the junction capacitor C_J and resistor R_J. It is coupled to the environment represented by the parallel capacitor C and series resistor R.

function is expected. Instead, in this case the decrease of the supercurrent with the normal state conductance is much faster. Due to the lineshape of the critical supercurrent, the I_cR_N product has a resonance at the maximum value of I_c as shown in Fig. IV.15d. The data and the theoretical fit are obtained by dividing the data and equations for I_c and G_N.

2.2.2 Magnetic field Dependence

To further characterize the observed superconductivity-related transport features their magnetic field dependence is studied. This is shown in Fig. IV.17 for three different gate cross-sections. In the 'On' state at $V_g = 10.6\,\mathrm{V}$ in Fig. IV.17b, a zero-bias supercurrent peak can be seen along with vaguely observed multiple Andreev reflection peaks. In the 'Off' states plotted in Fig. IV.17c,e the MAR features are well resolved. The two cross-sections are measured in Fabry-Pérot and fourfold shell filling regimes at gate voltages $V_G = -9.4\,\mathrm{V}$ and $V_G = 17.3\,\mathrm{V}$ correspondingly (see Fig. IV.12a). In these states, as expected, the supercurrent peak is suppressed. As before the positions of the peaks versus the applied field are fitted with Eqn. IV.3 yielding $\Delta_g = 125\,\mu\mathrm{eV}$ which agrees with the value obtained for the device discussed in Section IV.2.1. The values of the coefficients $K_{j\Delta}$ obtained from the fits correspond to the expected values for the quasiparticle

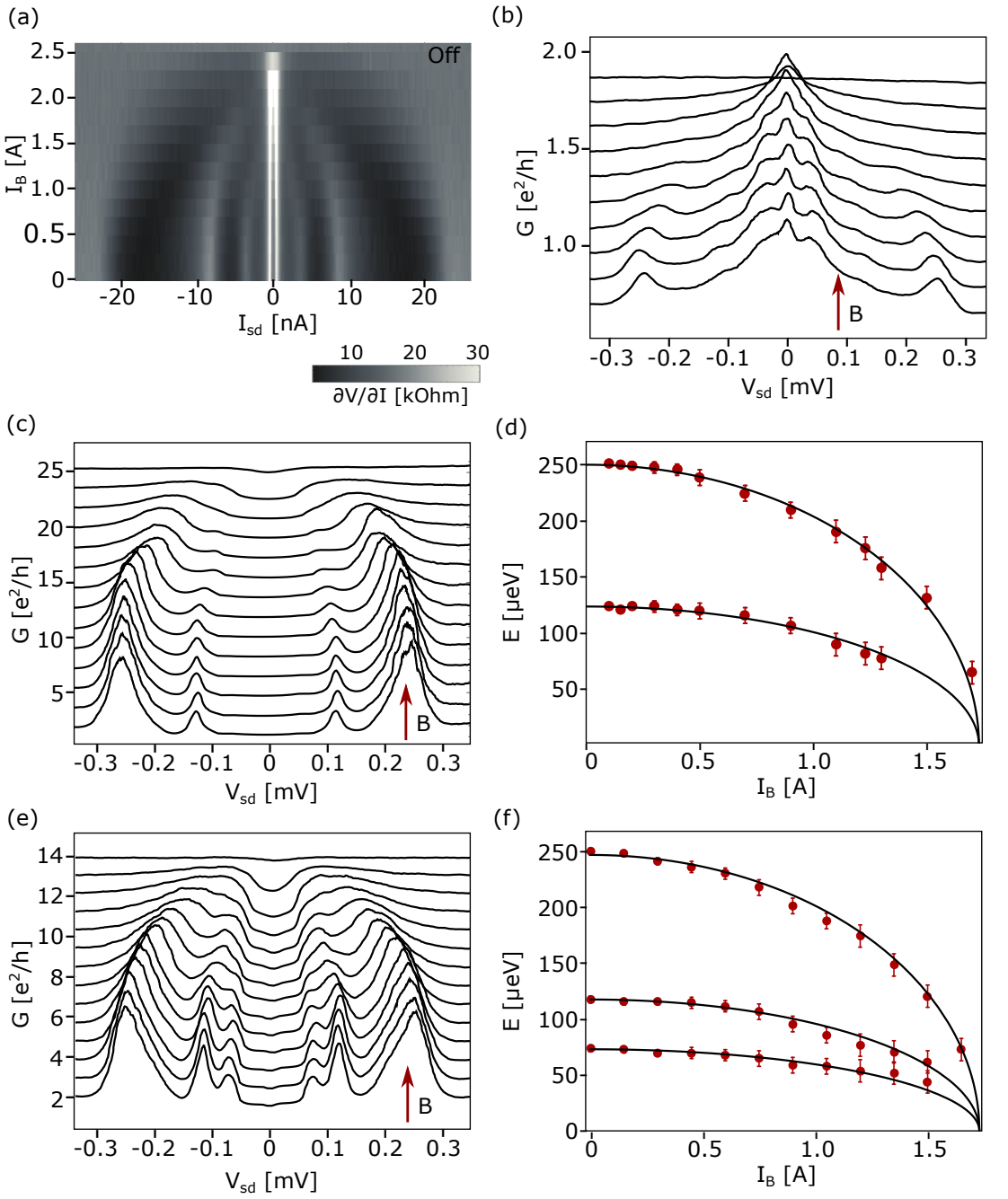


Figure IV.17: a. The magnetic field dependence of a sub-gap structure in a current-biased measurement. b. Voltage-biased curve in the 'On' state showing smeared MAR peaks and a zero-bias supercurrent peak. c,e. Field dependence of the differential conductance as a function of the measured voltage drop in 'Off' state correspondingly in the Fabry-Pérot and single particle-tunneling regimes. The quasiparticle transport and first and second order MAR peaks are clearly observed with decreasing energies and amplitudes with the field in both regions. d. The data and theoretical fits of the observed peak energies versus the applied field yielding $\Delta = 125\,\mu$eV. Expected values for $K_{j\Delta}$ coefficients are obtained from the fits.

transport and 1-st and 2-nd order multiple Andreev reflection peaks. Note that the superconductor-contacted devices described until now, although being fabricated on different samples, show consistent results for the superconducting gap and the critical field and temperature values. This indicates that we have good control over our fabrication of the 4/80 nm Pd/Al bilayer, whose critical field and temperature are sensitive to the film quality and thicknesses (further discussed in Chapter V).

2.2.3 Subgap Structure at the Transition Region

Here we discuss a gate region at the transition between the Fabry-Pérot and the single-particle transport ($-7V \lesssim V_G \lesssim -2V$) showing a rich structure in the current-biased measurement (Fig. IV.12a). A fine measurement of the differential resistance in this region is shown in Fig. IV.18a. The supercurrent is strongly suppressed and a number of clear gate dependent peaks in differential resistance are observed at low bias current inside the transition region, extending to higher bias current outside the region. As discussed in the previous sections, these peaks are due to multiple Andreev reflections. Around $V_G = -4\,\mathrm{V}$, peaks extending from the left disappear and new peaks appear at higher bias (see also Fig. IV.14).

In an effort to understand the observed sub-gap features, we study these in the voltage-biased picture. Fig. IV.18b shows a large bias measurement of the differential conductance at the transition region as a function of the measured voltage drop when tuning the gate voltage. A large Coulomb diamond can be observed with smeared edges indicating strong coupling of the nanotube to the leads. An additional conductance feature is observed inside the diamond which crosses the zero bias at around $V_G = 4\,\mathrm{V}$ (outlined with a red dashed line). This feature can be a reminiscent of the Fabry-Pérot transport at lower gate voltages. A fine measurement of the sub-gap structure at the transition region is shown in

Fig. IV.18c. One can observe horizontal resonances at bias voltages of $\pm 250\,\mu$eV, which mark the onset of direct quasiparticle tunneling between source and drain electrodes. The peaks due to the quasiparticle transport are clearly seen in the cross-sections at two different gate voltages shown in Fig. IV.18d. In Fig. IV.18e the gate evolution of the sub-gap structure at the intersection between the red dashed resonance in Fig. IV.18b and the gap region is shown. Besides the quasiparticle transport peaks, smaller peaks at lower bias are observed (indicated with a black arrow). These peaks can be due to 1st order MAR processes. They show a weak variation with the gate voltage. Such gate-dependence of the MAR processes has been previously reported and is believed to be related to the shift of the level position of the single-electron states with V_G [32, 148].

A more clear measurement of the normal-state conductance is necessary to understand the origin of the additional conductance resonance in the diamond in Fig. IV.18b and the gate-dependence of the sub-gap structure at this resonance.

2.3 Interplay of Four-fold Degeneracy and Multiple Andreev Reflections in a Carbon Nanotube Quantum Dot

In this section we discuss additional measurements of the interplay of the nanotube four-fold degenerate shell structure and the MAR. The device length is 300 nm and the same Pd/Al bilayer is used to contact the nanotube (device DC-SN-3 in Appendix B). Fig. IV.19a shows a measurement of the differential conductance in the normal state of the contacts when changing the applied gate voltage. The superconductivity of the contacts is suppressed by applying a perpendicular magnetic field. The clusters of four conductance peaks followed by a large dip are a result of a Coulomb blockade and the four-fold degeneracy of the nanotube energy band as explained in Section II.1.2.6. The slight increase of the conductance value with the

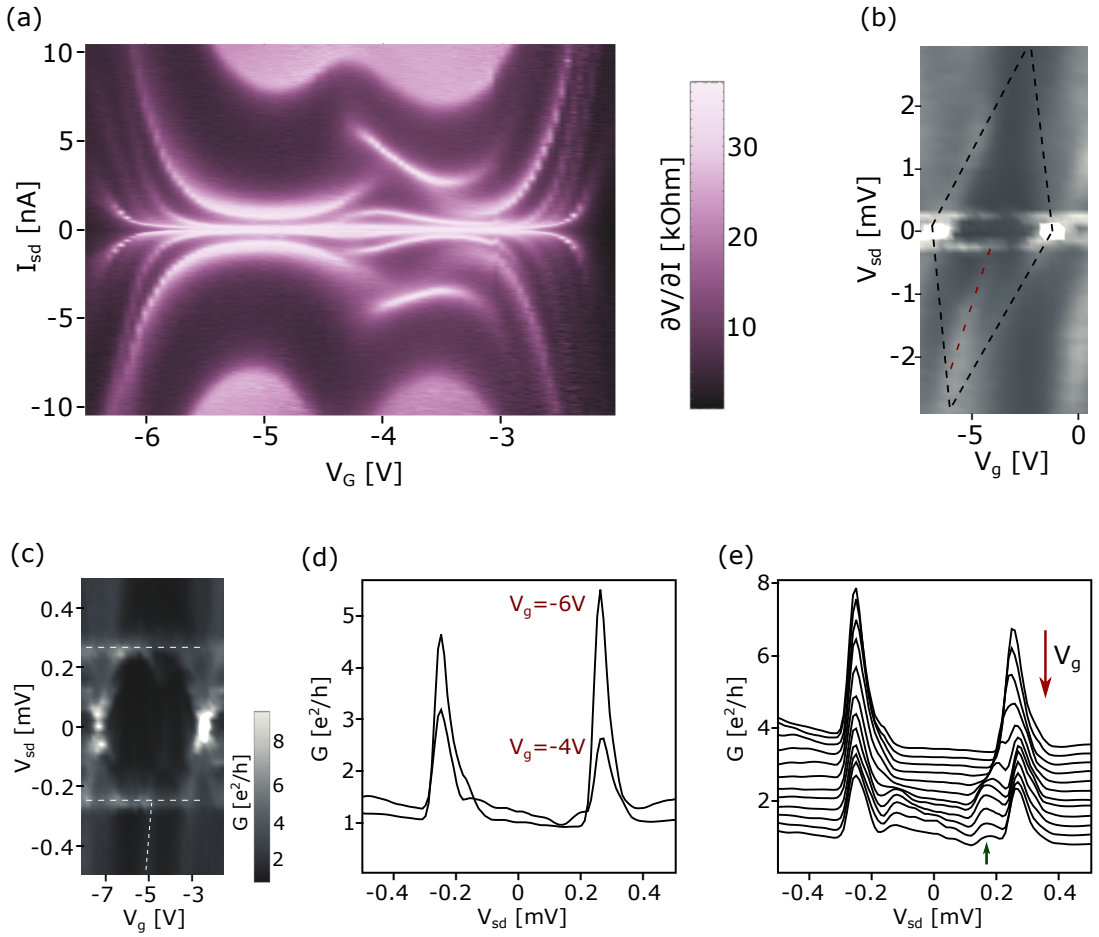


Figure IV.18: a. High resolution current-biased measurement of the transition between Fabry-Pérot and single particle filling transport regions. b. Large voltage-biased measurement of the differential conductance. A Coulomb diamond is observed at the transition region. An additional conductance resonance can be seen inside the diamond. c. A detailed lower bias measurement of the gap region. Quasiparticle transport peaks appear at $2\Delta/e$. The additional resonance line is outlined with a white dashed line. d. Gate cross-sections before and after the intersection point of the additional resonance with the gap region. 2Δ peaks are observed. e. The cross-sections at the transition through the intersection point.

gate indicates that in this region an electron-transport takes place. When tuning the bias voltage across the nanotube, the conductance peaks evolve to form sets of a large diamond followed by three smaller diamonds as shown in Fig. IV.19b. In the normal state, the maximum conductance in the measured gate region is $G_{max} = 2.1\, e^2/h$, and therefore the nanotube states are strongly coupled to the leads. This results in the smearing of the transport features.

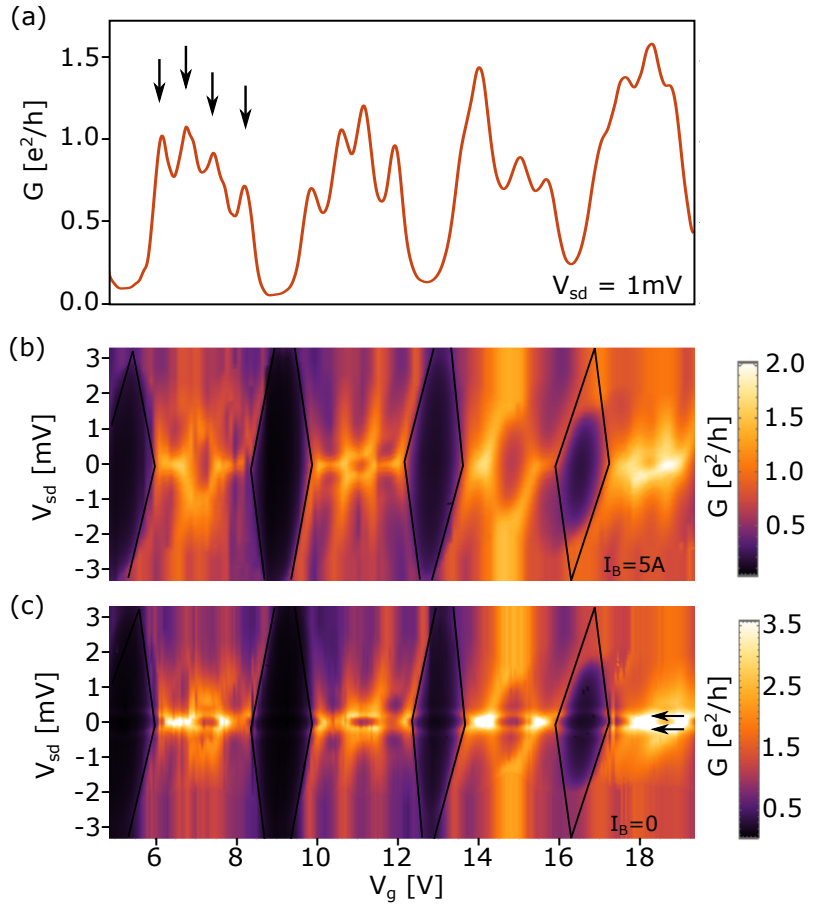


Figure IV.19: a. Normal state differential conductance of DC-SN-3 nanotube device at $V_{sd} = 1\,\mathrm{mV}$ when a magnetic field is applied to suppress superconductivity of the leads. Clusters of four small conductance peaks are observed followed by a large blockade valleys revealing the single electron filling of the four-fold degenerate quantum dot energy levels. b. Stability diagram in the normal state when a large magnetic field is applied perpendicular to the sample. Large blockade diamonds are observed followed by smaller smeared diamonds. In the spin-odd states Kondo effect results in zero-bias transport peaks. c. Stability diagram when the magnetic field is turned off. Additional transport features are observed at low bias voltage due to the superconductivity of the leads.

When the magnetic field is turned off the contacts become superconducting. In this case additional transport features are observed in the differential conductance measurement shown in Fig. IV.19c. In particular, one can observe the appearance of new features at low bias voltages ($V_{SD} \lesssim 0.5\,\mathrm{mV}$). At higher bias voltage, the transport features are near identical to those in the normal state of the contacts. The increase in the maximum value of the conductance ($G^{SC}_{max} = 3.6\,e^2/h$) owes to the superconducting proximity effect. The slight distortion of the results at

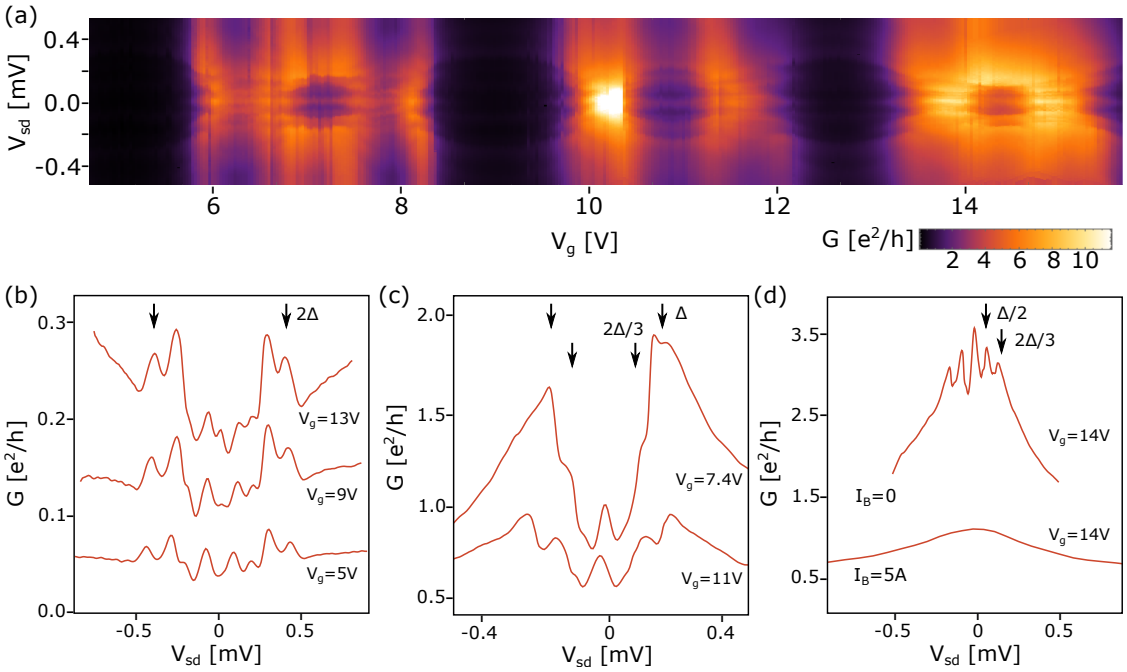


Figure IV.20: a. A finer measurement of the transport features near zero-bias that are due to the superconductivity of the leads. b. Cross-sections at gate voltages in the three large diamonds showing multiple orders of MAR peaks. b. Cross-sections at spin-even states showing the quasiparticle tunneling peaks and 1st order MAR peaks. A zero-bias peak is observed owing to supercurrent transport. d. Cross-section at a spin-odd state when the current through the magnet is $I_B = 0$ and $I_B = 5\,\mathrm{A}$. In the normal state a broad Kondo peak is observed. In the superconducting state additional smaller peaks appear on top of the Kondo peak and the overall conductance is largely enhanced.

high bias voltages is due to the numerical correction of the data where the circuit resistances other than the device are subtracted.

Fig. IV.20a shows a finer measurement of the observed low bias structure. We recall that the conductance peaks due to the Andreev reflections appear at bias voltages $2\Delta/ne$, where Δ is the superconducting gap.

In the large diamonds the net spin of the quantum dot is even. Fig. IV.19b shows the cross-sections at the centers of the large diamonds. Here the sub-gap structure consists of the 2Δ conductance peaks, shown with black arrows, indicating the onset of the quasiparticle transport. The gap energy can be estimated from the positions of the 2Δ peaks to be about $200\,\mu$eV at 10 mK. One can also clearly identify 1st, 2nd and even higher orders of multiple Andreev reflection peaks.

In the three smaller diamonds the quantum dot has correspondingly odd, even and odd net spin. In the even-valley the SGS slightly resembles the one in the larger diamonds with visible Δ and $2\Delta/3$ peaks. However, unlike the sub-gap structures in Fig. IV.19b, here also a small zero-bias peak exists. This has been previously interpreted as being a result of a proximity-induced supercurrent due to Andreev bound states [50].

In the 1st and 3rd of the smaller diamonds a Kondo effect is observed as shown in Fig. IV.19b due to the net odd spin. The sub-gap structure here is different from the first two cases. Fig. IV.19c shows the plots at a particular odd-valley in the normal and superconducting states of the leads. The normal state curve shows a typical Kondo peak with a maximum conductance of $1\,e^2/h$. When the leads are superconducting, this peak is enhanced to $3.5\,e^2/h$. In addition to this, conductance peaks appear on top of the Kondo peak, which decays fast beyond the gap energy. These peaks appear at voltages $\pm 2\Delta/3$ and $\pm 2\Delta/4$ and are believed to be due to 2nd and 3rd order MAR processes. In addition, in the Kondo valley a comparably larger zero-bias peak exists possibly due to the proximity-induced supercurrent transport.

When comparing the sub-gap structures in Coulomb and Kondo valleys, one can thus see, that in the Coulomb valleys, where the conductance on average (otherwise the effective transparency of the S-CNT-S channel) is smaller, large 2Δ peaks are observed and the zero-bias peak is suppressed. On the other hand, in Kondo valleys, where the conductance is larger, a large zero-bias peak is observed and the 2Δ peaks are suppressed. Such behaviour has been observed previously in nanotube devices [31, 32].

The critical temperature of the bilayer calculated from the gap energy is $T_c = 1.3\,\mathrm{K}$. Compared to the superconductor-contacted nanotube devices discussed in the previous sections, the obtained value for the critical temperature is very high. It is

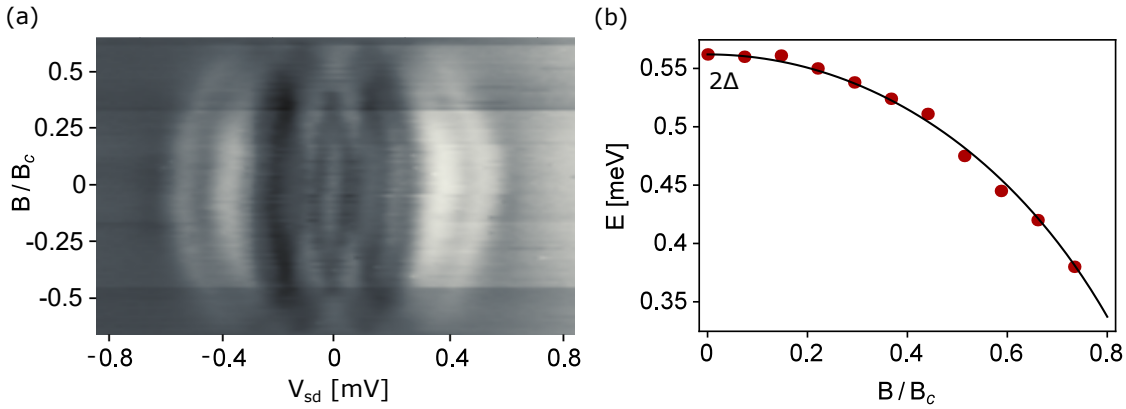


Figure IV.21: a. Magnetic field dependence of the differential conductance as a function of the bias voltage. The MAR peak positions and amplitudes decrease due to the suppression of the gap. b. Position of the 2Δ peaks as a function of the field normalized to the fitted critical field B_c. Data is fitted using Eqn. IV.3, yielding $\Delta \approx 230\,\mu$eV.

closer to the bulk Al critical temperature, which means that the nanotube is either covered by a Pd layer with a thickness much lower than the evaporated thickness of 4 nm or otherwise the Pd layer is not uniform. This can be a result of a non-zero angle of the sample with respect to the evaporator source or contaminations of the Al or Pd sources. At the same time the critical field necessary to turn the contacts normal is measured to be twice as high as for the rest of the measured samples, which is consistent with the estimated value of the T_c.

A further proof of the Andreev reflection origin of the observed subgap structures is achieved by performing magnetic field dependent measurements. A cross-section of the differential conductance inside a large diamond is plotted in Fig. IV.21a as a function of the normalized magnetic field. When increasing the absolute value of the magnetic field, the bias voltages at which the peaks appear as well as their amplitudes decrease. To estimate the superconducting gap, the energy of the quasiparticle tunneling peaks at 2Δ is fitted using Eqn. IV.3. Fig. IV.21b shows the data and the fitted curve as a function of the field normalized to the fitted critical field. We cannot state the field quantitatively as the sample is not

placed inside the magnet bore. The fitting yields $\Delta \approx 225\,\mu$eV.

2.4 Discussion and Conclusion

In conclusion, the DC transport measurements of superconducting and normal metal contacted nanotubes have been discussed in detail. In both our superconducting and normal metal contacted nanotube devices Pd is the metal directly contacting the nanotube. We have consistently observed to have very high transparencies and conductance values are measured nearly equal to the quantum limit of $4e^2/h$ for a single link with two conduction channels. In the superconducting metal contacted nanotubes, additional Al layer was used with a thickness much larger than the Pd layer thickness. In these devices, the superconducting proximity effect resuts in obtaining high transparency superconducting contacts to the nanotubes. The measured values of the superconducting gap energy $\Delta \approx 125\,\mu$eV and the critical temperature $T \approx 900$mK are reduced compared to the values of the bulk Al. This is due to the existence of the normal Pd layer in the bilayer and the values are in agreement with those found from microwave measurements reported in the next chapter.

Different transport regimes in normal metal contacted nanotubes have been investigated in detail in the beginning of the chapter. Depending on the particle tunneling barrier heights at the metal-nanotube interfaces, Coulomb blockade, Kondo effect and Fabry-Pérot interference transport characteristics have been observed in different devices. In each case, characteristics of the measured nanotubes are extracted using the theoretical models discussed in Chapter II.

The observed quantum transport characteristics can be compared to those in other systems, such as graphene, semiconducting nanowires and atomic contacts. Unlike single-walled nanotubes, in all of these structures the weak link connecting

the source and drain leads has a large number of conduction channels. Due to this, it is harder to understand and characterize the quantum transport (e.g. single-particle tunneling) in these systems.

The series of DC experiments on the normal metal contacted nanotube devices prove the good contact properties of Pd to the nanotubes. Additionally, they summarize the quantum transport properties of nanotubes. These experiments serve as a foundation not only for the DC transports of the superconducting metal contacted nanotube devices, but also the microwave probing of the quantum states in nanotubes discussed in Chapter VI.

In the second part of the chapter the superconducting metal contacted nanotubes have been investigated. When the contacts are superconducting, additional transport channels exist for the Cooper pairs. This is due to the Andreev reflection processes taking place at metal-nanotube interfaces. The interplay of the transport characteristics of Cooper pairs and normal quasiparticles has been measured in different transport regimes. In the Fabry-Pérot regime, superconducting transistor behaviour of the device has been measured. When tuning the gate voltage, the supercurrent follows subsequent 'On' and 'Off' states, where it is either strongly enhanced or suppressed in agreement with previously reported results [33]. This transistor behaviour is shown to be due to tuning the nanotube quantum levels on and off-resonance with the Fermi levels of the leads. Therefore the transport due to the superconducting nature of the leads follows the normal state conductance characteristics. In addition to the non-dissipative current observed at zero bias voltage, conductance peaks due to multiple Andreev reflection processes have been observed. These peaks appear at bias voltages $2\Delta/ne$, where Δ is the superconducting gap. In the measurements, up to third order multiple Andreev reflection processes have been clearly identified. The temperature and magnetic

field dependences of the sub-gap structures in both states of this supecurrent transistor have been studied. With the increase of both the temperature and the magnetic field, the energies of MAR peaks decrease and they disappear. This is a result of the suppression of the superconductivity of the leads when increasing T and B. The data agrees very well with the theoretical models for the gap energy dependences on the temperature and the field.

In a different sample, the proximity-induced transport has been studied in successive Fabry-Pérot and single particle filling regimes. The four-fold degeneracy of the nanotube quantum levels has been revealed in the singl particle filling transport. In the Fabry-Pérot regime the familiar suparcurrent transistor behaviour is observed, extending to clustered transistor states in the four-fold shell filling regime due to the four-fold degenerate structure of the quantum levels.

The correlation of the critical value of the supercurrent with the normal state conductance is studied. It shows a good qualitative agreement with the theoretical model for weak links contacting superconducting reservoirs. However, the experimentally estimated maximum value of the supercurrent is much smaller than expected from the model. Such reduction of the supercurrent has been observed before and is believed to be due to the coupling to the external electromagnetic environment, which is not taken into account in the model.

The magnetic field dependence of the MAR peaks and the supercurrent has been investigated in different supercurrent transistor states. The comparison to the theoretical model yields superconducting gap and critical field parameters consistent with the previous device. This proves that the Pd/Al bilayer is reliable.

The sub-gap structure is studied at the transition between Fabry-Pérot and single particle filling transport regimes. Additional peaks at voltages other than the expected MAR peak positions exist in this region. The normal state transport shows

conductance resonances resembling the excited state transport characteristics. The additional peaks may therefore be explained as being the quasiparticle tunneling through the excited states. Measurements of further similar devices, preferably with clearer normal state transport could help to clarify this.

In the final section the MAR features are measured in a device showing Coulomb blockade transport characteristics for four-fold degenerate quantum levels. The sub-gap structures in different spin-states are measured showing qualitatively different behaviours. Most importantly, in the Coulomb valleys large quasiparticle transport peaks are observed and the supercurrent peak at zero-bias is suppressed, whereas in the Kondo valleys, the quasiparticle peaks are suppressed and an enhanced supercurrent peak exists. This is attributed to an effectively large transparency of the conduction channel in Kondo valleys compared to the Coulomb valleys. Magnetic field dependence of the MAR features has been studied. Compared to the previous devices, the obtained gap energy and critical field values are much larger. This is believed to be due to a non-uniform covering of the nanotube with the Pd layer or the contaminations in Pd or Al sources.

With this, the measurements of the SN-bilayer contacted nanotubes are summarized. The observed proximity-induced transport features are well-characterized with the theoretical model of Andreev reflection transport. This creates a good foundation for studying the superconducting transport characteristics in a microwave circuit geometry.

The work reported in this chapter shows that we are able to fabricate consistently high transparency high transparency superconducting contacts to consistently good quality nanotubes. Therefore, we can expect to use the developed fabrication process to make Andreev bound state devices, such as carbon nanotube SQUIDs, where the ABS energies are tuned by a magnetic flux.

Moreover, one can think of a quantum bit in a circuit QED geometry based on the Andreev bound states existing in the high transmission nanotube channels. Compared to other systems, only one conduction channel exists in a single-walled carbon nanotube. It can carry only two Andreev bound state which can serve as quantum bit levels as suggested in [27, 119]. In this Andreev level qubit higher energy levels do not exist and therefore they do not cause decoherence and decay of the qubit.

V

Microwave Resonators for Proximity Effect Studies

Contents

1 Characterization of superconducting microwave LC resonators 118
1.1 Extracting Resonator Parameters From Temperature Dependence of Transmission 121
2 Measuring Proximity in Pd/Al Bilayers Using LC Resonators 125
2.1 Proximity Effect in SN Bilayers 125
2.2 Measuring LC resonator frequency response in a multiplexed geometry 126
2.3 Extracting LC resonator parameters from their temperature dependence 128
2.4 Study of the Critical Temperature of Pd/Al Bilayers . . 130
2.5 Discussion and Conclusion 133

In this chapter measurements of planar lumped element microwave resonators, fabricated from SN bilayers, are reported. The motivation for this is twofold. Firstly, lumped element resonators are promising candidates for high coupling strengths in circuit quantum electrodynamics geometries, where a carbon nanotube superconducting quantum interference device serves as a flux quantum bit. Moreover,

as discussed in this chapter, lumped element resonators serve as a reliable testbed for understanding the superconducting proximity-induced properties of the Pd/Al bilayers used for contacting the nanotubes.

This chapter presents measurements of lumped LC resonators. The results are well explained with the theoretical model presented in Section II.3.

1 Characterization of superconducting microwave LC resonators

In this section measurements of two-port LC resonators with a meander line inductor described in Section III.2.1 are presented. The geometries of the resonators are as shown in Fig. III.6a. The measurements of single resonators introduced here allow optimization of the device architecture to achieve desired resonance frequencies. In addition, they are useful in understanding the factors that influence the quality of the resonators.

The resonators presented in this section are made from Al (50 nm) and Ti (5 nm)/Al (50 nm) metallic layers. Low temperature measurements are done in a dilution fridge at 10 mK. The transmission through single LC resonators is measured with a vector network analyzer.

Measurement of the transmission S_{21} of an Al resonator is shown in Fig. V.1. The capacitor plate radius, the distance of capacitor plates and the inductor length are respectively $R_c = 175\,\mu$m, $d_C = 170\,\mu$m, $d_L = 2.53$ mm. The width of the meander line inductor is 400 nm. In the complex plane, the resonance represents a circle as explained in Section II.3.2 (Fig. V.1a).

Theoretically, the transmission of a two-port resonator can be obtained by

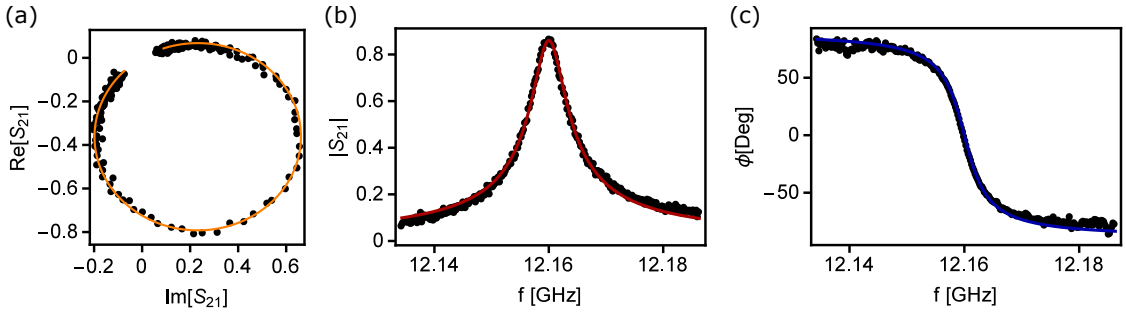


Figure V.1: a. Complex plane representation of the measured transmission through an LC resonator made of 50 nm Al layer. The solid line is obtained by fitting the data to Eqn. V.1. Parameters obtained from the fit are $f_0 = 12.16\,\mathrm{GHz}$, $Q_i = 1.5 \cdot 10^4$, $Q_e = 2400$. b. Linearized amplitude of the transmission showing the resonance. The solid line represents the amplitude of Eqn. V.1 with the parameters extracted from the fit in a. c. The phase data of the resonance. The solid line is obtained by substituting parameters extracted from the resonance fit in the argument of Eqn. V.1.

constructing its LCR representation (see Appendix A). It can be written as

$$S_{21}^{2port} = \frac{Q_i}{Q_e} \frac{1}{(1+\frac{Q_i}{Q_e})(1+2iQ_l\frac{\omega-\omega_0}{\omega_0})} e^{i\phi}, \tag{V.1}$$

where Q_l is the loaded quality factor of the resonator given by Eqn. II.34 and ω_0 is the resonance frequency. ϕ is a phase offset that accounts for an arbitrary initial phase. The orange curve in Fig. V.1a is obtained by fitting Eqn. V.1 to the complex data. The resonance parameters $f_0 = 12.16\,\mathrm{GHz}$, $Q_i = 1.5 \cdot 10^4$ and $Q_e = 2400$ are extracted from the fit.

Plotting the amplitude and phase of the complex response (Fig. V.1b and c) shows the more familiar Lorentzian response, with a peak at the resonant frequency.

Fig. V.2 shows results for a similar but smaller resonator made from the Ti(5 nm)/Al(50 nm) bilayer. The capacitor pad diameter and the inductor length are correspondingly $R_c = 135\,\mu\mathrm{m}$, $d_L = 1.8\,\mathrm{mm}$. All the other dimensions are the same as for the resonator in Fig. V.1. The smaller values of R_c and d_L result in a larger measured resonance frequency. The resonator parameters extracted from the fits are $f_0 = 15.34\,\mathrm{GHz}$, $Q_i = 1.05 \cdot 10^4$, $Q_e = 584$.

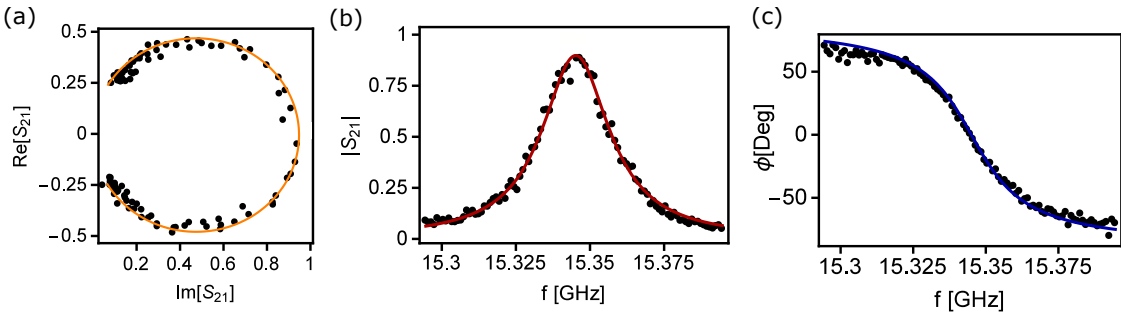


Figure V.2: a. Complex plane representation of the measured transmission through an LC resonator made of Ti (5 nm)/Al (50 nm) bilayer fitted with Eqn. V.1. Resonator parameters $f_0 = 15.34\,\text{GHz}$, $Q_i = 1.05 \cdot 10^4$, $Q_e = 584$ are extracted from the fitting. b. Linearized amplitude of the transmission showing the resonance and the corresponding theoretical curve given by the absolute value of S_{21} in Eqn. V.1 obtained using the parameters above. c. The phase data of the resonance and the corresponding theoretical curve given by the phase of S_{21} in Eqn. V.1.

As illustrated above, the dimensions of capacitors and inductors can be tuned to design resonators with desired resonance frequencies (Fig. V.3a). Amplitudes of transmissions of two resonators with different inductor lengths are plotted in Fig. V.3b and c. As the inductor length d_L decreases, L decreases, therefore increasing the resonance frequency from 12.11 GHz to 12.16 GHz. Similarly, the resonance frequency can be tuned by changing the capacitor pad diameter R_c, the distance between the capacitor pads d_c or the distance between the input and output ports and the capacitor pads d_p. In the proximity effect tests discussed in the next section, the frequencies are tuned by changing R_c and keeping all other dimensions constant.

As mentioned in Section III.2, chips carrying the LC resonators are attached to the copper sample holder with GE varnish. Resonators have been measured for different thicknesses of the insulating GE varnish layer. It is found that generally the internal quality factor increases for a thicker GE varnish layer. For example, when increasing the GE varnish thickness twice, Al resonator Q_i shows an increase from 1300 to 5800 and Ti/AL resonator Q_i shows an increase from 2500 to 3700.

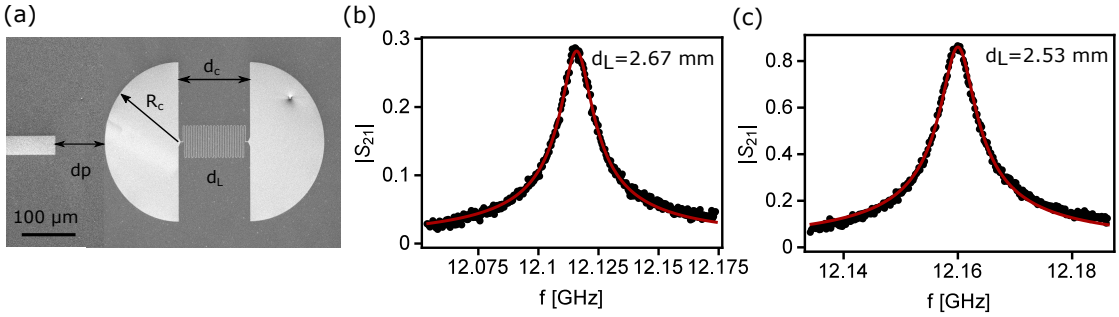


Figure V.3: a. SEM image of a two port resonator (the second port from the right is symmetrically positioned) showing the dimensions of the parameters. b,c. Amplitudes of S_{21} of Al (50 nm) resonators with different meander inductor lengths. When changing d_L from 2.67 mm to 2.53 mm the total inductance decreases and the resonance frequency increases from 12.11 GHz to 12.16 GHz.

This may be explained by a decreased microwave loss through the Si substrate and the metallic sample holder, when the substrate is better isolated from the holder.

The resonators discussed above are undercoupled, as in both cases $Q_e < Q_i$. The quality factor of an undercoupled resonator strongly depends on the applied power. Fig. V.4 shows the power dependence of a resonator transmission in the logarithmic scale. Above -70 dBm the linearized transmission spectrum at the resonance loses its Lorenzian shape and becomes nonlinear [149]. The non-linear behaviour of the resonance is modeled by the equation of motion of a Duffing oscillator [123]. At low powers, the dielectric losses in the resonator strongly depend on the photon number in it and therefore the quality factor can be reduced [150, 151]. The transmission spectra of the resonators measured in this thesis are taken at the highest power that corresponds to the linear regime to account for both of the above described effects.

1.1 Extracting Resonator Parameters From Temperature Dependence of Transmission

To extract the characteristic parameters of the resonators, such as the total capacitance C, as well as the metallic layers, such as T_c and the penetration depth $\lambda(0)$ in Eqn. II.42-II.44, temperature dependences of the transmission spectra

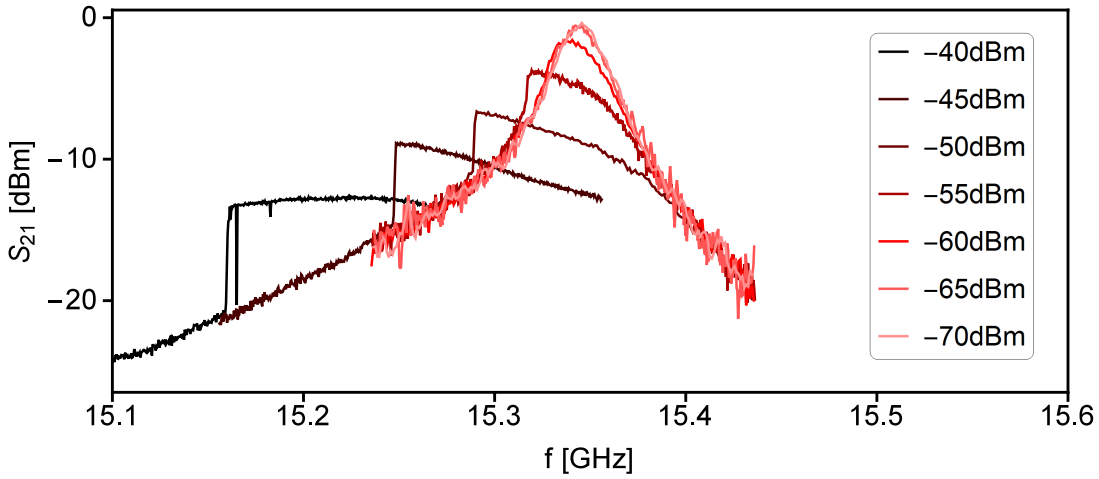


Figure V.4: Power dependence of the transmission spectrum of an LC resonator. The inset shows the color-coded values of the applied power. As the power increases, the resonance becomes nonlinear and bifurcates to the left.

of the resonators are measured. Here, the measurements are presented for the resonators in Fig. V.1 and Fig. V.2. The temperature dependence of the resonance frequencies of the two resonators are illustrated in Fig. V.5.

Eqn. II.43 for the temperature dependence of the resonance frequency includes free parameters $\lambda(0)$, T_c, L_m and C, and therefore can not be accurately fitted to the data. To fit the data, we first use reasonable arguments to fix some of these parameters. Firstly, we notice that for the Al resonators the thin film penetration depth $\lambda(0) = 100\,\text{nm}$ can be calculated using Eqn. II.39*, taking a value for the bulk London penetration depth for Al of $\lambda_L = 15\,\text{nm}$ [130]. Additionally, one can estimate the geometric inductance L_m^T of the meander line inductor. Eqn. II.38 gives the inductance of a microstrip wire with length l, width w and thickness t. The mutual inductance of such wires at a distance s from each other is given by [129]

$$M(l,s) \approx 2(Ln\frac{2l}{s} - 1 + \frac{s}{l} - \frac{s^2}{4l^2}) \cdot 10^{-7}[H]. \tag{V.2}$$

*In the further experiments a value for the Al penetration depth is measured which agrees with the calculated value.

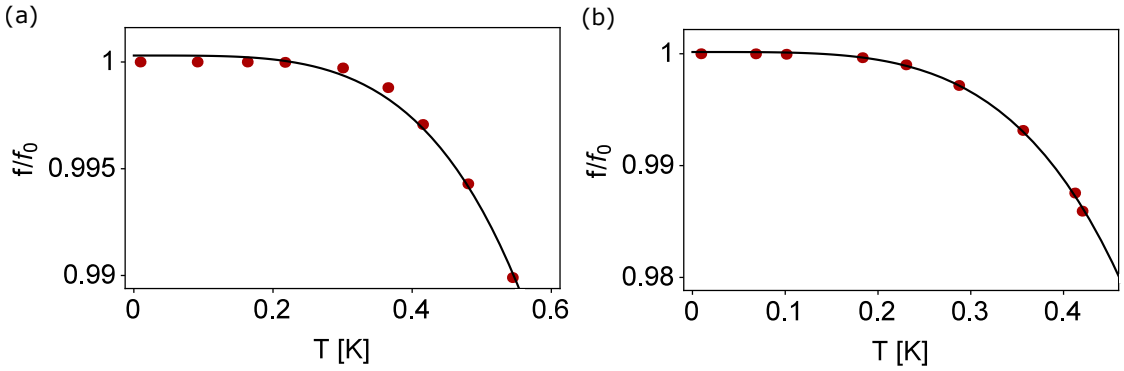


Figure V.5: Temperature dependences of the normalized resonance frequencies of Al (a) and Ti/Al (b) resonators. The solid lines are obtained by fitting the data to Eqn. II.42.

The total geometric inductance L_m^T of a meander line constructed by n parallel microstrip wires and arcs of radius r connecting them is obtained as

$$L_m^T = n(L_m(l) + L_m(\pi r)) + \sum_{k=1}^{n}\sum_{i\neq k}^{n}(-1)^{i-k}M(l, s_{i,k}). \tag{V.3}$$

The first term in this equation is the sum of geometric inductances of n microstrip wires and connecting arcs. The second term is the mutual inductances of wires i and k. When the integer (i-k) is even, the currents in the two wires are parallel and therefore the mutual inductance is added. Otherwise the current is antiparallel and the mutual inductance is subtracted from the total. The data in Fig. V.5a is therefore fitted taking the total capacitance C and the critical temperature of Al film T_c as the fitting parameters. We obtain $C = 43 \pm 0.2\,\mathrm{fF}$ and $T_c = 1.26 \pm 0.02\,\mathrm{K}$. The critical temperature is in a good agreement with that of the bulk Al.

Compared to the pure Al resonator (where we could base calculations on the known bulk penetration depth), for the Ti/Al resonator in Fig. V.5b, the penetration depth λ_0 can not be easily pre-calculated. On the other hand the resonator has a different capacitor pad radius and therefore different C. The data is fitted taking λ_0 and C as the fitting parameters and using $T_c = 0.86 \pm 0.005\,\mathrm{K}$ obtained from fitting the data of a Ti/Al resonator with the same capacitor pad radius as for the

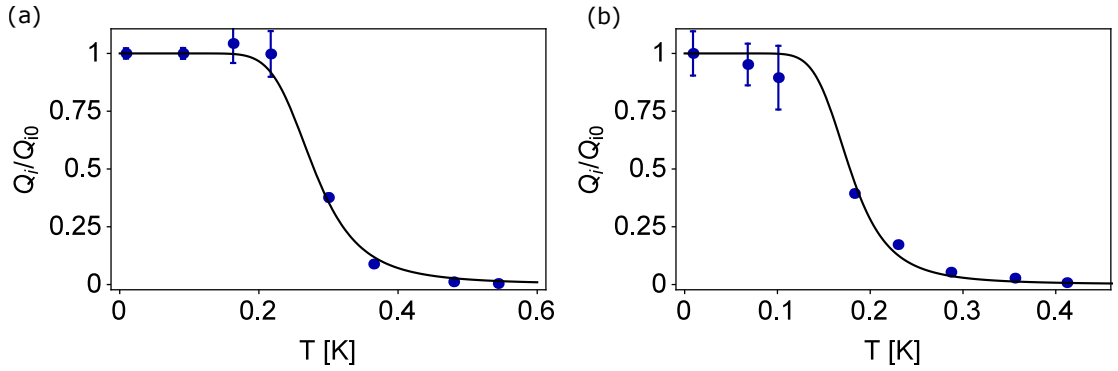


Figure V.6: Temperature dependences of the internal quality factors of Al (a) and Ti/Al (b) resonators. The solid lines are obtained by fitting the data to Eqn. V.4. $Q_i(0)$ and τ_n are taken as the fitting parameters. The data and the solid lines are plotted normalized to the obtained $Q_i(0)$.

Al resonator in Fig. V.5a. The capacitance of the new resonator is obtained from the fitting as $C = 28\,\mathrm{fF}$ and the bilayer penetration depth is $\lambda(0) = 159\,\mathrm{nm}$. The extracted value of the capacitance is lower than the capacitance for the Al resonator therefore resulting in a higher resonance frequency. Compared to the Al layer, the critical temperature of the Ti/Al bilayer is reduced, due to the Ti layer. On the other hand the obtained value of $\lambda(0)$ is larger for the bilayer than for pure Al. This is expected, since the London penetration depth of bulk Ti is $\lambda_L = 70\,\mathrm{nm}$ [152], and the critical temperature of the Ti/Al bilayer is reduced compared to bulk Al.

Fig. V.6 shows the temperature dependences of the internal quality factors of the two resonators. The data is fitted to

$$Q_i^{fit}(T) = \left(\frac{1}{Q_i(0)} + \frac{1}{Q_i(T)} \right)^{-1}, \tag{V.4}$$

where $Q_i(T)$ is given by Eqn. II.44. The internal quality factor at $T = 10\,\mathrm{mK}$ and the relaxation time τ_n are taken as the fitting parameters. We obtain $Q_i^{Al}(0) = 1.53 \cdot 10^4$, $\tau_n^{Al} = 6.4 \cdot 10^{-12}\,\mathrm{s}$ and $Q_i^{TiAl}(0) = 0.9 \cdot 10^4$, $\tau_n^{TiAl} = 8.8 \cdot 10^{-12}\,\mathrm{s}$. The obtained values for τ_n agree with the typical values of the relaxation time [130]. The data and the solid lines are plotted normalized by the values of $Q_i(0)$ obtained from the

fit. The quality factors are consistent with the values extracted from the fitting in Fig. V.1 and Fig. V.2. The data and the theoretical models therefore agree well for both single-layer and bilayer resonators.

This method of extracting the resonator and metallic layer parameters is used in the next section to understand the properties of Pd/Al bilayers.

2 Measuring Proximity in Pd/Al Bilayers Using LC Resonators

In this section we present a new method for studying the proximity effect in thin metallic bilayers. In particular, we are interested in superconducting properties of the Pd/Al bilayer. This bilayer is used to contact the carbon nanotubes and it results in rich superconducting proximity-induced transport characteristics, as shown in the previous chapter. It is therefore a promising candidate for incorporating nanotubes in microwave circuits.

The present measurements are done using the second type of resonator samples introduced in Section III.2.1. These samples consist of a single coplanar transmission line and four LC resonators capacitively coupled to it as shown in Fig. III.6b. The ground plane surrounding the resonators reduces the microwave coupling between them. The advantage of these samples is that multiple resonators prepared at the same evaporation step with different frequencies can be measured. This allows a detailed study of the properties of the particular metallic layer.

2.1 Proximity Effect in SN Bilayers

The proximity effect, referring to the coherent propagation of the superconducting order into the normal material, has been studied theoretically and experimentally since 1960s. The early knowledge about the proximity effect has been summarized

by Deutscher and De Gennes in 1969 [39]. The theoretical model developed by De Gennes is valid only close to the transition temperature. Subsequent theoretical developments have provided a much more advanced theoretical framework [153, 154]. The theory in the limit of dirty superconductors was developed by Usadel in 1970 [155]. More recently, a close relation between proximity effect and Andreev reflections has been established [16] and in SN junctions, where ballistic transport of electrons can be assumed, Bogoliubov-De-Gennes equations are used [156]. The proximity effect can be generally described as the combination of the Andreev reflection at the NS interface and the phase coherence maintained over a certain length scale in the normal layer.

The study of metal-based NS layers has been an active area of the proximity effect research since 1990s [157, 158, 159]. In these experiments, tunneling spectroscopy was used to measure the key parameters describing superconductivity, such as the superconducting gap, electron density of states, and their temperature dependences.

2.2 Measuring LC resonator frequency response in a multiplexed geometry

The properties of Pd/Al bilayers are studied by fabricating a range of microwave resonator samples with a varying Pd layer thickness between 0 and 7 nm. The thickness of the Al layer is kept constant at 80 nm. The frequencies of the resonators are tuned by changing the radius of the capacitor pads. To choose the desired range of frequencies, simulations of the resonator samples are carried out using Ansys HFSS software package (see Section VI.1).

An example measurement of the transmission spectrum at 10 mK of a resonator with 3 nm Pd layer is plotted in Fig. V.7. The amplitude of S_{21} shows a dip at the resonance frequency $f_0 = 19.24$ GHz, where the microwave field is strongly

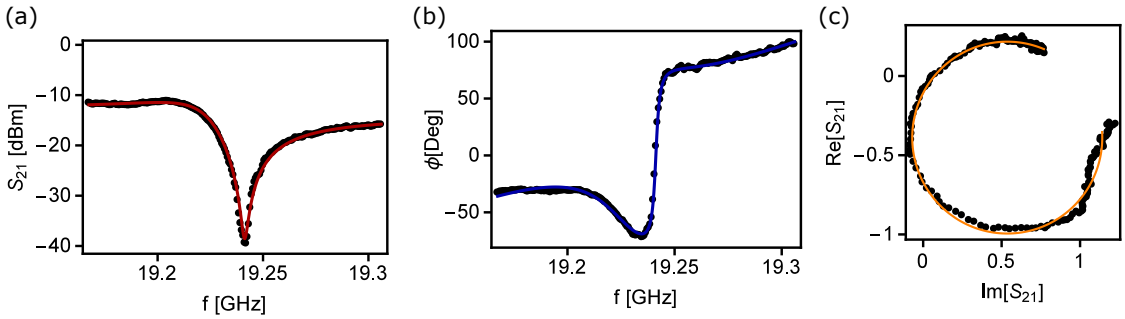


Figure V.7: a. Amplitude of the transmission spectrum of a Pd (3 nm)/Al (80 nm) resonator and the corresponding theoretical curve obtained by inserting the parameters extracted from fitting complex plane data with Eqn. II.36 in the logarithmic scale. b. Phase of S_{21} in degrees. The random phase of the cables is subtracted. c. Complex plane representation of the resonance fitted with Eqn. V.5. $Q_i = 8.4 \cdot 10^3$, $f_0 = 19.24\,\text{GHz}$ and $\phi_0 = 0.69$ are extracted from the fitting.

absorbed by the resonator. The phase and complex plane representations of the resonance are plotted correspondingly in Fig. V.7b and c. The data in the complex plane is fitted to the equation

$$S_{21}^{-1} = 1 + \frac{Q_i}{Q_e^*} e^{i\phi_0} \frac{1}{1 + i2Q_i\delta\omega} \tag{V.5}$$

already introduced in Section II.3.2 (Eqn. II.36). The parameters extracted from the fit are $Q_i = 8.4 \cdot 10^3$, $f_0 = 19.24\,\text{GHz}$ and $\phi_0 = 30°$. Using these parameters the theoretical curves of the amplitude and phase of S_{21} are obtained and overlaid to the data in Fig. V.7a and b. The model and the experimental data agree well. It is important to notice that the transmission spectrum is asymmetric with respect to the resonance frequency, as seen in Fig. V.7a. The reason for this asymmetry is the impedance mismatch at the two sides of the transmission line, which can be due to the imperfections of the external microwave circuitry such as the bond wire connections and the transmission lines on the PCB. In the theoretical model in Eqn. II.36 this mismatch is accounted for by the asymmetry angle ϕ_0, which results in a rotation of the circle in the complex plane representation. The obtained values for ϕ_0 range between 0-30° for the measured resonators.

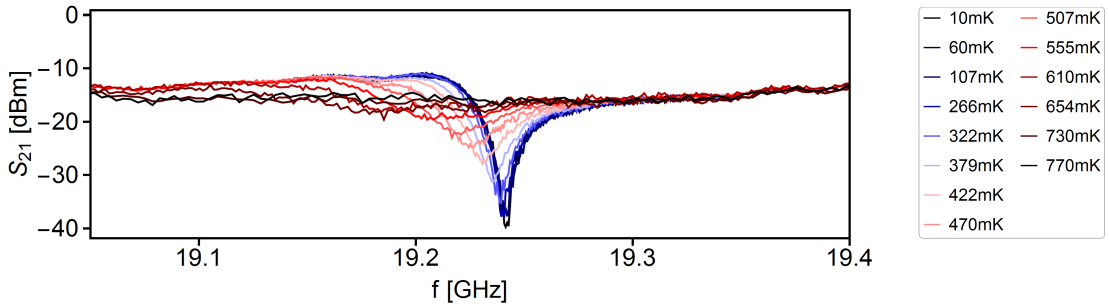


Figure V.8: The temperature dependence of the transmission spectrum of the resonator in Fig. V.7. The color coded temperature values are presented on the right. As the temperature increases, the resonance dips shift to the left and their quality factor decreases.

The transmission spectrum of four such resonances of different frequencies are measured for all thicknesses of the Pd layer. The quality factors, resonance frequencies and the impedance mismatch angle are then accurately extracted by fitting the data to the theoretical model.

2.3 Extracting LC resonator parameters from their temperature dependence

In order to characterize the superconducting properties of different Pd/Al bilayers, temperature dependent measurements are done for each resonator and Pd thickness. Fig. V.8 shows the temperature measurement of the resonance amplitude of the 3 nm Pd resonator. As the temperature is increased, the dip shifts to the left and the quality factor decreases. The dip disappears at the critical temperature of the bilayer. By fitting the measured transmission spectrum for each temperature, the temperature dependences of the internal quality factors and the resonance frequencies are extracted for all the resonators. Examples of the temperature dependences of the resonance frequency and internal quality factor are shown in Fig. V.9. The theoretical model for the obtained data is described by equations

$$L_k(T) = \mu \frac{\lambda(0)^2}{1-(T/T_c)^4}\frac{l}{A}, \quad f(T) = \frac{1}{2\pi}\frac{1}{\sqrt{(C(L_m + L_k(T)))}} \tag{V.6}$$

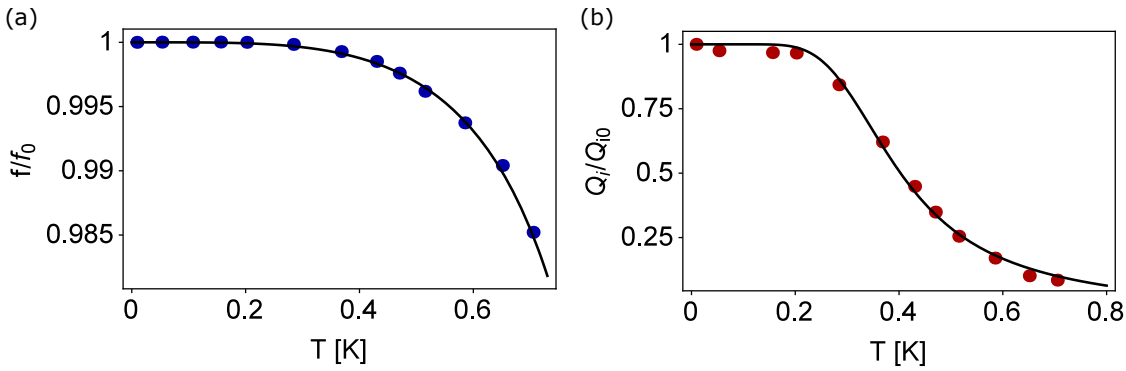


Figure V.9: a. Temperature dependence of the frequency obtained from fitting the transmission to Eqn. V.5. The resonance frequency decreases with temperature. The data is fitted to Eqn. V.6, yielding the value of the magnetic field penetration depth $\lambda(0)$. b. The temperature dependence of the internal quality factor. The theoretical curve is obtained by fitting the data to Eqn. V.7. The data in a and b are fitted for the same values of $\lambda(0)$, T_c and τ_n.

and

$$Q_i(T) = \frac{L_m + L_k(T)}{\tau_n \omega(T) L_k(T)} exp(1.764 T_c/T), \tag{V.7}$$

where $\lambda(0)$ is the magnetic field penetration depth at zero temperature, L and A are the length and the cross-sectional area of the inductor. τ_n is the room temperature electron relaxation time [130]. For the inductors in Fig. III.6b, the temperature and material-independent geometrical inductance can be calculated from

$$L_m = 2l(Log\frac{2l}{w+t} + 0.5 + 0.2235\frac{w+t}{l}) \cdot 10^{-7}[H], \tag{V.8}$$

where $l = 1.5\,\text{mm}$ is the total length of the inductor line, $w = 1\,\mu\text{m}$ is its width and t is the total thickness of the metallic layer that ranges from 80-87 nm. The capacitances C of the resonators are expressed as

$$C = \frac{1}{4\pi^2 (L_m + L_k(T))^2 f_0^2}, \tag{V.9}$$

where f_0 is the resonance frequency at 10 mK. Eqns. V.6 and V.7 contain three unknown parameters, $\lambda(0)$, T_c and τ_n. Note that in Eqn. V.7, the temperature dependence of the resonance frequency is very small and $\omega(T) \approx \omega(T{=}10\,\text{mK})$

is assumed. Temperature dependences of f_0 and Q_i are fitted simultaneously to Eqns. V.6 and V.7 for the same set of the unknown parameters for each resonance. The resulting theoretical curves are plotted for the example data in Fig. V.9. A good agreement between the theory and the data is observed and the parameters λ_0, T_c and τ_n can be uniquely extracted for all the resonators for each thickness of Pd.

2.4 Study of the Critical Temperature of Pd/Al Bilayers

The critical temperatures for each resonator at each Pd thickness extracted from fits similar to Fig. V.9 are shown in Fig. V.10a. The value of the critical temperature of the 80 nm Al film agrees with the bulk Al T_c. The values of the critical temperature for the resonators made from the same Pd thickness are in a good agreement with each other, proving the reliability of the method for extracting the T_c.

As expected, the T_c decreases with the increasing thickness of the normal Pd layer. The Usadel equations can be used to theoretically model the observed behaviour [160]. The Usadel theory is based on the assumption that the particles travel diffusively through the metal. This is a good assumption for thin-film superconductors because electrons either have short mean-free paths in the metals or scatter diffusively from the boundaries [161].

In the limit of thin bilayers, the transition temperature has been derived by Martinis *et. al.* [161], and is given by

$$\begin{aligned} T_c &= T_{c0}\left[\frac{d_s}{d_0}\frac{1}{1.13(1+1/\alpha)}\frac{1}{t}\right]^{\alpha}, \\ \frac{1}{d_0} &= \frac{\pi}{2}k_B T_{c0}\lambda_f^2 n_s, \\ \alpha &= d_n n_n / d_s n_s. \end{aligned} \tag{V.10}$$

T_{c0} is the transition temperature of the bare superconductor, which is equal to 1.2 K for the Al layer. d_s and d_n are correspondingly the thicknesses of the superconducting

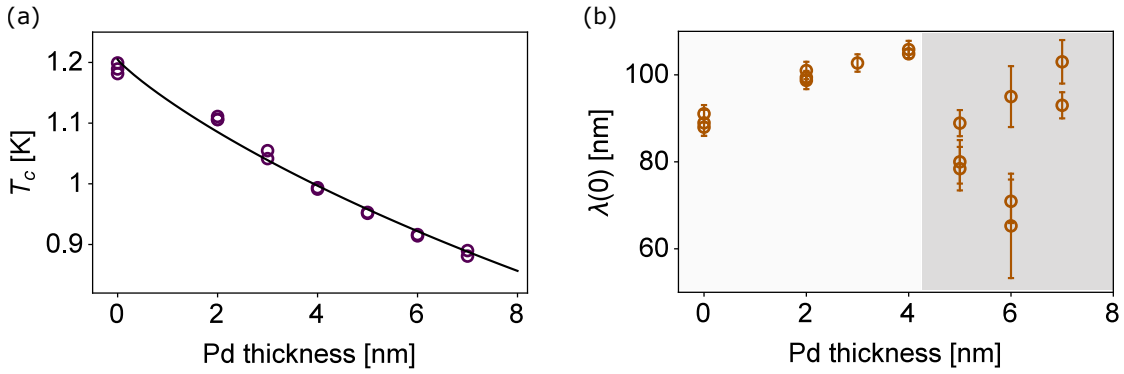


Figure V.10: a. Critical temperatures of Pd/Al bilayers for each resonator. Pd layer thickness is plotted on the x-axis. The normal Pd layer suppresses the superconductivity in the bilayer causing the decrease in the T_c. The data is fitted to Eqn. V.10 taking λ_f^2/t and T_{c0} as the fitting parameters. b. The magnetic field penetration depth of the Pd/Al bilayers with different Pd thicknesses. The two gray regions correspond to resonators made from different Al sources. $\lambda(0)$ consistently increases in the first region, whereas it is inconsistent for the second set of resonators.

and normal layers. $n_s = 1.81 \cdot 10^{29}\,\text{states/eVm}^3$ and $n_n = 1.02 \cdot 10^{29}\,\text{states/eVm}^3$ are the densities of states in Al and Pd. λ_f is the effective Fermi wavelength. t is the transmission coefficient that depends on the roughness of the NS interface. For most of the clean metals this coefficient is of the order of one.

Eqn. V.10 is used to fit the data in Fig. V.10a, where T_{c0} and λ_f^2/t are the fitting parameters. We obtain $T_{c0} = 1.2\,\text{K}$ and $\lambda_f^2/t = 0.0216\,\text{nm}^2$. For an ideal transmission through the interface, t=1, the Fermi wavelength is therefore $\lambda_f = 0.15\,\text{nm}$. This can be compared to the Fermi wavelength of Al roughly estimated from the its Fermi energy $E_F^{Al} = 11.7\,\text{eV}$ as

$$\lambda_f = \frac{h}{P_F} = \frac{hv_F}{2E_F} = 0.35\,\text{nm}. \tag{V.11}$$

The obtained values are of the same order of magnitude. The suppression of the transition temperature with the thickness of the normal layer is therefore well-described by Eqn. V.10.

2.4.1 Magnetic Field Penetration Depth

Since the discovery of the proximity effect, there have been numerous theoretical and experimental studies of the magnetic penetration depth λ in conventional layered superconductors [162, 163, 164]. Experimental results from the surface impedance measurements [163], the two-coil mutual inductance measurements [165] and the ac susceptibility measurements [166] showed altered screening of the applied magnetic field, not characteristic for homogeneous superconductors. In the proximity-coupled systems λ is an overall screening length which does not correspond to the screening lengths of the individual constituents due to the nonuniform nature of the superconductivity.

The measurement method discussed above allows investigating the effective magnetic field screening in Pd/Al proximity superconductors. The extracted values of the critical temperature for different Pd thicknesses can be used to obtain the magnetic field penetration depth from the temperature dependences of the resonance frequencies. The values of the penetration depth at zero temperature $\lambda(0)$ for each resonator made from different Pd thicknesses are plotted in Fig. V.10b. For the pure Al layer of 80 nm $\lambda(0) \approx 90$ nm is found. Using the equation for the thin layer penetration depth (Eqn. II.39) one can find the expected value for $\lambda(0)$. Taking into account that the bulk London penetration depth of Al is $\lambda_L = 15\,nm$ [167], we find $\lambda(0) = 100$ nm, which agrees with the obtained value.

The penetration depth values obtained for the resonators up to 4 nm Pd thickness are in a good agreement with each other and they consistently increase as a function of the thickness. This behaviour of the penetration depth has been observed before for example in Nb/Cu superconducting bilayers [163, 168]. In such NS bilayers the superconducting properties of the S layer, which has the dominant role in screening

the magnetic field, are suppressed due to the normal layer. This therefore causes the increase in the penetration depth with the normal layer thickness.

Unlike this, the values for higher thicknesses of Pd are scattered. The reason is that the higher temperature measurements, which determine $\lambda(0)$, are not very accurate for the second set of resonators. In addition, the resonators with thicker Pd generally have lower quality factors, which makes it difficult to fit the measured spectra to the theory.

2.5 Discussion and Conclusion

In this chapter, measurements of two types of LC resonator samples are presented. Firstly, single resonators capacitively coupled to input and output ports are presented. Such measurements allow optimizing the geometries of the capacitor pads and the inductor. In particular, transmission measurements of two resonators made from Al(50 nm) and Ti(5 nm)/Al(50 nm) are presented. The transmission data of the resonances in the complex plane are fitted to the theoretical model, showing a good agreement between the two. The resonance parameters can therefore be reliably extracted from the fitting. In particular, the obtained values of the internal quality factors are of the order of 10^4 for both resonators, therefore proving the reliability of the fabrication methods.

Temperature dependences of the transmission spectra for the resonators are performed. By fitting the resonance frequency and the internal quality factor to the Eqns. V.6 and V.7, the critical temperatures and the magnetic penetration depths of the metallic layers can be extracted. On the other hand, the critical temperature of the Ti/Al bilayer of 0.86 K is strongly reduced due to the Ti layer which suppresses the superconducting properties of the proximity bilayer compared to those of the pure Al. The analysis method additionally allows extracting the

values of the effective electron relaxation time τ_n which does not change noticeably for the two presented superconducting layers.

The established fabrication and measurement methods for the single LC resonators are then used for more rigorous studies of the material properties. In the second part of the section a new method of studying the superconducting proximity effect in proximity bilayers is introduced. We study the proximity in Pd/Al bilayers. Since this yields good superconducting contacts to carbon nanotubes and can therefore be used to incorporate the latter in microwave circuits. The studied samples consist of several LC resonators with different resonance frequencies coupled to a single transmission line. The advantage of these samples is that multiple resonators can be fabricated in the same evaporation step. This also increases the effectiveness of the measurements as all resonators on a single sample can be measured through one pair of microwave cables. To study the superconducting properties of the proximity Pd/Al bilayers, a series of samples with varying Pd thicknesses have been prepared and measured. The measured transmission spectra were fitted to a theoretical equation for S_{21} obtained from the transmission matrix model. A good agreement between the theory and the experimental data allow us to extract the values of the resonance parameters such as the quality factors and the resonance frequencies.

By carrying out temperature measurements of the transmission spectra for each resonator and each Pd thickness, the temperature dependences of corresponding internal quality factors and resonance frequencies are obtained. These are then fitted to the theoretical models yielding several parameters characterizing the superconducting properties of each Pd/Al bilayer. In particular, this method allows to accurately extract the transition temperatures and magnetic field penetration depths of the bilayers. A wide variety of theories exists for modeling the proximity

effect in superconductor/normal metal bilayers. However, their predictions of the superconducting properties are generally only qualitatively correct. The experimental methods used to measure the superconducting properties of NS bilayers include tunneling spectroscopy measurements of the resistivity of the bilayers [169], kinetic inductance measurements [165] as well as surface impedance measurements [163]. Compared to these, measuring the superconducting properties of bilayers through microwave resonators provides with a more straightforward way of extracting the characteristic parameters of superconductivity and their thickness-dependences.

The obtained critical temperatures show an expected decrease with the increasing thickness of the normal layer thickness. This can be modeled with an equation for the bilayer T_c valid for thin layers. A good agreement with the model is observed. By fitting the experimental data of the T_c to the model a parameter depending on the effective Fermi wavelength and the NS interface transparency can be extracted. This gives a good estimate of the interface transparency for theoretically predicted values of the Fermi wavelength, which is important in various applications of the proximity bilayers. In addition to the critical temperature, the thickness-dependence of the magnetic penetration depth can be extracted from the measurements. For Pd thicknesses up to 4 nm, a consistent increase in the penetration depth is observed, as expected. However, for higher thicknesses, the obtained values do not agree with each other. This is due to inaccurate measurements of the resonators in the second set of thicknesses at higher temperatures, which have the largest contribution in determining $\lambda(0)$. Additionally, we observe a general decrease in the quality factors at higher Pd thicknesses, and therefore more inaccurate fits of the transmission spectra.

As a conclusion, a good agreement of the experimental observations and the theoretical predictions for the superconducting properties of NS bilayers is observed. Therefore, the above introduced method constitutes a reliable way of extracting the

superconducting properties of bilayers. In particular, the understanding of properties of Pd/Al bilayers in microwave resonators can be combined with our earlier studies of their use in DC contacted nanotube devices to provide a good background to now move on to integrate nanotubes into SN-bilayer microwave circuits.

VI

Embedding carbon nanotubes in an SN-bilayer microwave LC circuit

Contents

1 Design of LC resonator nanotube coupled devices . . . 138
2 Probing Coulomb Blockade with Microwave Field . . . 141
2.1 Circuit Model of Nanotube SQUID-Resonator System . 144
2.2 Power Dependence of the Amplitude Dips 148
3 Discussion and Conclusion 151

In Chapters IVand V the DC carbon nanotube devices and LC microwave resonators were individually studied in detail. In this chapter we move on to describe first experiments integrating these two together. We show first results of probing the transport of a nanotube that is embedded in a superconducting LC circuit. A repeatable gate dependence is observed in the microwave transmission of the LC circuit, due to tuning the quantum states in the nanotube. The results indicate that probing of Andreev physics in nanotubes via embedding in a microwave resonator, and nanotube Andreev bound state circuit QED are now within reach.

1 Design of LC resonator nanotube coupled devices

The design and fabrication methods of the coupled nanotube-LC resonator devices were introduced in Section III.3. Each sample consists of four devices in which a nanotube is embedded in a superconducting loop that is in turn directly embedded in an LC resonator. The resonators are capacitively coupled to coplanar input and output transmission lines. The devices are all fabricated from a 4/80 nm Pd/Al SN bilayer, based on our success with this combination in DC nanotube and LC circuit measurements described in Chapters IV and V respectively.

To understand the behaviour of the microwave field in the samples, a finite element high frequency simulation software Ansys HFSS is used. Due to the limitations of the experimental circuitry, the accessible frequency range is $8 - 12$ GHz. In order to design the resonators in this frequency range, their frequencies are first predicted using analytical equations and the measurements of individual resonators discussed in Chapter V. In addition to this, the predicted LC geometries are simulated with HFSS yielding more precise positions of the resonances. Fig. VI.1 shows the model of the sample in HFSS. The substrate shown in dark gray is modeled to be a highly resistive 0.5 mm thick Si with conductivity $\sigma = 10^{-2}$ S/m and a dielectric constant $\epsilon = 11.7$. The metallic layer on top of the substrate consisting of the resonators in white, ports in yellow and ground planes in orange has a thickness of approximately 80 nm, much smaller than the thickness of the substrate. It is modeled as a two-dimensional perfectly conductive boundary. The vacuum box surrounding the sample (shown in light blue), which mimics the copper sample holder, limits the simulation space and has perfect electrical conductor boundary conditions assigned on its surfaces. This forces the electrical field to be

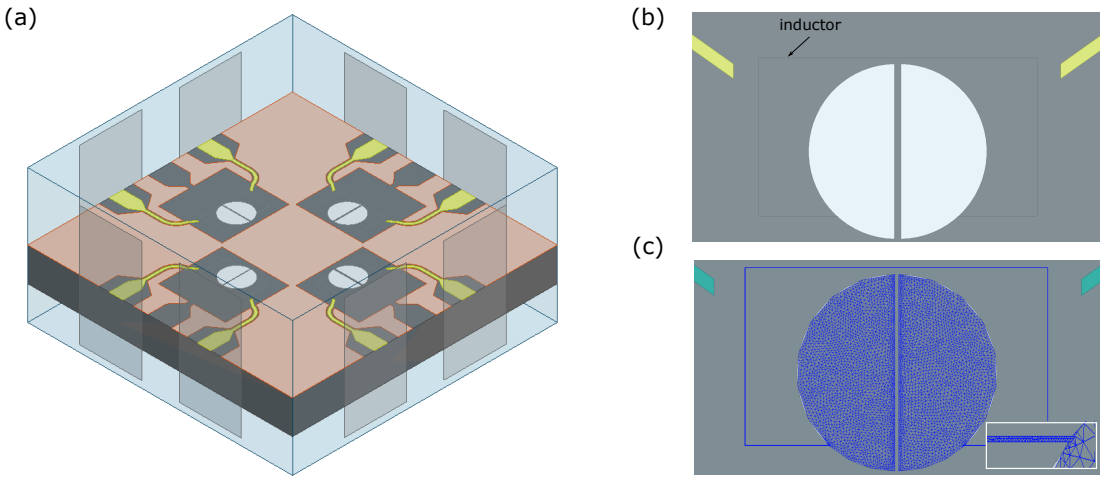


Figure VI.1: a. The HFSS model of the sample of coupled nanotube SQUID-resonator devices. The devices (white), microwave ports (yellow) and the ground plane (orange) are modelled as 2D perfectly conducting boundaries on top of the silicon substrate (dark gray). The sample is surrounded by a vacuum box (light blue). The gray rectangles on the vacuum box represent the microwave excitation sources. b. A zoomed-in picture of the LC resonator model showing the inductor line, the capacitor bads and the microwave ports. c. The discrete mesh generated on the capacitor plates and the inductor line.

normal to the surface. The microwave excitation sources are modeled as the gray rectangles on the vacuum box, perpendicular to the substrate.

Fig. VI.1b is a zoomed in picture of a resonator, where the capacitor plates and the inductor line can be seen. The simulation takes into account only the geometric inductance. However, since the geometric inductance is much larger than the kinetic inductance, the latter would have minor influence on the results. Note that the nanotube SQUIDs are not modeled, as they do not noticeably influence the fields in the resonators and the resonance frequencies. This is due to the much smaller dimensions of the SQUIDs and large distances from the resonator fields concentrated mainly within the capacitor plates.

To solve the model for the electromagnetic field, a discrete mesh has to be generated. For large objects, such as the vacuum box, the silicon and the ground plane, this is automatically generated based on the geometry and the boundary conditions. On the other hand, to achieve accurate results, the mesh

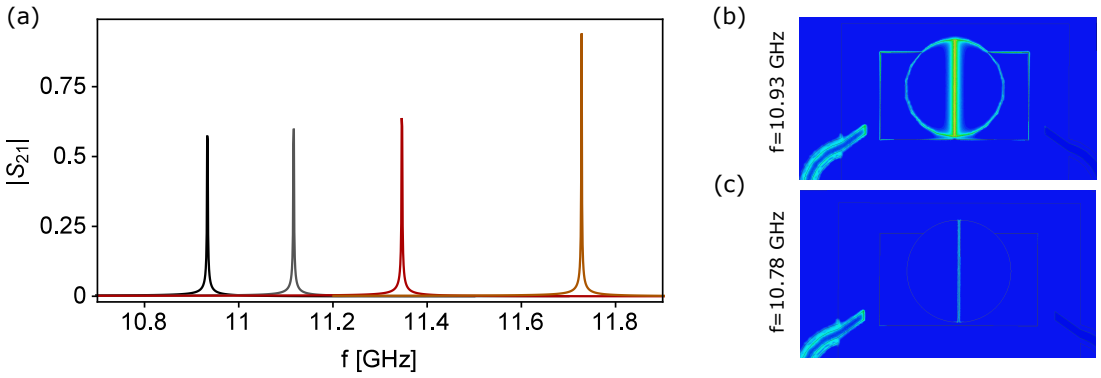


Figure VI.2: a. Amplitudes of four resonances on the sample with capacitor plate distances corresponding to 8 μm, 12 μm, 16 μm and 20 μm from left to right obtained from HFSS simulations. As the distance increases the capacitance decreases therefore increasing the resonance frequency. b. The electrical field amplitude distribution at the resonance of the first resonator. The field is the highest between the capacitor plates and the microwave signal is transmitted through the resonator. c. The electrical field distribution off resonance. No signal is transmitted through the resonator.

on the inductor lines and the capacitor plates is further refined and optimized as illustrated in Fig. VI.1c.

The radius of the capacitor plates is 0.21 μm and the length of the inductor lines is 1.9 mm. The resonance frequencies of the resonators are tuned by choosing the capacitor plate distances to be 8 μm, 12 μm, 16 μm and 20 μm.

The results of the simulations of each resonator are plotted in Fig. VI.2a. Four Lorenzian peaks are observed at the resonance frequencies, which increase for larger capacitor plate distances as the capacitance decreases. Fig. VI.2b shows the color-coded field amplitude at the resonance of the first resonator at 10.93 GHz. The highest field is observed between the capacitor plates, and the microwave signal is transmitted through the resonator resulting in a resonance peak. On the other hand, the off resonance field shown in Fig. VI.2c has the highest amplitude at the input port on the left side and no signal is transmitted through the resonator.

Using the simulation results, one can estimate the total capacitances of the resonators. Eqns. V.6 and V.8 are used to calculate the total inductance at 10 mK for

an inductor with length $l = 1.9\,\mathrm{mm}$, width $w = 1\,\mu\mathrm{m}$ and film thickness $t = 80\,\mathrm{nm}$. Note that a perfect conductivity of the metallic layer is assumed, whereas in the experiments one should also take into account the finite conductivity of the Pd/Al layer. We obtain $L_{tot} \approx 3.3\,\mathrm{nH}$. Using the simulated resonance frequency values of $f_1 = 10.93\,\mathrm{GHz}$, $f_1 = 11.11\,\mathrm{GHz}$, $f_1 = 11.34\,\mathrm{GHz}$ and $f_1 = 11.72\,\mathrm{GHz}$ we obtain $C_1 = 64.3\,\mathrm{fF}$, $C_2 = 62.3\,\mathrm{fF}$, $C_3 = 59.8\,\mathrm{fF}$ and $C_4 = 56\,\mathrm{fF}$.

The simulation results are used to fabricate the LC resonators of the coupled devices with the desired frequencies. A comparison to the experimental results is shown in the next section.

2 Probing Coulomb Blockade with Microwave Field

In this section we introduce the measurements of a carbon nanotube SQUID coupled to a microwave LC resonator in a planar geometry. The sample consists of four coupled devices. The capacitor plate distances for the LC resonators are $8\,\mu\mathrm{m}$, $12\,\mu\mathrm{m}$, $16\,\mu\mathrm{m}$ and $20\,\mu\mathrm{m}$. Based on the measurements of the DC nanotube devices and the LC resonators, the metallic layer is chosen to be Pd (4)nm/Al (80 nm). The samples are mounted in the sample holder anchored at 10 mK stage of the dilution refrigerator. The transmission through each resonator is measured as described in Section III.3.2.

The transmission amplitude normalized to maximum values for each resonator is plotted in Fig. VI.3a. The observed four resonances are at $f_1 = 10.405\,\mathrm{GHz}$, $f_2 = 10.53\,\mathrm{GHz}$, $f_3 = 10.73\,\mathrm{GHz}$ and $f_4 = 11\,\mathrm{GHz}$. Compared to the simulation results in Fig. VI.2a, the measured resonances are shifted towards lower frequencies by approximately 500 MHz. This can be due to the kinetic inductance not taken into account in the simulations. On the other hand, the actual distances of the capacitor plates might be smaller compared to the designed values for example due to the over-exposure during the electron beam lithography. The internal quality

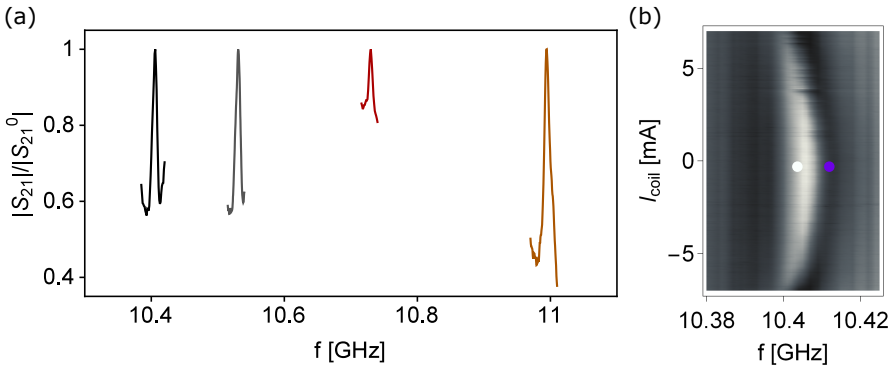


Figure VI.3: a. Normalized amplitudes of four resonances on the sample with capacitor plate distances corresponding to 8 μm, 12 μm, 16 μm and 20 μm from left to right measured at 10 mK. The background transmission is not plotted for clarity b. The resonance spectrum of the first resonator measured as a function of the current through the magnetic coil mounted underneath the sample. As the absolute value of the current increases, the magnetic field increases. This causes the suppression of the superconductivity in the Pd/Al film, due to which the resonance shifts and eventually disappears.

factors of the resonances are found from the fits to Eqn. V.1, yielding $Q_1 = 905$, $Q_2 = 600$, $Q_3 = 1000$ and $Q_4 = 1000$. Large background transmission is measured on each spectrum along with the resonances. This can be due to the fact that the bond wires connecting the sample port and ground plane to the external PCB are very dense and a large cross-coupling is possible between them. To ensure that the measured resonances correspond to the LC resonators, magnetic flux dependence is measured. Fig. VI.3b shows the resonance spectrum for the resonator at 10.405 GHz measured as a function of the current through the magnetic coil mounted underneath the sample. As the current increases, the resonance shifts towards lower frequencies and disappears for large currents. The magnetic field of the coil at the position of the sample is estimated to be around 8 mT at $I_{coil} = 7$ mA, taking into account the coil dimensions and its distance from the sample. This value is close to the critical field of approximately 10 mT of the Al film at which the superconductivity is suppressed. The latter causes the resonance to disappear. The increasing magnetic field suppresses the superconductivity of the bilayer therefore

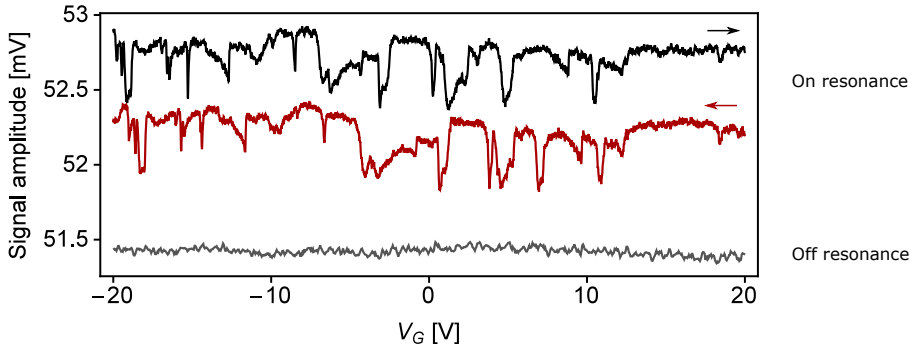


Figure VI.4: Amplitude of the resonance at 10.41 GHz as a function of the voltage applied to the side-gate to the nanotube when sweeping the gate in a positive (black) or a negative (red) direction. The two at the red dot in Fig. VI.3b are vertically shifted for clarity. Multiple dips are observed in the amplitude, which show a hysteresis depending on the direction of sweeping the gate voltage. The gray plot is the off-resonance amplitude of S_{21} at the black dot in Fig. VI.3b, where no substantial changes are observed.

increasing the magnetic penetration depth in it. This causes the increase in the kinetic inductance and a shift in the resonance frequency to lower values. Similar behaviour is measured for all resonances in Fig. VI.3a.

When Andreev bound states exist in the nanotube, a modulation of the resonance at lower flux values is expected (see Eqn. II.27). The latter is not observed in our measurements.

We now turn our attention to the influence of the DC side-gate of the nanotube shown in Fig. III.8 on the observed resonances. In Fig. VI.4 the transmission amplitude of the 10.405 GHz resonator is plotted as a function of the gate voltage on- and off-resonance (white and purple dots in Fig. VI.3b). The black and red curves in the on-resonance case correspond to sweeping the gate voltage towards positive and negative directions. The two curves are vertically shifted for clarity. Multiple dips are observed with the changing gate voltage. A hysteric behaviour of these dips is observed when sweeping the gate voltage in the two directions. This can be due to the fact the the LC/nanotube system is floating with respect to the ground, and it does not have a well defined potential. The latter can drift

due to the charges moving slowly in the environment. A solution in future is to ground one side of the resonator.

In contrast to the on-resonant curves, in the off-resonance curve no amplitude changes are observed with the gate voltage. The gate dependence of the resonance amplitude is observed only in one out of the four devices. The SEM imaging showed that in the remaining three devices the SQUIDs were not contacting the nanotubes due to a misalignment in the fabrication process.

To understand the behaviour in the on-resonant case we consider the electrical circuit equivalent to the nanotube SQUID-resonator system.

2.1 Circuit Model of Nanotube SQUID-Resonator System

Fig. VI.5a shows the circuit diagram equivalent to the coupled system. The microwave resonator with capacitance C and inductance $L = L_s + L_r$ is coupled to input and output ports via capacitances C_k. Part of the inductance L_s is shared with the nanotube SQUID. L_1 and L_2 represent the inductances of the metallic parts of the SQUID loop. C_m is the capacitance between the source and drain contacts of the nanotube. The nanotube can be modeled by constructing its equivalent circuit representation. Such a model has been proposed by P. J. Burke in [170] for single-walled carbon nanotubes in a ballistic transport regime. The effective circuit consists of an inductance L_{NT} and $C_{NT} = C^E_{NT} + C^Q_{NT}$, where C^E_{NT} and C^Q_{NT} are correspondingly the electrostatic and quantum components of the nanotube capacitance. The more general case of the non-ballistic transport can be addressed by adding a series diffusive component R_{NT} to the model as shown in Fig. VI.5a [171].

It has been shown that the kinetic inductance of a nanotube always dominates its geometric inductance which is ignored in the circuit [172]. The kinetic inductance

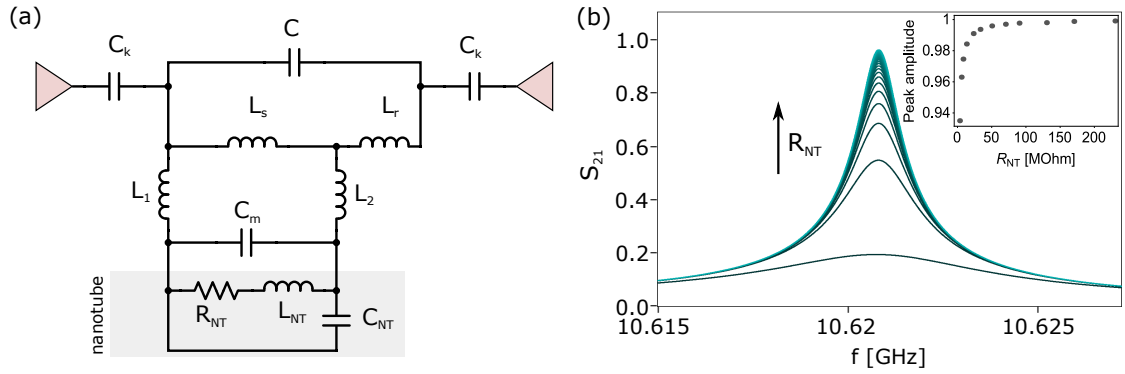


Figure VI.5: a. The circuit diagram equivalent to the coupled nanotube SQUID-LC resonator system. The parallel capacitance C and inductance $L = L_s + L_m$ form the resonator which is coupled to input and output microwave ports via capacitances C_k. The nanotube SQUID shares L_s of the resonator inductor. The inductance of the metallic part of the SQUID is $L_1 + L_2$. The carbon nanotube is modeled as an RLC circuit, where $L_{NT} \approx L^k_{NT}$ and C_{NT} is the sum of electrostatic and quantum components. R_{NT} is the diffusive component of the circuit representing the general case of a non-ballistic transport through the nanotube. b. The simulated transmission of the circuit showing a resonance at 10.62 GHz. R_{NT} is tuned between 50 kOhm and 3 MOhm. When increasing R_{NT} the resonance becomes sharper and its amplitude increases due to a lower microwave loss through the resistance. The inset shows the resonance peak amplitude depending on R_{NT}. For infinitely large value of R_{NT}, the peak amplitude goes to 1.

per unit length of a nanotube is given by

$$L^{NT} = \frac{h}{2e^2 v_F} = 16\,\mathrm{nH}/\mu\mathrm{m}, \tag{VI.1}$$

where $v_F = 8 \cdot 10^5\,\mathrm{m/s}$. The electrostatic capacitance between a wire and a ground plane is given by [173]

$$C^E_{NT} \approx \frac{2\pi\epsilon}{Ln(h/d)} \approx 50\,\mathrm{aF}/\mu\mathrm{m}, \tag{VI.2}$$

This is valid when the distance h to the ground is larger than the wire length. d is the wire diameter. Besides the classical electrostatic capacitance, one should also consider the quantum capacitance of the nanotube. This accounts for the fact that an electron can only be added to an available quantum state above the Fermi level. This capacitance can be found from

$$\frac{e^2}{C^Q_{NT}} = \frac{\hbar v_F \pi}{L}. \tag{VI.3}$$

The right side of this equation is the quantum level spacing of a nanotube with length L. For the quantum capacitance per unit length we find

$$C_{NT}^{Q} = 100\,\mathrm{aF}/\mu\mathrm{m}. \tag{VI.4}$$

The capacitance $C_m = 0.476\,\mathrm{fF}$ between the source and drain contacts is found from HFSS simulations. The coupling capacitances are similarly estimated from the simulations to be around 2 fF. Subtracting the coupling capacitances from the total capacitance of 71 fF for the 10.41 GHz resonance frequency estimated from the measurements we find $C = 67\,\mathrm{fF}$. The total inductance of the metallic part of the SQUID loop can be estimated from Eqn. II.38 to be about 0.5 nH. The total inductance of the resonator is 3.3 nH, from which the shared part is $L_s = 1\,\mathrm{nH}$. Using the above mentioned values, the transmission through the circuit is simulated using NI AWR Microwave Office environment. The result of the simulation is shown in Fig. VI.5b, which shows a resonance at 10.62 GHz. This value is closer to the experimentally measured value compared to the value obtained from the HFSS simulations, as the kinetic inductance of the resonator inductor has been taken into account.

When tuning the gate voltage, the resistance of the nanotube changes as discussed in Chapter IV. Fig. VI.5b shows the effect of tuning the nanotube resistance R_{NT} on the resonance. As the resistance increases, the resonance peak amplitude increases. This is due to the fact that for a larger R_{NT}, less current flows through it therefore the microwave loss is smaller resulting in a higher quality factor*.

Taking this into account, a dip on the on-resonance curve in Fig. VI.4 can be interpreted as a sharp decrease in the nanotube resistance. This, for example,

*The quality factor can be found by $Q = \omega C^* R^*$, where R^* is an effective parallel resistance that depends on R_{NT}.

can be due to a Coulomb blockade in the nanotube where sharp increase of the conductance happens when the quantum level in the nanotube is aligned with the Fermi level of the leads. The average change in the dip amplitude in Fig. VI.4 is around 1%. We compare this to the change expected in case of a Coulomb blockade. We consider the measurement of the Coulomb blockade discussed in Chapter IV. As shown in Fig. IV.1a, the smallest change in differential conductance between on- and off-resonance is observed for $-2\,\mathrm{V} < V_G < 2\,\mathrm{V}$. Here the resistance of the nanotube is approximately 3 MOhm at the Coulomb resonance. The circuit simulation result plotted in the inset of Fig. VI.5b shows that when the resistance changes from this value to a theoretically infinite value in the blockade regime (where the simulated peak amplitude is 1) the transmission amplitude changes by approximately 6%. This is larger than the amplitude changes observed in Fig. VI.4. A smaller 1% change observed in the experiment could be possible if the resistance of the nanotube on the Coulomb resonance was for example 25 MOhm. This could be the case if the nanotube was highly resistive. The discrepancy, however, can also be due to the inaccuracy of the LC model of the nanotube. In addition, the nanotube quantum capacitance change when tuning the gate voltage is not taken into account in the circuit simulations. The latter would result in a resonance frequency shift which would further affect the transmission amplitude probed at a constant frequency. Therefore, a more accurate circuit model and further measurements of coupled devices are necessary to better understand the origin of the observed dips. However, in the further discussion we assume that they are due to the Coulomb blockade in the nanotube.

2.2 Power Dependence of the Amplitude Dips

Fig. VI.6a and b show the microwave power dependence of two amplitude dips near gate voltages of −15 V and 0.5 V. The received signal amplitudes are normalized to the square root of the corresponding input powers. Additionally, mean values for each spectrum are subtracted to bring the curves to the same level. The color-coded power values are given on the right for each figure*. The dips are shifted horizontally from each other for clarity. Fig. VI.7a and b show the power dependences of the width of the amplitude dips in Fig. VI.6a and b obtained by fitting them to Lorenzian functions. As the power increases the width of the dip in Fig. VI.6a increases. On the other hand, the width of the much wider dip in Fig. VI.6b stays the same within the error of the measurement.

To understand this behaviour we investigate the current bias on the nanotube when a microwave power is applied through the resonator. The AC current through the nanotube is simulated by adding an ammeter in series with the nanotube in the circuit in Fig. VI.5. Fig. VI.6c shows the AC current for different input powers at the microwave port. As the power increases the AC current amplitude increases from 0.12 nA to 1.2 nA. This causes broadening of the transport features, and in particular the possible Coulomb resonances probed with the AC bias. The latter can lead to the broadening of the amplitude dip in Fig. VI.6a at higher powers. On the other hand, this mechanism of dip broadening does not affect the much wider dip in Fig. VI.6b.

In addition to the modulation of the AC current bias on the nanotube, other factors can also result in broadening of the amplitude dips. The influence of the microwave radiation on the DC transport through quantum dots has been studied in different systems [17, 174, 175, 176, 177]. In particular, the power dependence of

*Note that this is the power at the output of the wave generator which is further attenuated before reaching the sample.

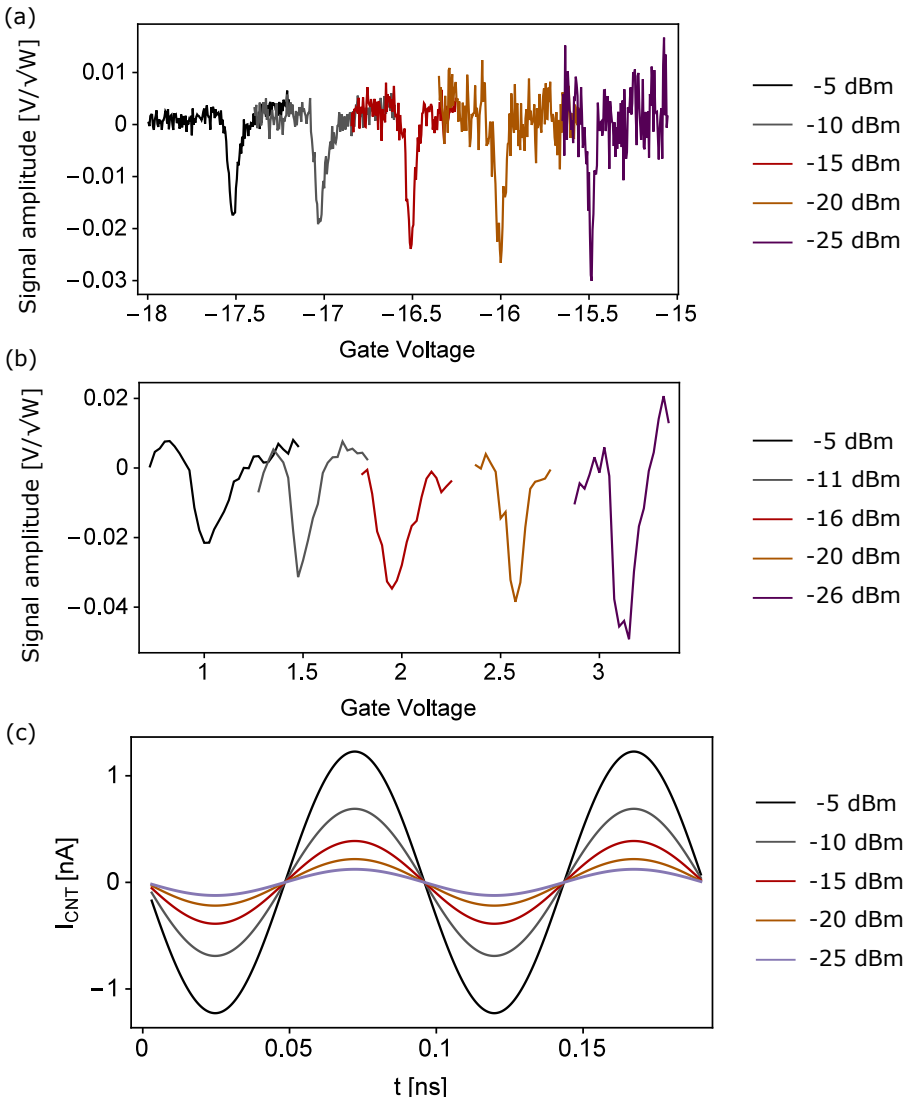


Figure VI.6: a,b. The normalized signal amplitude dips correspondingly around $V_G = -15\,\mathrm{V}$ and $V_G = 0.5\,\mathrm{V}$ as functions of the microwave power. The mean value for each spectrum is subtracted to bring the spectra to the same level. The power values are given on the right. As the power decreases the dips become sharper and their amplitudes increase. c. The AC current through the carbon nanotube at the resonance of the circuit for different input powers obtained from the simulations.

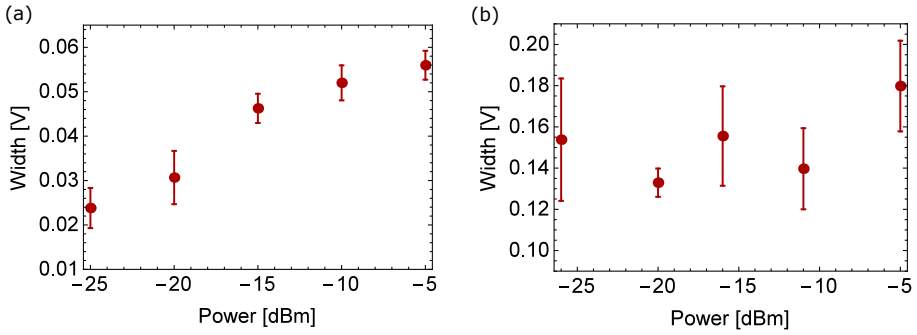


Figure VI.7: a. Power dependence of the amplitude dip width in Fig. VI.6a, showing the sharpening of the dip with decreasing power. b. Power dependence of the amplitude dip width in Fig. VI.6b. The dip width does not show a consistent dependence on the power.

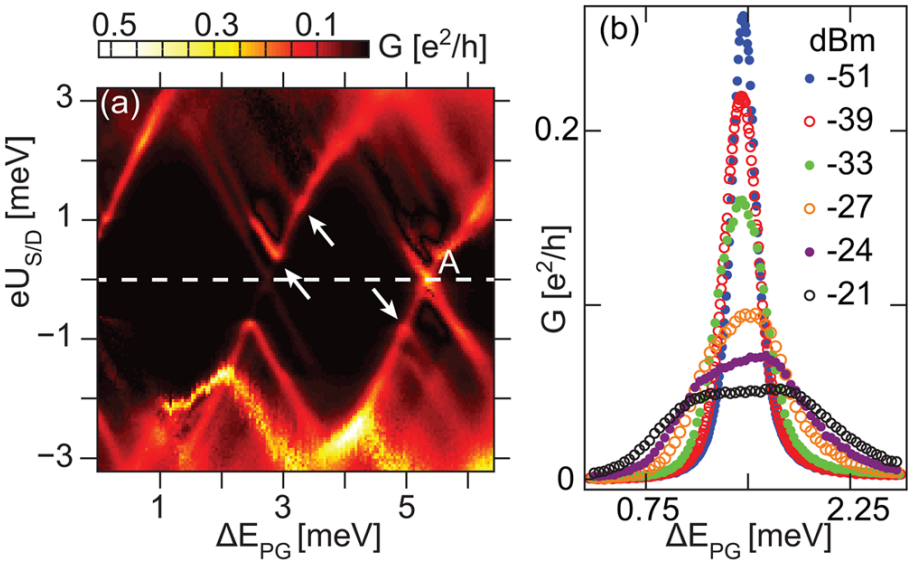


Figure VI.8: DC measurement of a GaAs quantum dot positioned at an antinode of the electric field of a microwave transmission-line resonator (taken from [17]). The DC characterization on the left shows a typical Coulomb blockade transport. On the right hand side a Coulomb resonance peak is plotted as a function of the power of the microwave signal in the resonator. As the power increases, the resonance broadens and its amplitude decreases due to the heating of the 2DEG in the quantum dot by the microwave field.

the Coulomb blockade resonances in a similar system has been observed by Frey *et. al.* in [17]. The authors investigate a GaAs quantum dot coupled to a microwave transmission-line resonator. The independently measured DC conductance through the dot shows Coulomb diamonds. In the first set of experiments studying the interaction between the two subsystems, the Coulomb conductance resonance is monitored under the application of a microwave field through the resonator. As the microwave power is increased, a reduction in the conductance of the quantum dot and a broadening of the Coulomb resonance are observed (Fig. VI.8). Similar effect has been observed in a GaAs quantum dot in [174]. According to the authors in [17], the modulation of the conductance resonance is due to the thermal broadening of the dot levels. The microwave field couples to the two-dimensional electron gas (2DEG) surrounding the quantum dot. The 2DEG is heated by the applied microwave field which results in the thermal broadening of the Coulomb peaks.

In case of a nanotube quantum dot the microwave radiation can similarly increase the electron temperature in the source and drain leads and the nanotube, resulting in the decrease of the amplitude and thermal broadening of the Coulomb resonances. However, as the contacts to the nanotube are superconducting, such broadening will be much smaller compared to the 2DEG quantum dot, which is resistive and can heat up more easily. Therefore, this explanation of the amplitude dip broadening in Fig. VI.6a and b is less likely.

3 Discussion and Conclusion

In this chapter we realized the first hybrid device in which an SN-bilayer was used to simultaneously contact a carbon nanotube and form a high quality microwave LC resonator, coupled to the nanotube. The advantage of the Pd (4 nm)/Al (80)nm bilayer used in this chapter is that it yields ohmic superconducting contacts to the

nanotubes. Additionally, LC resonators made from this bilayer show quality factors higher than 10^3. This is therefore a promising candidate for microwave probing of the superconductivity-driven transport in the nanotubes, and in particular the Andreev bound states.

A typical sample carries up to four coupled devices which are isolated from each other with a ground plane. To understand the microwave field behaviour in the sample and design the LC resonators with the desired frequencies AnSYS HFSS simulations are performed. Each resonator has been simulated individually and its transmission spectrum is obtained showing the resonance peak. The experimentally measured resonance frequencies are close to the values obtained from the simulations, the difference being only the addition of the kinetic inductance in the total inductance. The resonance spectra are measured as functions of the flux applied by the magnetic coil underneath the sample. At large enough field values the resonances shift and disappear due to the suppression of the superconductivity of the bilayer. This value agrees with the critical field value of the Al film. At low flux values no modulation of the frequency due to ABS are observed.

The gate voltage dependence of the resonance amplitude is measured showing sharp dips. The appearance of these dips shows a hysteresis when sweeping the gate voltage in two directions. The results are compared to the gate dependence of the signal amplitude far from the resonance, which shows no dependence on the gate voltage. Therefore, the gate dependence of the resonance amplitude is due to the gate dependence of the electrical transport through the nanotube. Using NI AWR simulations of the equivalent circuit, it is shown that the changes in the amplitude are due to the changes in the nanotube resistance when sweeping the gate voltage. The observed sharp dips can therefore be attributed to the Coulomb blockade effect in the nanotube, where conductance peaks are observed when tuning the gate voltage.

The power dependence of the amplitude dips is studied and illustrated for two dips at different gate voltages. As the power increases the narrower dip broadens. On the other hand, the increasing power does not affect the much wider dip. To understand this behaviour, the ac current through the nanotube for different input powers is obtained in the simulations. For the same power range, the ac current amplitude changes around 10 times. The increase in the ac current bias results in broadening of the transport features such as the Coulomb resonances. The latter causes the broadening of the narrow amplitude dip for higher microwave powers.

A less likely explanation of the observed broadening is the increase of the electron temperature in the source and drain leads as the microwave power is increased. This is compared to the broadening of a Coulomb resonance with the increasing power in a system consisting of a GaAs quantum dot coupled to a transmission-line resonator studied in [17]. However, in this system the 2DEG surrounding the quantum dot is resistive and is easily heated up with the microwave power, unlike the nanotube quantum dot, where the contacts are superconducting.

VII

Conclusion and Prospects

In this thesis, superconducting devices were studied with the aim of integrating superconducting contacted carbon nanotubes into superconducting microwave circuits. The aim of the first experiments was to study the quantum transport through nanotubes contacted to normal or superconducting leads. We have successfully developed fabrication methods for achieving high contact transparencies for both normal metal and superconducting metal contacted devices by using Pd as the layer in a direct contact with the nanotube. In addition to this, we have developed a reliable low-noise measurement setup allowing to observe the superfine structures in transport characteristics. The measurements of Coulomb blockade, Kondo effect and Fabry-Pérot transport characteristics have been illustrated depending on the nanotube-lead contact interface transparency. We also investigated in detail the transport characteristics of superconducting metal-contacted nanotubes where multiple Andreev reflections and supercurrent transport were clearly observed due to the high contact transparency provided by the Pd/Al layer. Furthermore, we showed the interplay of the supercurrent and MAR with different transport regimes, including the observed supercurrent transistor behaviour in the Fabry-Pérot

regime, as well as the interplay with the four-fold degenerate Coulomb blockade effect. We have observed an interesting behaviour of the MAR structures at the transition between Fabry-Pérot and Coulomb blockade regimes, which requires a more detailed investigation.

The second set of experiments pursued in the present work was aimed to investigate lumped-element LC resonators for coupling to carbon nanotube devices in a cQED geometry. Firstly, we have showed that high quality factors can be achieved for resonance frequencies higher than 12 GHz.

We were able to use measurements of these LC resonators to understand the superconducting proximity effect in Pd/Al SN bilayers. We have developed a convenient method for extracting the critical temperature and the magnetic penetration depth of the bilayers using only measurements of the microwave resonant frequencies and quality factors. . The extracted critical temperature of the bilayers showed a good agreement with the existing theoretical model. For low Pd thicknesses, the penetration depth showed a consistent increase with the thickness. However, for higher Pd thicknesses the values of the penetration depth were inconsistent. This is due to inaccurate measurements of the transmission spectra at high temperatures as well as generally lower qualities of the resonators with higher Pd thicknesses.

The consistent values of the critical temperature and the penetration depth showed nearly linear dependence on the Pd thickness. The natural extension of these experiments would be to study the bilayers with much larger normal layer thickness and observe the nonlinear behaviour of these parameters. This would allow for example to extract additional information about the bilayer, such as the transparency of the interface. Another improvement of the method would be to use coplanar waveguide resonators instead of lumped element LC resonators, which may show higher quality factors. This therefore would result in more precise values

of the extracted parameters at higher thicknesses of the normal layer, which is a limitation when using lumped-element resonators.

Finally, we have achieved embedding of a carbon nanotube in a SN microwave LC circuit. We have successfully fabricated the coupled nanotube-LC resonator devices from the Pd/Al bilayer, which has already been showed to be a good choice for both subsystems. The microwave simulations of the samples were illustrated proving to be very useful when designing the samples. We have illustrated the microwave probing of a Coulomb blockade in a nanotube quantum dot and compared it to the simulations of the equivalent circuit, which takes into account all the elements in the system. The power dependence of the obtained gate-dependent spectra showed an expected behaviour demonstrated in other resonator-quantum dot systems.

The first successful demonstration of the nanotube-resonator coupling creates the prospect of probing different quantum phenomena with the microwave field. In addition to this, the possibility and the advantages of studying a nanotube based flux qubit formed by a pair of Andreev bound states has been discussed. Therefore a major direction along these measurements would be to achieve a strong coupling and coherent manipulation of the Andreev bound states in such a circuit QED geometry. Possible improvements of the current system towards such experiments would be to optimize the geometry of the resonator by increasing the capacitance and decreasing the inductance. In this case, stronger coupling could be achieved for smaller sizes of the nanotube SQUID, thus minimizing the effects of flux noise. For large contact transparencies the ABS transition frequency lays in the region reachable by the resonators, and therefore anticrossing can be observed. In this case, the normal Pd layer turns out to be useful as it reduces the superconducting gap therefore further decreasing the ABS transition frequency. To further improve

the coupled system, one could consider grounding the resonators to eliminate the potential drift observed in our measurements.

The proposed architecture is thus promising for a broad range of future experiments on the rich physics in carbon nanotubes, as well as the possibility to implement a nanotube-based Andreev qubit controlled by a microwave field.

Bibliography

[1] Blais, A., Huang, R.-S., Walraff, A., Girvin, S. M. & Schoelkopf, R. J. Cavity quantum electrodynamics for superconducting electrical circuits: An architecture for quantum computation. *Phys. Rev. A* **69**, 062320 (2004).

[2] Walraff, A. *et al.* Strong coupling of a single photon to a superconducting qubit using circuit quantum electrodynamics. *Nature* **431**, 162–167 (2004).

[3] Schoelkopf, R. & Girvin, S. Wiring up quantum systems. *Nature* **451**, 664–669 (2008).

[4] Clarke, J. & Wilhelm, F. K. Superconducting quantum bits. *Nature* **453**, 1031 (2008).

[5] Toida, H., Nakajima, T. & Komiyama, S. Vacuum rabi splitting in a semiconductor circuit qed system. *Phys. Rev. Lett.* **110**, 066802 (2013).

[6] Deng, C., Otto, M. & Lupascu, A. An analysis method for transmission measurements of superconducting resonators with applications to quantum-regime dielectric-loss measurements. *J. Appl. Phys.* **114**, 054504 (2013).

[7] Rabl, P. *et al.* Hybrid quantum processors: Molecular ensembles as quantum memory for solid state circuits. *Phys. Rev. Lett.* **97**, 033003 (2006). URL `http://link.aps.org/doi/10.1103/PhysRevLett.97.033003`.

[8] Kubo, Y. *et al.* Strong coupling of a spin ensemble to a superconducting resonator. *Phys. Rev. Lett.* **105**, 140502 (2010).

[9] Schuster, D. I. *et al.* High-cooperativity coupling of electron-spin ensembles to superconducting cavities. *Phys. Rev. Lett.* **105**, 140501 (2010).

[10] Biercuk, M. J., Ilani, S., Marcus, C. M. & McEuen, P. L. Electrical transport in single-wall carbon nanotubes. *Top. Appl. Phys.* **111**, 455–493 (2008).

[11] Liang, W. *et al.* Fabry-Perot interference in a nanotube electron waveguide. *Nature* **411**, 665–669 (2001).

[12] Bockrath, M. *et al.* Luttinger-liquid behaviour in carbon nanotubes. *Nature* **397**, 598–601 (1999).

[13] Nygard, J., Cobden, D. H. & Lindelof, P. E. Kondo physics in carbon nanotubes. *Nature* **408**, 342–346 (2000).

[14] Steele, G. *et al.* Large spin-orbit coupling in carbon nanotubes. *Nature Communications* **4**, 1573 (2013).

[15] Galpin, M. R., Jayatilaka, F. W., Logan, D. E. & Anders, F. B. Interplay between Kondo physics and spin-orbit coupling in carbon nanotube quantum dots. *Phys. Rev. B* **81**, 075437 (2010).

[16] Andreev, A. F. Thermal conductivity of the intermediate state of superconductors. *J. Exptl. Theoret. Phys.* **47**, 2222 (1964).

[17] Frey, T. *et al.* Characterization of a microwave frequency resonator via a nearby quantum dot. *Appl. Phys. Lett.* **98**, 262105 (2011).

[18] Petersson, K. D. *et al.* Circuit quantum electrodynamics with a spin qubit. *Nature* **490**, 380 (2012).

[19] Basset, J. *et al.* Single-electron double quantum dot dipole-coupled to a single photonic mode. *Phys. Rev. B* **88**, 125312 (2013).

[20] Singh, V. *et al.* Optomechanical coupling between a multilayer graphene mechanical resonator and a superconducting microwave cavity. *Nature Nanotech.* **9**, 820–824 (2014).

[21] Teufel, J. D. *et al.* Sideband cooling of micromechanical motion to the quantum ground state. *Nature* **475**, 359–363 (2011).

[22] Delbecq, M. R. *et al.* Coupling a quantum dot, fermionic leads, and a microwave cavity on a chip. *Phys. Rev. Lett.* **107**, 256804 (2011).

[23] Delbecq, M. R. *et al.* Photon-mediated interaction between distant quantum dot circuits. *Nature Comm.* **4** (2012).

[24] Viennot, J. J., Delbecq, M. R., Dartiailh, M. C., Cottet, A. & Kontos, T. Out-of-equilibrium charge dynamics in a hybrid circuit quantum electrodynamics architecture. *Phys. Rev. B* **89**, 165404 (2014).

[25] Viennot, J. J., Dartiailh, M. C., Cottet, A. & Kontos, T. Coherent coupling of a single spin to microwave cavity photons. *Science* **349**, 408 (2015).

[26] Laird, E. A., Pei, F. & Kouwenhoven, L. P. A valley–spin qubit in a carbon nanotube. *Nature Nanotech.* **8**, 565 (2013).

[27] Zazunov, A., Shumeiko, V. S., Bratus, E. N., Lantz, J. & Wendin, G. Andreev level qubit. *Phys. Rev. Lett.* **90**, 087003 (2003).

[28] Bretheau, L., Girit, C. O., Pothier, H., Esteve, D. & Urbina, C. Exciting Andreev pairs in a superconducting atomic contact. *Nature* **499**, 312–315 (2013).

[29] Janvier, C. *et al.* Coherent manipulation of Andreev states in superconducting atomic contacts. *Science* **349**, 1199–1202 (2015).

[30] Beenakker, C. W. J. & van Houten, H. Josephson current through a superconducting quantum point contact shorter than the coherence length. *Phys. Rev. Lett.* **66**, 3056 (1991).

[31] Buitelaar, M. R., Nussbaumer, T. & Schönenberger, C. Quantum dot in the Kondo regime coupled to superconductors. *Phys. Rev. Lett.* **89**, 256801 (2002).

[32] Buitelaar, M. R. *et al.* Multiple andreev reflections in a carbon nanotube quantum dot. *Phys. Rev. Lett.* **91**, 057005 (2003).

[33] Jarillo-Herrero, P., van Dam, J. A. & Kouwenhoven, L. P. Quantum supercurrent transistors in carbon nanotubes. *Nature* **439**, 935–956 (2005).

[34] Eichler, A. *et al.* Even-odd effect in Andreev transport through a carbon nanotube quantum dot. *Phys. Rev. Lett.* **99**, 126602 (2007).

[35] Pillet, J.-D. *et al.* Andreev bound states in supercurrent-carrying carbon nanotubes revealed. *Nature Physics* **6**, 965 (2010).

[36] Chai, Y., Hazeghi, A., Takei, K. & Chen, H.-Y. Low resistance electrical contact to carbon nanotubes with graphitic interfacial layer. *IEEE Transactions On Electron Devices* **59**, 12–19 (2012).

[37] Lim, S. C. *et al.* Contact resistance between metal and carbon nanotube interconnects: Effect of work function and wettability. *Appl. Phys. Lett.* **95**, 264103 (2009).

[38] Kim, B. K. *et al.* Transport measurement of Andreev bound states in a Kondo-correlated quantum dot. *Phys. Rev. Lett.* **110**, 076803 (2013).

[39] Deutscher, G., Gennes, P. G. D. & Parks, R. D. *Superconductivity*, vol. 2 (Marcel Dekker, New York, 1969).

[40] Klapwijk, T. M. Proximity effect from an Andreev perspective. *J. Supercon.* **17**, 593 (2004).

[41] Josephson, B. D. Coupled superconductors. *Rev. Mod. Phys.* **36**, 216 (1964).

[42] Golubov, A. A., Kupriyanov, M. Y. & Il'ichev, E. The current-phase relation in josephson junctions. *Rev. Mod. Phys.* **76**, 411 (2004).

[43] Beenakker, C. W. J. & van Houten, H. Quantum transport in semiconductor nanostructures. *Solid State Physics* **44**, 1–228 (1991).

[44] Furusaki, A. & Tsukada, M. DC josephson effect and Andreev reflection. *Solid State Commun.* **78**, 299–302 (1991).

[45] Schindele, J., Baumgartner, A., Maurand, R., Weiss, M. & Schönenberger, C. Nonlocal spectroscopy of andreev bound states. *Phys. Rev. B* **89**, 045422 (2014).

[46] Kumar, A. *et al.* Temperature dependence of andreev spectra in a superconducting carbon nanotube quantum dot. *Phys. Rev. B* **89**, 075428 (2014). URL `http://link.aps.org/doi/10.1103/PhysRevB.89.075428`.

[47] Laird, E. A. *et al.* Quantum transport in carbon nanotubes. *Rev. Mod. Phys.* **87**, 703 (2015).

[48] Tans, S. T., Devoret, M. H., Groenevels, R. J. A. & Dekker, C. Electron–electron correlations in carbon nanotubes. *Nature* **394**, 761 (1998).

[49] Bockrath, M. *et al.* Single-electron transport in ropes of carbon nanotubes. *Science* **275**, 1922–1925 (1997).

[50] Grove-Rasmussen, K., JØorgensen, H. I. & Lindelof, P. E. Kondo resonance enhanced supercurrent in single wall carbon nanotube Josephson junctions. *New Journal of Physics* **9**, 124 (2007).

[51] Goldhaber-Gordon, D. *et al.* Kondo effect in a single-electron transistor. *Nature* **391**, 156 (1998).

[52] Paaske, J. *et al.* Non-equilibrium singlet–triplet kondo effect in carbon nanotubes. *Nature Physics* **2**, 460 (2006).

[53] Wei, Y., Wang, J., Guo, H., Mehrez, H. & Roland, R. Resonant Andreev reflections in superconductor-carbon nanotube devices. *Phys. Rev. B* **63**, 195412 (2001).

[54] Iijima, S. Helical microtubules of graphitic carbon. *Nature* **354**, 56 (1991).

[55] Terrones, M. Science and technology of the twenty-first century: Synthesis, properties, and applications of carbon nanotubes. *Annu. Rev. Mater Res.* **33**, 419 (2003).

[56] Dai, H. Carbon nanotubes: Synthesis, integration, and properties. *Acc. Chem. Res.* **35**, 1035 (2002).

[57] Bandaru, P. R. Electrical properties and applications of carbon nanotube structures. *Journal of Nanoscience and Nanotechnology* **7**, 1239 (2007).

[58] Harris, P. J. F. *Carbon Nanotube Science: Synthesis, Properties and Applications* (Cambridge University Press, University of Reading, UK, 2011).

[59] Gopalakrishnan, S. & Narender, S. *Wave propagation in nanostructures: Non-local continuum mechanics formulations* (Springer International Publishing, 2013).

[60] Castro Neto, A. H., Guinea, F., Peros, N. M. R., Novoselev, K. S. & Geim, A. K. The electronic properties of graphene. *Rev. Mod. Phys.* **81**, 109 (2009).

[61] Saito, R., Dresselhaus, G. & Dresselhaus, M. S. *Physical properties of carbon nanotubes* (Imperial College Press, 1998).

[62] Rafii-Tabar, H. *Computational physics of carbon nanotubes* (Cambridge University Press, New York, 2008), 1st edn.

[63] Hamada, N., Sawada, S. & Oshiyama, A. New one-dimensional conductors: Graphitic microtubules. *Phys. Rev. Lett.* **68**, 1579 (1992).

[64] Saito, R., Fujita, M. & Dresselhaus, G. Electronic structure of chiral graphene tubules. *Appl. Phys. Lett.* **60**, 2204 (1992).

[65] Heyd, R., Charlier, A. & McRae, E. Uniaxial-stress effects on the electronic properties of carbon nanotubes. *Phys. Rev. B* **55**, 6820 (1997).

[66] Rochefort, A., Salahub, D. R. & Avouris, P. The effect of structural distortions on the electronic structure of carbon nanotubes. *Chem. Phys. Lett.* **297**, 45–50 (1998).

[67] Yang, L. & Han, J. Electronic structure of deformed carbon nanotubes. *Phys. Rev. Lett.* **85**, 154 (2000).

[68] Kane, C. L. & Mele, E. J. Size, shape and low energy electronic structure of carbon nanotubes. *Phys. Rev. Lett.* **78**, 1932 (1997).

[69] Ouyang, M., Huang, J. L., Cheung, C. L. & Lieber, C. M. Energy gaps in "metallic" single-walled carbon nanotubes". *Science* **292**, 702–705 (2001).

[70] Ihn, T. *Semiconductor nanostructures* (Oxford University Press, 2011).

[71] Cobas, E. & Fuhrer, M. S. Microwave rectification by a carbon nanotube Schottky diode. *Appl. Phys. Lett* **93**, 043120 (2008).

[72] Chen, Z., Appenzeller, J., Knoch, J., Lin, Y. & Avouris, P. The role of metal-nanotube contact in the performance of carbon nanotube field-effect transistors. *Nano Letters* **5**, 1497–1502 (2005).

[73] Liu, W., Hierold, C. & Haluska, M. Electrical contacts to individual SWCNTs: A review. *Beilstein J. Nanotechnol.* **5**, 2202–2215 (2014).

[74] Javey, A., Guo, J., Wang, Q., Lundstrom, M. & Dai, H. Ballistic carbon nanotube field-effect transistors. *Nature* **424**, 654–657 (2003).

[75] Yahya, N. *Carbon and oxide nanostructures: Synthesis, characterization and applications* (Springer, Heidelberg, 2010).

[76] Sapmaz, S., Jarillo-Herrero, P., Kouwenhoven, L. K. & van der Zant, H. S. J. Quantum dots in carbon nanotubes. *Semicond. Sci. Technol.* **21**, S52–S63 (2006).

[77] Reich, S., Thomsen, C. & Maultzsch, J. *Carbon nanotubes: basic concepts and physical properties* (Wiley, 2004).

[78] Beenakker, C. W. J. Theory of Coulomb-blockade oscillations in the conductance of a quantum dot. *Phys. Rev. B* **44**, 1646 (1991).

[79] Oreg, Y., Byczuk, K. & Halperin, B. I. Spin configuration of a carbon nanotube in a nonuniform external potential. *Phys. Rev. Lett.* **85**, 365 (2000).

[80] Sapmaz, S. *et al.* Electronic excitation spectrum of metallic carbon nanotubes. *Phys. Rev. B* **71**, 153402 (2005).

[81] Liang, W., Bockrath, M. & Park, H. Shell filling and exchange coupling in metallic single-walled carbon nanotubes. *Phys. Rev. Lett.* **88**, 126801 (2002).

[82] van den Berg, G. & de Nobel, J. Les propriétés à basses températures des alliages des métaux normaux avec des solutés de transition. *Journal de Physique et le Radium* **23**, 665 (1962).

[83] Rowell, J. & Shen, L. Y. L. Zero-bias anomalies in normal metal tunnel junctions. *Phys. Rev. Lett.* **17**, 15 (1966).

[84] Kondo, J. Resistance minimum in dilute magnetic alloys. *Progress of Theoretical Physics* **32**, 37 (1964).

[85] Appelbaum, J. Exchange model of zero-bias tunneling anomalies. *Physical Review* **154**, 633 (1967).

[86] Anderson, P. Localized magnetic states and Fermi-surface anomalies in tunneling. *Phys. Rev. Lett.* **17**, 95 (1966).

[87] Wilson, K. The renormalization group: Critical phenomena and Kondo problem. *Reviews of Modern Physics* **47**, 773 (1975).

[88] Cronenwett, S. M., Oosterkamp, T. H. & Kouwenhoven, L. P. A tunable Kondo effect in quantum dots. *Science* **281**, 540 (1998).

[89] Goldhaber-Gordon, D. *et al.* From the Kondo regime to the mixed-valence regime in a single-electron transistor. *Phys. Rev. Lett.* **81**, 5225 (1998).

[90] Haldane, F. D. Scaling theory of the asymmetric Anderson model. *Phys. Rev. Lett.* **40**, 416 (1978).

[91] Kim, N. Y. *Correlated Electron Transport in one-dimensional microscopic conductors*. Ph.D. thesis, Stanford University (2006).

[92] Javey, A. *et al.* High-field quasiballistic transport in short carbon nanotubes. *Phys. Rev. Lett.* **92**, 106804 (2004).

[93] Berger, C., Yi, Y., Wang, Z. L. & de Heer, W. Multiwalled carbon nanotubes are ballistic conductors at room temperature. *Appl. Phys. A* **74**, 363 (2002).

[94] Berger, C., Poncharal, P., Yi, Y. & de Heer, W. Ballistic conduction in multi-walled carbon nanotubes. *J. Nanosci. Nanotechnol.* **3**, 171 (2003).

[95] Büttiker, M. Scattering theory of current and intensity noise correlations in conductors and wave guides. *Phys. Rev. B* **46**, 12485 (1992).

[96] Imry, Y. & Landauer, R. Conductance viewed as transmission. *Rev. Mod. Phys.* **71**, S306 (1999).

[97] Saint-James, D. Elementary excitations in the vicinity of the surface separating a normal metal and a superconducting metal. *Journal de Physique* **25**, 899 (1964).

[98] de Gennes, P. G. & Saint-James, D. Elementary excitations in the vicinity of a normal metal-superconducting metal contact. *Physics Letters* **4**, 151–152 (1963).

[99] de Gennes, P. G. Boundary effects in superconductors. *Reviews of Modern Physics* **36**, 225 (1964).

[100] Ojeda-Aristizabel, C., Ferrier, M., Guéron, S. & Bouchiat, H. Tuning the proximity effect in a superconductor-graphene-superconductor junction. *Phys. Rev. B* **79**, 165436 (2009).

[101] Kasumov, A. Y. *et al.* Proximity effect in a superconductor-metallofullerene-superconductor molecular junction. *Phys. Rev. B* **72**, 033414 (2005).

[102] Cuevas, J. C., Hammer, J., Viljas, J. K. J. K. & Eschrig, M. Proximity effect and multiple Andreev reflections in diffusive superconductor–normal-metal–superconductor junctions. *Phys. Rev. B* **73**, 184505 (2006).

[103] Kontos, T., Aprili, M., Lesueur, J. & Grison, X. Inhomogeneous superconductivity induced in a ferromagnet by proximity effect. *Phys. Rev. Lett.* **86**, 304 (2001).

[104] Buzdin, A. I. Proximity effects in superconductor-ferromagnet heterostructures. *Rev. Mod. Phys.* **77**, 935 (2005).

[105] Doh, Y.-J. *et al.* Tunable supercurrent through semiconductor nanowires. *Science* **309**, 272–275 (2005).

[106] Volkov, A. F., Magnée, P. H. C., Wees, B. J. V. & Klapwijk, T. M. Proximity and josephson effects in superconductor-two-dimensional electron gas planar junctions. *Physica C: Superconductivity* **242**, 261–266 (1995).

[107] Scheer, E. *et al.* Proximity effect and multiple Andreev reflections in gold atomic contacts. *Phys. Rev. Lett.* **86**, 284 (2001).

[108] de Gennes, P. G. *Superconductivity of Metals and Alloys* (Addison-Wesley, New York, 1989).

[109] Bardeen, J., Cooper, L. N. & Schrieffer, J. R. Theory of superconductivity. *Phys. Rev.* **108**, 1175–1204 (1957).

[110] Schäpers, T. Superconductor/semiconductor junctions. *Springer Tracts in Modern Physics* **174** (2001).

[111] Taylor, B. N. & Burstein, E. Excess currents in electron tunneling between superconductors. *Phys. Rev. Lett.* **10**, 14 (1963).

[112] Klapwijk, T. M., Blonder, G. E. & Tinkham, M. Explanation of subharmonic energy gap structure in superconducting contacts. *Physica B+C* **109-110**, 1657–1664 (1982).

[113] Octavio, M., Tinkham, M., Blonder, G. E. & Klapwijk, T. M. Subharmonic energy-gap structure in superconducting constrictions. *Phys. Rev. B* **27**, 6739 (1983).

[114] Bratus, E. N., Shumeiko, V. S. & Wendin, G. Theory of subharmonic gap structure in superconducting mesoscopic tunnel contacts. *Phys. Rev. Lett.* **74**, 2110 (1995).

[115] Chauvin, M. *The Josephson effect in superconducting atomic contacts.* Ph.D. thesis, Université Paris 6 (2005).

[116] Jøorgensen, H. I. *et al.* Electrical transport in single-wall carbon nanotube weak links in the fabry-perot regime. *Phys. Rev. Lett.* **96**, 207003 (2006).

[117] Grove-Rasmussen, K. *et al.* Superconductivity-enhanced bias spectroscopy in carbon nanotube quantum dots. *Phys. Rev. B* **79**, 134518 (2009).

[118] Delagrange, R. *et al.* 0-π quantum transition in a carbon nanotube josephson junction: Universal phase dependence and orbital degeneracy. *Phys. Rev. B* **93**, 195437 (2016).

[119] Cleuziou, J.-P., Wernsdorfer, W., Bouchiat, V., Ondarçuhu, T. & Monthioux, M. Carbon nanotube superconducting quantum interference device. *Nature Nanotechnology* **1**, 53–59 (2006).

[120] Gramich, J., Baumgartner, A. & Schönenberger, C. Resonant and inelastic andreev tunneling observed on a carbon nanotube quantum dot. *Phys. Rev. Lett.* **115**, 216801 (2015).

[121] Day, P. K., LeDuc, H. G., Mazin, B. A., Vayonakis, A. & Zmuidzinas, J. A broadband superconducting detector suitable for use in large arrays. *Nature* **425**, 817–821 (2003).

[122] Pozar, D. M. *Microwave Engineering* (John Wiley & Sons, Inc., New York, 2012), 4th edn.

[123] Göppl, M. *et al.* Coplanar waveguide resonators for circuit quantum electrodynamics. *Journal of Applied Physics* **104**, 113904 (2008).

[124] Lindström, T. *et al.* Circuit QED with a flux qubit strongly coupled to a coplanar transmission line resonator. *Semicon. Sci. Tech.* **20**, 814 (2007).

[125] Megrant, A. *et al.* Planar superconducting resonators with internal quality factors above one million. *Appl. Phys. Lett.* **100**, 113510 (2012).

[126] Mazin, B. A. *Microwave Kinetic Inductance Detectors*. Ph.D. thesis, California Institute of Technology (2004).

[127] Meservey, R. & Tedrow, P. M. Measurements of kinetic inductance of superconducting linear structures. *J. Appl. Phys.* **40**, 2028 (1969).

[128] Doyle, S. *Lumped element kinetic inductance detectors*. Ph.D. thesis, Cardiff University (2008).

[129] Wadell, B. C. *Transmission line design handbook* (Artech House, Inc, 1991).

[130] Tinkham, M. *Introduction to superconductivity* (Dover Publications, 2004).

[131] Rose-Innes, A. *Introduction to superconductivity* (Pergamon Press, 1978).

[132] Schuster, D. I. *Circuit Quantum Electrodynamics*. Ph.D. thesis, Yale University (2007).

[133] Bardeen, J. Two-fluid model of superconductivity. *Phys. Rev. Lett.* **1**, 399 (1958).

[134] Romero, G., Lizuain, I., Shumeiko, V. S., Solano, E. & Bergeret, F. S. Circuit quantum electrodynamics with a superconducting quantum point contact. *Phys. Rev. B* **85**, 180506(R) (2012).

[135] Masne, Q. L. *Asymmetric current fluctuations and Andreev states probed with a Josephson junction*. Ph.D. thesis, CEA Saclay (2009).

[136] Wallraff, A. *et al.* Strong coupling of a single photon to a superconducting qubit using circuit quantum electrodynamics. *Nature* **431**, 162–167 (2004).

[137] Siddiqi, I. *et al.* Dispersive measurements of superconducting qubit coherence with a fast latching readout. *Phys. Rev. B* **73**, 054510 (2006).

[138] Devoret, M. H., Girvin, S. & Schoelkopf, R. Circuit-QED: How strong can the coupling between a Josephson junction atom and a transmission line resonator be? *Annalen der Physik* **519**, 767–779 (2007).

[139] Abdumalikov, A. A., Astafiev, O., Nakamura, Y., Pashkin, Y. A. & Tsai, J. Vacuum rabi splitting due to strong coupling of a flux qubit and a coplanar-waveguide resonator. *Phys. Rev. B* **78**, 180502(R) (2008).

[140] Lupaşcu, A., Verwijs, C. J. M., Schouten, R. N., Harmans, C. J. P. M. & Mooij, J. E. Nondestructive readout for a superconducting flux qubit. *Phys. Rev. Lett.* **93**, 177006 (2004).

[141] Pei, F. *Quantum Transport in one-dimensional nanostructures.* Ph.D. thesis, Kavli Institute of Nanoscience, TU Delft (2015).

[142] Peigney, A. *et al.* A study of the formation of single- and double-walled carbon nanotubes by a CVD method. *J. Phys. Chem. B* **105**, 9699–9710 (2001).

[143] Jarillo-Herrero, P., Sapmaz, S., Dekker, C., Kouwenhoven, L. P. & van der Zant, H. S. J. A few electron-hole semiconducting carbon nanotube quantum dot. In *Electronic Properties of Synthetic Nanostructures: XVII International Winterschool/Euroconference on Electronic Properties of Novel Materials* (2004).

[144] Ratz, S. *et al.* Thermally induced subgap features in the cotunneling spectroscopy of a carbon nanotube. *New Journal of Physics* **16**, 123040 (2014).

[145] Douglass Jr, D. H. Magnetic field dependence of the superconducting energy gap. *Phys. Rev. Lett.* **6**, 346 (1961).

[146] Galaktinov, A. V. & Zaikin, A. D. Quantum interference and supercurrent in multiple-barrier proximity structures. *Phys. Rev. B* **65**, 184507 (2002).

[147] Jøorgensen, H. I. *et al.* Critical current 0-π transition in designed josephson quantum dot junctions. *Nano Lett.* **7(8)**, 2441–2445 (2007).

[148] Yeyati, A. L., Cuevas, J. C., López-Dávalos, A. & Martín-Rodero, A. Resonant tunneling through a small quantum dot coupled to superconducting leads. *Phys. Rev. B* **55**, R6137 (1997).

[149] Abdo, B., Segev, E., Shtepluck, O. & Buke, E. Nonlinear dynamics in the resonance lineshape of NbN superconducting resonators. *Phys. Rev. B* **73**, 134513 (2006).

[150] Martinis, J. M. *et al.* Decoherence in josephson qubits from dielectric loss. *Phys. Rev. Lett.* **95**, 210503 (2005).

[151] O'Connell, A. D. *et al.* Microwave dielectric loss at single photon energies and millikelvin temperatures. *Appl. Phys. Lett.* **92**, 112903 (2008).

[152] Ruggiero, B., Delsing, P., Granata, C., Pashkin, Y. & Silvestrini, P. *Quantum computation in solid state systems* (Springer, New York, 2006).

[153] Rammer, J. & Smith, H. Quantum field-theoretical methods in transport theory of metals. *Rev. Mod. Phys.* **58**, 323 (1986).

[154] Eilenberger, G. Transformation of Gorkov's equation for type ii superconductors into transport-like equations. *Z. Physik* **214**, 195 (1968).

[155] Usadel, K. D. Generalized diffusion equation for superconducting alloys. *Phys. Rev. Lett.* **25**, 507 (1970).

[156] Clarke, J. Supercurrents in lead-copper-lead sandwiches. *Proc. R. Soc. London A.: Math. Phys. Sci* **308**, 447 (1969).

[157] Adkins, C. J. & Kingston, B. W. Investigations of the proximity effect by electron tunneling. *Phys. Rev.* **177**, 777 (1969).

[158] Toplicar, J. R. & Finnemore, D. K. Electron tunneling study of the superconducting proximity effect in Pb-Cd. *Phys. Rev. B* **16**, 2072 (1977).

[159] Kastalsky, A., Greene, L. H., Barner, J. B. & Bhat, R. Proximity-effect superconductive tunneling in Nb on nGaAs/InP/InGaAs heterostructures. *Phys. Rev. Lett.* **64**, 958 (1990).

[160] Guéron, S., Pothier, H., Birge, N. O., Esteve, D. & Devoret, M. H. Superconducting proximity effect probed on a mesoscopic length scale. *Phys. Rev. Lett.* **77**, 3025 (1996).

[161] Martinis, J. M., Hilton, G. C., Irwin, K. D. & Wollman, D. A. Calculation of t_c in a normal-superconductor bilayer using the microscopic-based usadel theory. *Nuclear Instruments and Methods in Physics Research* **444**, 23–27 (2000).

[162] Simon, R. W. & Chaikin, P. M. Penetration depth in proximity-effect superconductors. *Phys. Rev. B* **30**, 3750 (1984).

[163] Pambianchi, M. S., Chen, L. & Anlage, S. M. Complex conductivity of proximity-superconducting Nb/Cu bilayers. *Phys. Rev. B* **54**, 3508 (1996).

[164] Wang, R. F., Zhao, S. P., Chen, G. H. & Yang, Q. S. Magnetic penetration depth in Nb/Al and Nb/Cu superconducting proximity bilayers. *Phys. Rev. B* **62**, 11793 (2000).

[165] Claassen, J. H., Evetts, J. E., Somekh, R. E. & Barber, Z. H. Observation of the superconducting proximity effect from kinetic-inductance measurements. *Phys. Rev. B* **44**, 9605–9608 (1991).

[166] Kanoda, K., Mazaki, H., Hosoito, N. & Shinjo, T. Magnetic-field penetration depth and material parameters of V-Ag multilayered superconductors. *Phys. Rev. B* **35**, 8413–8420 (1987).

[167] Steinberg, K., Scheffler, M. & Dressel, M. Quasiparticle response of superconducting aluminum to electromagnetic radiation. *Phys. Rev. B* **77**, 214517 (2008).

[168] Mercaldo, L. V., Anlage, S. M. & Maritato, L. Microwave surface impedance of proximity-coupled superconducting (Nb)/spin-glass (CuMn) bilayers. *Phys. Rev. B* **59**, 4455 (1999).

[169] Kim, J., Doh, Y.-J., Char, K., Doh, H. & Choi, H.-Y. Proximity effect in Nb/Au/CoFe trilayers. *Phys. Rev. B* **71**, 214519 (2005).

[170] Burke, P. J. An RF circuit model for carbon nanotubes. *IEEE Trans. Nanotechnol.* **2**, 55–58 (2003).

[171] Raychowdhury, A. & Roy, K. A circuit model for carbon nanotube interconnects: comparative study with cu interconnects for scaled technologies. *Proc. 2004 IEEE/ACM ICCAD* 237–240 (2004).

[172] Burke, P. J. Luttinger liquid theory as a model of the gigahertz electrical properties of carbon nanotubes. *IEEE Trans. Nanotechnol.* **1**, 129–144 (2002).

[173] Ramo, S., Whinnery, J. R. & Duzer, T. V. *Fields and Waves in Communication Electronics* (Wiley, 1994).

[174] Fujii, K. *et al.* Microwave modulation of Coulomb-blockade oscillations in a quantum dot. *Physica B: Condensed Matter* **227**, 98–101 (1999).

[175] Elzerman, J. M., Franceschi, S. D., Goldhaber-Gordon, D., van der Wiel, W. G. & Kouwenhoven, L. P. Suppression of the Kondo effect in a quantum dot by microwave radiation. *Journal of Low Temp. Phys.* **118** (1999).

[176] Ida, T., Ishibashi, K., Tsukagoshi, K. & Aoyagi, Y. Quantum-dot transport in carbon nanotubes. *Superlat. Microstruct.* **27**, 551 (2000).

[177] Kawakami, E. *et al.* Excitation of a Si/SiGe quantum dot using an on-chip microwave antenna. *Appl. Phys. Lett.* **103**, 132410 (2013).

Appendices

A

Derivation of the Transmission for Two-port Resonators

In this appendix we present a detailed derivation of the equation for the transmission for two-port LC resonators (Eqn. V.1). Fig. A.1a is the equivalent circuit of the two-port resonators, where R_l is the load resistance of a port, C_k is the coupling capacitance and C_g is the capacitance to the ground. The series connection of these two elements with total impedance Z_s can be transformed into an equivalent parallel connection with impedance Z_p with circuit elements R_l' and C_k'. By equating the two impedances we find,

$$R_l' = \frac{1 + C_k^2 R_l^2 \omega^2}{C_k^2 R_l \omega^2} \approx \frac{1}{C_k^2 R_l \omega^2}, \quad C_k^2 = \frac{C_k}{1 + C_k^2 R_l^2 \omega^2} \approx C_k. \tag{A.1}$$

The approximations are made taking into account that for coupling capacitances typically in the fF range and frequencies in GHz range, $1/C_k^2\omega^2 >> R_l$.

A similar transformation is done for the series connection of L and R in Fig. A.1a, which yields

$$R' = \frac{R^2 + L^2\omega^2}{R} \approx \frac{L^2\omega^2}{R}, \quad L' = \frac{R^2 + L^2\omega^2}{L\omega^2} \approx L. \tag{A.2}$$

The approximation $L^2\omega^2 >> R^2$ is applied here, which is valid for the typical inductances of the order of nH.

WIth these transformations the circuit in Fig. A.1a can be effectively represented by the parallel circuit in Fig. A.1b [123]. The latter is a two-port network with port impedances $4R'$ and admittance

$$Y = \frac{1}{i\omega L} + i\omega(C + C_g/2 + C_k/2) + \frac{1}{R'}. \tag{A.3}$$

Taking $Im(Y(\omega = \omega_0)) = 0$ on resonance, we obtain

$$\omega_0 = \frac{1}{\sqrt{LC_{total}}}, \quad C_{total} = C + \frac{C_g}{2} + \frac{C_k}{2}. \tag{A.4}$$

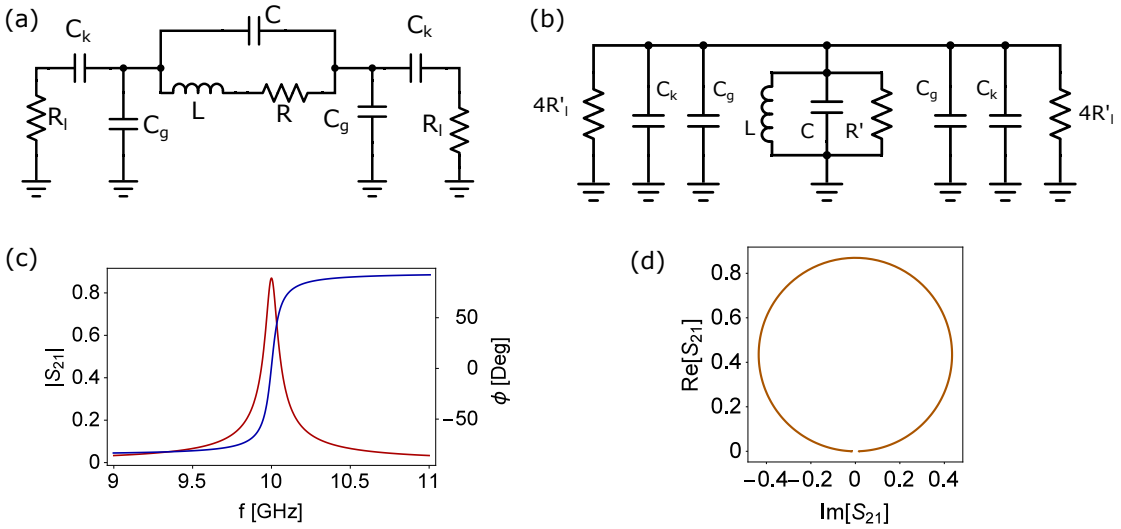


Figure A.1: a. The equivalent circuit of the two-port LC resonator. R_l is the load resistance of the ports, C_k is the coupling capacitance, C_g is the capacitance to the ground. b. The equivalent parallel circuit transformation of the circuit in a. c. The amplitude and phase of the transmission given by Eqn. A.9 obtained for $Q_i = 1000$, $Q_l = 150$ and $\omega_0 = 2\pi \cdot 10\,\mathrm{GHz}$. d. The plot of the transmission in the complex plane.

The admittance can therefore be rewritten as

$$Y = \frac{1}{i\omega L}(1 - \frac{\omega^2}{\omega_0^2}) + \frac{1}{R'} \approx \frac{2i}{\omega_0^2 L}(\omega - \omega_0) + \frac{1}{R'}. \tag{A.5}$$

On the other hand, the loaded quality factor for the circuit in Fig. A.1b is given by

$$Q_l = \omega_0 C_{total} \frac{1}{1/R' + 1/2R'_l}. \tag{A.6}$$

Substituting Eqn. A.6 in Eqn. A.5, we obtain

$$Y \approx 2iQ_l \frac{\Delta\omega}{\omega_0}\left(\frac{1}{R'} + \frac{1}{2R'_l}\right) + \frac{1}{R'}, \tag{A.7}$$

where $\Delta\omega = \omega - \omega_0$. Using the equation for the transmission of a two-port network with shunt admittance Y, we obtain [122]

$$S_{21} = \frac{2}{2 + Y/Y_0} = \frac{1}{(1 + \frac{2R'_l}{R'})(1 + 2iQ_l\frac{\Delta\omega}{\omega_0})}. \tag{A.8}$$

Finally taking into account that $Q_i = \omega_0 C_{total} R'$, the equation for the transmission can be written as

$$S_{21} = \frac{Q_i/Q_e}{(1 + \frac{Q_i}{Q_e})(1 + 2iQ_l\frac{\Delta\omega}{\omega_0})}. \tag{A.9}$$

The amplitude and phase of the transmission given by Eqn. A.9 are plotted in Fig. A.1c for typical values of the quality factors and the resonance frequency. The amplitude shows a resonance peak at the resonance frequency of 10 GHz. The plot of S_{21} in the complex plain is shown in Fig. A.1d.

B

Labeling of Nanotube Devices

Table B.1 shows the growth and geometrical parameters for each nanotube device measured in this thesis.

Nanotube device label	Growth	Substrate	metal layer	contact distance
DC-Pd-1	CVD	Si ($\rho > 20000\ \Omega$·cm)	Pd (50 nm)	300nm
DC-Pd-2	CVD	Si ($\rho > 20000\ \Omega$·cm)	Pd (50 nm)	300nm
DC-Pd-3	CVD	Si ($\rho > 20000\ \Omega$·cm)	Pd (50 nm)	1 μm
DC-SN-1	CVD	Si ($\rho > 20000\ \Omega$·cm)	Pd/Al (4/80 nm)	300 nm
DC-SN-2	CVD	Si ($\rho > 20000\ \Omega$·cm)	Pd/Al (4/80 nm)	300 nm
DC-SN-3	CVD	Si ($\rho > 20000\ \Omega$·cm)	Pd/Al (4/80 nm)	300 nm

Table B.1: Nanotube device labeling